

NAVAL POSTGRADUATE SCHOOL

MONTEREY, CALIFORNIA



19980611 060

THESIS

**PRESSURE-SENSITIVE PAINT
MEASUREMENT TECHNIQUE
DEVELOPMENT FOR TURBOMACHINERY
APPLICATION**

by

Kevin J. Quinn

December 1997

Thesis Advisor:

Raymond P. Shreeve

Approved for public release; distribution is unlimited.

REPORT DOCUMENTATION PAGE

Form Approved OMB No. 0704-0188

Public reporting burden for this collection of information is estimated to average 1 hour per response, including the time for reviewing instruction, searching existing data sources, gathering and maintaining the data needed, and completing and reviewing the collection of information. Send comments regarding this burden estimate or any other aspect of this collection of information, including suggestions for reducing this burden, to Washington Headquarters Service, Directorate for Information Operations And Reports, 1215 Jefferson Davis Highway, Suite 1204, Arlington, Va 22202-4302, and to the Office Of Management And Budget, Paperwork Reduction Project (0704-0188) Washington DC 20503.

1. AGENCY USE ONLY (Leave Blank)			2. REPORT DATE December 1997	3. REPORT TYPE AND DATES COVERED Engineer's Thesis	
4. TITLE AND SUBTITLE PRESSURE-SENSITIVE PAINT MEASUREMENT TECHNIQUE DEVELOPMENT FOR TURBOMACHINERY APPLICATION			5. FUNDING NUMBERS		
6. AUTHOR(S) Quinn, Kevin J.					
7. PERFORMING ORGANIZATION NAME(S) AND ADDRESS(ES) Naval Postgraduate School Monterey, CA 93943-5000			8. PERFORMING ORGANIZATION REPORT NUMBER		
9. SPONSORING/MONITORING AGENCY NAME(S) AND ADDRESS(ES)			10. SPONSORING/MONITORING AGENCY REPORT NUMBER		
11. SUPPLEMENTARY NOTES The views in this thesis are those of the author and do not reflect the official policy or position of the Department of Defense or the U.S. Government					
12a. DISTRIBUTION/AVAILABILITY STATEMENT Approved for public release; distribution is unlimited			12b. DISTRIBUTION CODE		
13. ABSTRACT (maximum 200 words) Pressure-sensitive paint measurement on a transonic compressor rotor required the prior development of phase-locked cumulative imaging using a disk-rotor driven by a high-speed Hamilton-Standard turbine as a developmental test-bed. The turbine was installed in a protective housing in the Gas Dynamics Laboratory and connected to an 8000 cu ft, 300 psi air supply. An hydraulic pump provided bearing lubrication. A once per revolution trigger signal was produced from a light-emitting diode and PIN photodiode pair. The imaging system consisted of an intensified CCD video camera externally triggered by the 1/rev signal via a waveform shaping circuit designed for the present application. Images were captured at camera gate speeds calculated to eliminate pixel blur and image integration times were varied to optimize image intensity and spatial resolution. Structural and modal analyses of the disk-rotor were conducted and a simplified numerical model of the flow was computed. Ratioed, colored images were produced for wheel speeds to 20,000 RPM. The effect of the radially varying stagnation temperature was evident, underscoring the importance of quantifying and accounting for the PSP temperature sensitivity so that quantitative pressure data may be obtained. Recommendations for a follow-on program are reported.					
14. SUBJECT TERMS Pressure-Sensitive Paint, Phase-Locked Imaging, Transonic Rotor Measurements, CFD Analysis				15. NUMBER OF PAGES 98	
16. PRICE CODE					
17. SECURITY CLASSIFICATION OF REPORT Unclassified	18. SECURITY CLASSIFICATION OF THIS PAGE Unclassified	19. SECURITY CLASSIFICATION OF ABSTRACT Unclassified	20. LIMITATION OF ABSTRACT UL		

NSN 7540-01-280-5500

Standard Form 298 (Rev. 2-89)
Prescribed by ANSI Std. Z39-18 298-102

Approved for public release; distribution is unlimited.

PRESSURE-SENSITIVE PAINT MEASUREMENT TECHNIQUE DEVELOPMENT FOR TURBOMACHINERY APPLICATION

Kevin J. Quinn
Lieutenant, United States Navy
B.S., United States Naval Academy, 1989

Submitted in partial fulfillment of the
requirements for the degree of

AERONAUTICAL AND ASTRONAUTICAL
ENGINEER

from the

NAVAL POSTGRADUATE SCHOOL
December, 1997

Author:

Kevin J. Quinn

Kevin J. Quinn

Approved by:

Raymond P. Shreeve

Raymond P. Shreeve, Thesis Advisor

Garth V. Hobson

Garth V. Hobson, Second Reader

Gerald H. Lindsey

Gerald H. Lindsey
Department of Aeronautics and Astronautics

ABSTRACT

Pressure-sensitive paint measurement on a transonic compressor rotor required the prior development of phase-locked cumulative imaging using a disk-rotor driven by a high-speed Hamilton-Standard turbine as a developmental test-bed. The turbine was installed in a protective housing in the Gas Dynamics Laboratory and connected to an 8000 cu ft, 300 psi air supply. An hydraulic pump provided bearing lubrication. A once per revolution trigger signal was produced from a light-emitting diode and PIN photodiode pair. The imaging system consisted of an intensified CCD video camera externally triggered by the 1/rev signal via a waveform shaping circuit designed for the present application. Images were captured at camera gate speeds calculated to eliminate pixel blur and image integration times were varied to optimize image intensity and spatial resolution. Structural and modal analyses of the disk-rotor were conducted and a simplified numerical model of the flow was computed. Ratioed, colored images were produced for wheel speeds to 20,000 RPM. The effect of the radially varying stagnation temperature was evident, underscoring the importance of quantifying and accounting for the PSP temperature sensitivity so that quantitative pressure data may be obtained. Recommendations for a follow-on program are reported.

TABLE OF CONTENTS

I. INTRODUCTION	1
A. SUMMARY OF RESEARCH	1
B. THEORETICAL BACKGROUND	2
C. CONCEPT AND APPROACH	3
II. FLOWFIELD CHARACTERIZATION	5
A. OVERVIEW	5
B. COMPUTATIONAL DEVELOPMENT	5
1. Code Overview	5
2. Grid Generation	6
3. Boundary Conditions and Computational Setup	6
4. Computational Results	6
III. EXPERIMENTAL SETUP AND CONSIDERATIONS	13
A. HAMILTON STANDARD TURBINE-DRIVEN FUEL PUMP	13
B. DISK-ROTOR	15
C. ONCE-PER-REVOLUTION (1/REV) TRIGGERING	15
D. IMAGE ACQUISITION SYSTEM	16
1. CCD Camera and Control Unit	16
2. Illumination System	17
3. Frame Grabbing and Image Display	17
4. Monostable Wave-Shaping Circuit	17
5. Image Capture and Processing	19
IV. EXPERIMENTAL PROCEDURE	31
A. ROTOR PREPARATION	31
B. CAMERA AND LAMP PLACEMENT	31
C. FOCUS AND GATING	31
D. "WIND-ON" ACQUISITION	32
E. DARK CURRENT ACQUISITION	32
F. "WIND-OFF" ACQUISITION	33
G. POSTPROCESSING	33
V. RESULTS AND DISCUSSION	35

VI. CONCLUSIONS AND RECOMMENDATIONS	43
APPENDIX A. OVERFLOW NUMERICAL SOLUTION	45
A. CODE INPUT	45
B. SOLUTION METHOD	46
C. SOLUTION OUTPUT	48
D. PROGRAM CODES	48
APPENDIX B. TURBINE APPARATUS MECHANICAL DRAWINGS	61
APPENDIX C. CIRCUIT DESIGN	67
APPENDIX D. 4MIP TOOL SCRIPTED MACROS	71
APPENDIX E. DISK STRESS ANALYSIS AND ROTOR REDESIGN	75
A. STRESS ANALYSIS	75
B. MODAL ANALYSIS	76
C. DISK-ROTOR REDESIGN	77
LIST OF REFERENCES	83
INITIAL DISTRIBUTION LIST	85

LIST OF FIGURES

Figure 1	Computational Grid	8
Figure 2	Streamline Trace of Flow About Rotating Disk -- 333 Hz / Case 4.....	8
Figure 3a	P/P _o Distribution at 166 Hz Disk Frequency.....	9
Figure 3b	T _t /T _{to} Distribution at 166 Hz Disk Frequency.....	9
Figure 4a	P/P _o Distribution at 266 Hz Disk Frequency.....	10
Figure 4b	T _t /T _{to} Distribution at 266 Hz Disk Frequency.....	10
Figure 5a	P/P _o Distribution at 285 Hz Disk Frequency.....	11
Figure 5b	T _t /T _{to} Distribution at 285 Hz Disk Frequency.....	11
Figure 6a	P/P _o Distribution at 333 Hz Disk Frequency.....	12
Figure 6b	T _t /T _{to} Distribution at 333 Hz Disk Frequency.....	12
Figure 7	PSP Experimental Setup.....	20
Figure 8	Four-View Aspect of Hamilton Standard TPC-13 Turbine Mount.....	21
Figure 9	Hamilton Standard TPC13 Turbine Dimensional Illustration.....	22
Figure 10a	Spin Chamber Side-View with Protective Front Plate Installed.....	23
Figure 10b	Spin Chamber Views; Turbine Uninstalled (Top) and Installed (Bottom).....	23
Figure 11	Turbine Lubrication System.....	24
Figure 12	Dual-Bladed Disk-Rotor.....	25
Figure 13	Triggering Circuit Diagram.....	26
Figure 14	LED / Photodiode Pair and Mounting Bracket.....	27
Figure 15	ORIEL Camera Filter #53590 Characteristics	28
Figure 16	Waveform Shaping Schematic.....	29
Figure 17	Waveshaping, Image Control, and Postprocessing Components.....	30
Figure 18	Plot of Linear RGB Pseudocoloring Functions and Color Palette.....	34
Figure 19	Ratioed Intensity Image at 166 Hz Disk Frequency	38

Figure 20	Ratioed Intensity Image at 266 Hz Disk Frequency	39
Figure 21	Ratioed Intensity Image at 285 Hz Disk Frequency	40
Figure 22	Ratioed Intensity Image at 333 Hz Disk Frequency	41
Figure 23a	Vertical I_o/I Distribution at Horizontal Station X = 15% Blade Chord...	42
Figure 23b	Vertical I_o/I Distribution at Horizontal Station X = 50% Blade Chord...	42
Figure 23c	Horizontal I_o/I Distribution at Vertical Station Y = 83% Disk Radius....	42
Figure A1	333 HZ Case Convergence History	49
Figure B1	Turbine Mounting Bracket Detailed Drawing; Side / Bottom Views	62
Figure B2	Turbine Mounting Bracket Detailed Drawing; Front / Rear Views.....	63
Figure B3	Turbine Mounting Bracket / Spin Chamber Interface Drawing.....	64
Figure B4	Light Emitting Diode / Photodiode Bracket Detailed Drawing.....	65
Figure B5	Turbine Connecting Flange Detailed Drawing.....	66
Figure C1	BCD Counter Circuit	68
Figure C2	Power Supply Circuit	69
Figure C3	Proposed One-shot Monostable Waveshaper Circuit Schematic.....	70
Figure E1	Disk-Rotor Stress Distributions	78
Figure E2	NASTRAN Disk-Rotor Finite-Element Model	79
Figure E3	Disk-Rotor Modal Characteristics.....	80
Figure E4	Constant Stress Disk-Rotor Thickness Distribution	81
Figure E5	Disk-Rotor Redesign Drawing	82

LIST OF TABLES

Table 1	Computational Solutions and Similarity Parameters	7
Table 2	Turbine Bearing Lubrication Limitations	14
Table 3	Shim Requirements for Turbine Alignment by Attachment Hole	14
Table 4	1/REV Trigger Component Specifications	16
Table 5	Gate Speed Settings Varying Spatial Resolution and Wheel Speed	18
Table 6	File Naming Structure	19
Table 7	Imaging Data Comparison by Case	36
Table A1	Grid Domain and Coordinate Relation	45
Table A2	OVERFLOW Boundary Conditions	45
Table A3	Modified OVERFLOW Subroutines	46
Table E1	Disk-Rotor Modal Frequencies	76

I. INTRODUCTION

With increasing emphasis in the design of turbomachinery on three-dimensional numerical computation, validation of new design and analysis techniques has become critical. Toward that goal, the development of a pressure-sensitive paint (PSP) measurement technique has been initiated at the Naval Postgraduate School (NPS). The technique is to be applied as a new diagnostic in an experimental appraisal of the numerical methods used in the design of a rotor for the NPS Turbopropulsion Laboratory transonic compressor. Following a thorough evaluation of the numerical methods used to arrive at the present geometry, including the validation of computational off-design solutions, new designs can be attempted which optimize benefits from blade sweep and tip clearance flows. Thus, the full experimental validation of the new rotor design is key to attaining higher performance designs at lower test and evaluation costs. The present study, building on experience gained in preceding work, involved the construction and use of a turbine-driven PSP test-bed to develop the measurement technique. PSP images were successfully acquired from a rotor operating at sonic tip speeds, and problems which must be solved before measurements can be made on the compressor rotor were clearly defined. A summary of previous related research at NPS and a brief overview of the principles of the PSP measurement technique are provided as an introduction to the present study.

A. SUMMARY OF RESEARCH

The design of a stage for the NPS transonic compressor test rig by Sanger (1996) used a quasi-three-dimensional Euler code using distributed body forces to model viscous effects. Final stator and rotor blade aerodynamic geometries were derived iteratively to attain the design goals. The stage was machined by Turbocam Inc. to coordinates calculated for the unloaded condition. In preparation for test of the Sanger stage, a study by Reid (1995) evaluated the process described by Sanger and returned the NPS test rig to operational condition.

Concurrently, the commitment to PSP measurement at NPS was initiated by Seivwright (1996) in a shock-boundary layer interaction study of a flat plate in an under-expanded free-jet. PSP was used to map the surface pressure field. The flat plate study enabled the application of PSP in a rotational experiment, conducted by Varner (1995). Elsewhere Burns et al (1995) and Hubner et al (1996) reported using PSP in the rotating frame. In the Varner study, a flat-plate disk-rotor powered by an electric motor was used to attempt PSP pressure measurements at a transonic rotor condition. Imaging requirements

were identified and a phase-locked circuit was developed to acquire data. Qualitative measurements were obtained at subsonic rotor-tip speeds (13,000 RPM) and calibration studies were conducted, providing the impetus for a careful evaluation of the technique and application in a higher speed regime.

B. THEORETICAL BACKGROUND

The fundamental mechanism in PSP is the photoluminescent characteristic of an activated ‘probe’ molecule; platinum octaethylporphyrin (PtEOP) in the present study. The probe molecule achieves activated energy states, both in singlet and triplet form, through the absorption of excitation energy from ultraviolet light stimulation. Photoluminescence is the radiant energy emitted when a molecule returns from an excited triplet energy state to a ground, singlet state. This process is quenched when collisions occur between two triplet-state molecules with opposite electron spin orientation. The collision promotes a non-radiating transition of the probe molecule from its triplet to its ground state. Therefore, the photoluminescent transition and molecular collision transition processes compete.

PtEOP is predisposed to excite to a triplet state when activated, therefore tending to phosphoresce when it returns to its ground state. However, oxygen in the atmosphere occurs naturally in an excited triplet state with an opposite electron spin orientation, and quenches the phosphorescent process when collisions between it and the probe molecule occur. The rate at which these collisions occur is dependent on the oxygen partial pressure, which, in turn, is dependent on atmospheric pressure. Stern-Volmer related the rate constants of the processes involved to the intensity of the photoluminescence, and derived an inverse linear relation between intensity (I) and pressure (P) when referenced to a control. Equation 1 gives this relation, showing a dependency of the rate constants on temperature (T), where the subscript zero is a reference (usually ““wind-off””) condition.

$$\frac{I_0}{I} = A(T) + B(T) \frac{P}{P_0} \quad (1)$$

By combining the PtEOP in a oxygen-permeable silicon resin binder, application to an aerodynamic surface in the form of paint allows the static pressure on the coated surface to be determined by relating the intensity of the reference or “wind-off” condition to the flow or “wind-on” condition. The surface temperature must be constant for both the “wind-off” and “wind-on” images to be related through the A and B rate constants in this form. Seivwright (1995) and Kavandi (1990) provide thorough discussion of the mechanics of phosphorescence and oxygen quenching.

C. CONCEPT AND APPROACH

In the present study, the development of a high-speed test-bed for rotary PSP measurements and refinement of the image acquisition technique enabled PSP results to be obtained at four wheel speeds. The installation of a high-speed air-driven turbine to rotate a dual-blade disk-rotor provided the ability to obtain PSP images at near transonic conditions. Mechanical and vibrational characteristics of the disk-rotor were addressed. The use of a phase-locked, monostable-pulse circuit triggered by an amplified once-per-revolution pulse, allowed image acquisition with a charge-coupled-device (CCD) camera. Pixel blur and image integration time issues were solved and a process for the acquisition of images at optimum resolution was determined. Circuitry requirements for higher speed imaging and a disk-rotor redesign to enable higher speeds were identified. Most importantly, the association of image intensities to radially increasing stagnation temperature was verified.

In the present document, Section II discusses the flowfield produced by a rotating disk in a stationary flow and presents the results of a Navier-Stokes numerical computation. Section III details the experimental setup and test considerations. Section IV outlines the procedure used in obtaining four high-speed, ratioed images at progressively increased rim speeds. The results are discussed in Section V and conclusions and follow-on research recommendations are given in Section VI. Appendices A through E provide details of the numerical code used, engineering drawings, postprocessing software scripting, circuit specifications, and proposed circuit and disk-rotor redesigns.

II. FLOWFIELD CHARACTERIZATION

A. OVERVIEW

The flow created by a finite, high-speed rotating disk within an otherwise stationary environment is viscous, compressible, and three-dimensional (3D). The surface friction forces induce radial and tangential velocity components on the fluid in the vicinity of the disk surface. For continuity, the radially outflowing fluid near the disk is fed by an axially inflowing fluid mass along the rotational axis. The disk is therefore a centrifugal type pump. An analytic solution for the laminar boundary layer case derived by Schlichting (1960) assumed incompressible flow and zero radial pressure gradient. Calculating Reynold's number using disk radius as the length scale,

$$Re = \frac{\omega R^2}{\nu} \quad (2)$$

where ω is rotational frequency and ν is kinematic viscosity, Schlichting showed close agreement between analytic and experimental displacement thicknesses for both laminar and turbulent conditions. The transition from laminar to turbulent flow was shown to occur at a Reynold's Number of approximately 3×10^5 .

The higher disk rotational speeds in the present application give rise to a turbulent boundary layer. To account for compressibility and turbulence and not be constrained to thin viscous layers, a numerical solution was undertaken using the external-flow 3D Navier-Stokes code OVERFLOW. The computational development and solutions for varying disk rotational frequencies are discussed below.

B. COMPUTATIONAL DEVELOPMENT

1. Code Overview

OVERFLOW solves the three-dimensional Navier-Stokes equations implicitly using finite differencing and block tri-diagonal solvers. The OVERFLOW code is written in Fortran programming language for workstation use. The code makes use of an input file which defines the time step, a minimum Courant-Freidrichs-Levy (CFL) number, external flow boundary conditions and the solution variables. Viscous and turbulent terms are also adjusted within the input file. In summary, the physical domain is input, matched to the boundary conditions, and transformed to the computational domain where the equations are

solved. The code was altered to accommodate the rotating boundary condition, compiled, and run on a Silicon Graphics work-station. Specifics of the code and input / output file format are presented in Appendix A.

2. Grid Generation

A cylindrical 31x31x41 grid with a length scale equivalent to one disk radius was developed using *GRIDGEN*. As flowfield characterization was the initial purpose, the complexity of defining the blade geometries was not undertaken at this stage since it would have required an overlapped-grid technique. Therefore, the physical problem solved was that of a planar rotating disk, with an axisymmetric solution. A hyperbolic grid distribution was applied in the axial direction for fine resolution of the disk boundary layer and swirl development. Similarly, a hyperbolic distribution of grid lines was applied radially in order to resolve the flow near the rim. The grid domains were blocked in *GRIDGEN* such that the I,J,K directions were consistent with a cylindrical coordinate system and an OVERFLOW J,K,L notation. The grid correlation is given in Appendix A, Table A1. The grid is shown in Figure 1.

3. Boundary Conditions and Computational Setup

Accurately defining the inlet and rotating plane boundary conditions was critical. Although the code required an inflow Mach number to avoid singular calculations, it was found experimentally that $M_{in} = 0.015$ gave a converged solution. Therefore, the flow effectively was stationary and the inflow Mach number was assumed to have negligible effect on the results. To effect the radially-varying velocity distribution at the disk, alteration of the code was required. The viscous, no-slip boundary condition subroutine was edited, imposing tangential velocities on the grid points defining the disk surface. This change required the upstream flow to match the velocity at the disk, which therefore acted as a strong source term in the computation. Density extrapolation occurred prior to the velocity extrapolation and therefore provided accurate density updates. Varying the rotational frequency required editing the scalar in the boundary condition and recompiling the code. Additional notes on the boundary conditions can be found in Appendix A, including the edited subroutines. The solution method was fully viscous and turbulence was estimated using a Baldwin-Lomax turbulence model (Buning, 1995).

4. Computational Results

Solutions were obtained for four test cases corresponding to the disk rotational speeds tested experimentally. Table 1 summarizes the computational solutions obtained and lists the corresponding similarity parameters. Figure 2 represents a streamline trace from the 333 Hz

solution and exemplifies the overall flow structure. Figures 3 through 6 detail the normalized static pressure and normalized stagnation temperature distributions for the 166 Hz, 266 Hz, 285 Hz, and 333 Hz cases respectively. The three dimensional figures display the axisymmetric flowfield, its contours in the radial plane and the solution on the disk.

Frequency (f)	RPM (N)	Wheel Speed (U)	Reynold's No (Re)	Mach No (M)
166 Hz	10,000 rpm	521.5 fps	1.654e6	0.442
266 Hz	16,000 rpm	835.7 fps	2.650e6	0.709
285 Hz	17,000 rpm	895.4 fps	2.839e6	0.755
333 Hz	20,000 rpm	1046.2 fps	3.317e6	0.865

Table 1. Computational Solutions and Similarity Parameters

The solutions in Figures 3 through 6 show the entire disk and one peripheral grid location beyond the rim to accentuate maxima found at the disk rim. Convergence history data are given in Appendix A. Close agreement was found between the Mach number (0.442) at the disk rim at 166 Hz to that calculated incompressibly using the method of Schlichting. Evident in these solutions is the small pressure variation exhibited across the disk in all cases, in contrast to strong stagnation temperature changes. For the ambient laboratory temperature of 69°F, the effective recovery temperature on the disk surface was estimated to range from 100°-150°F. The computed pressure ratios of .98 to 1.01 reflect the inefficiency of the flat disk as a pump and justify the use of blading as small shock generators to generate a measurable event.

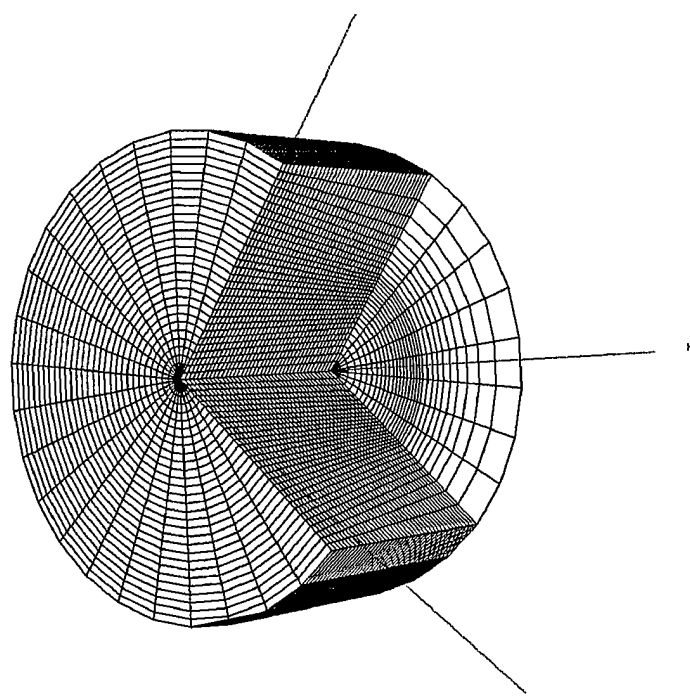


Figure 1. Computational Grid (31 x 31 x 41)

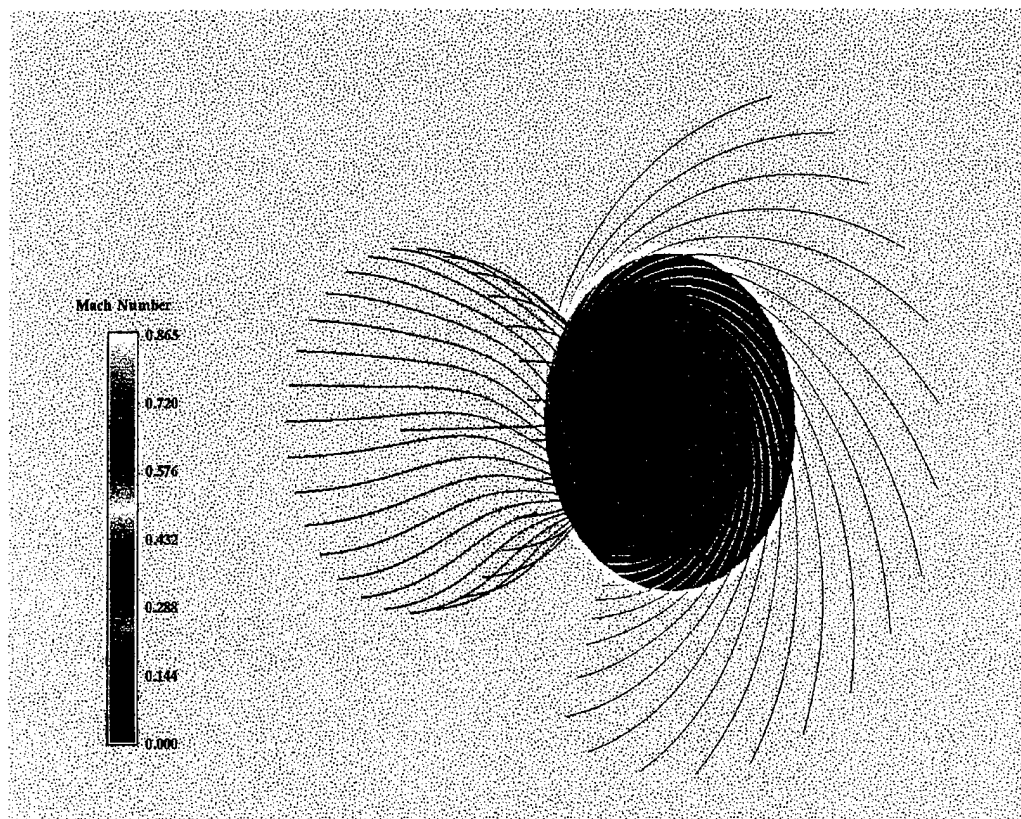


Figure 2. Streamline Trace of Flow About Rotating Disk
333 Hz / Case 4

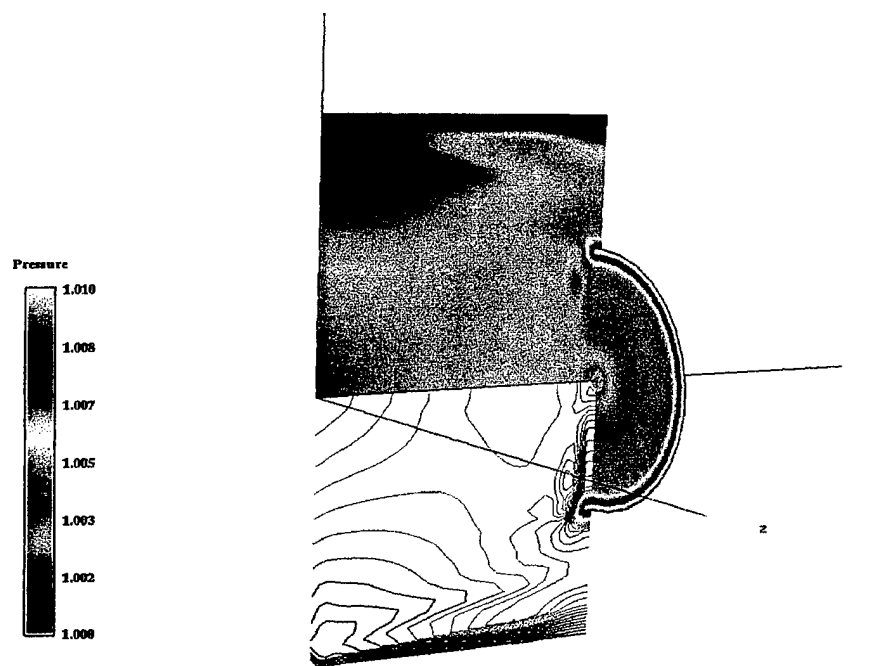


Figure 3a. $\frac{P}{P_0}$ Distribution at 166 Hz Disk Frequency

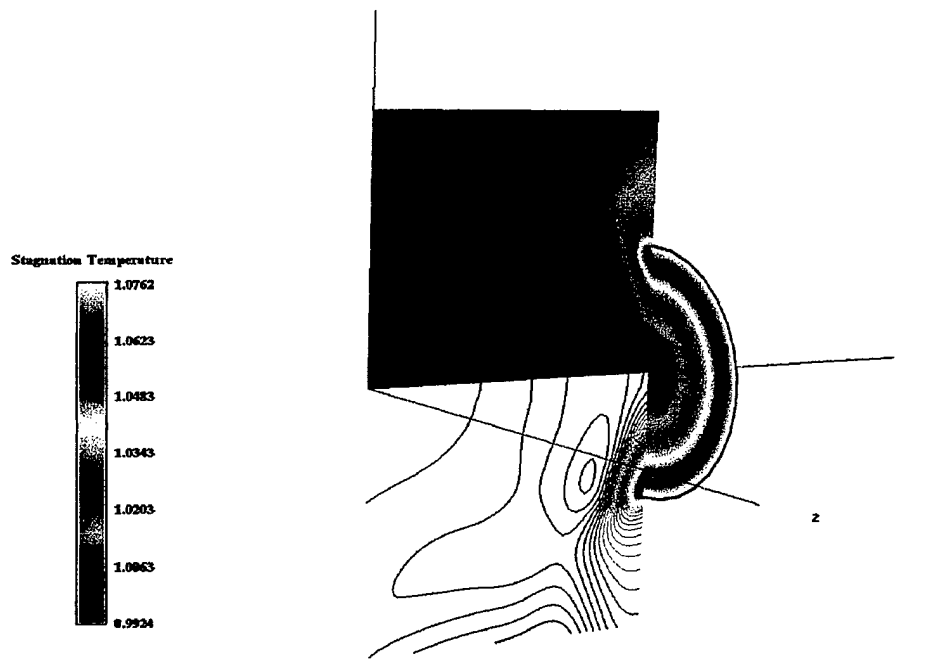


Figure 3b. $\frac{T_t}{T_{to}}$ Distribution at 166 Hz Disk Frequency

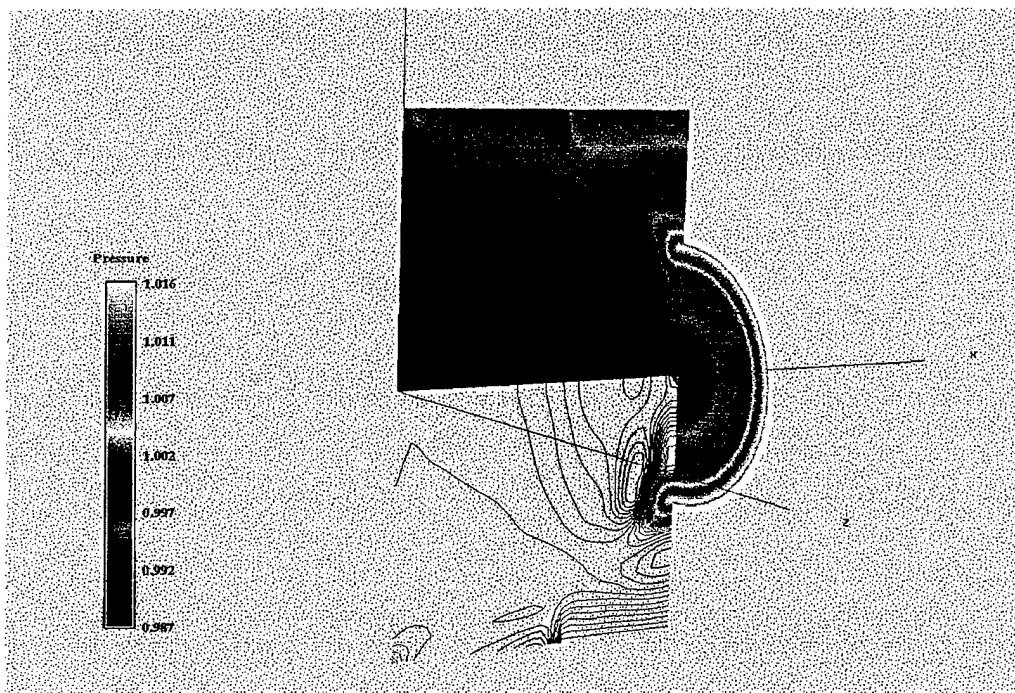


Figure 4a. $\frac{P}{P_o}$ Distribution / 266 Hz Disk Frequency

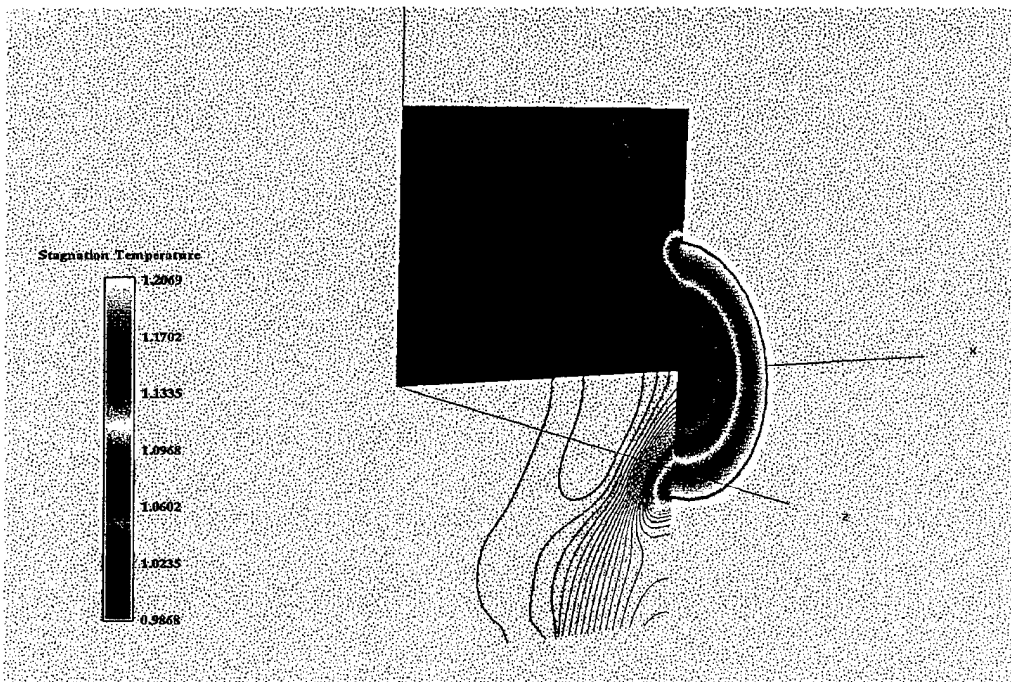


Figure 4b. $\frac{T_t}{T_{to}}$ Distribution / 266 Hz Disk Frequency

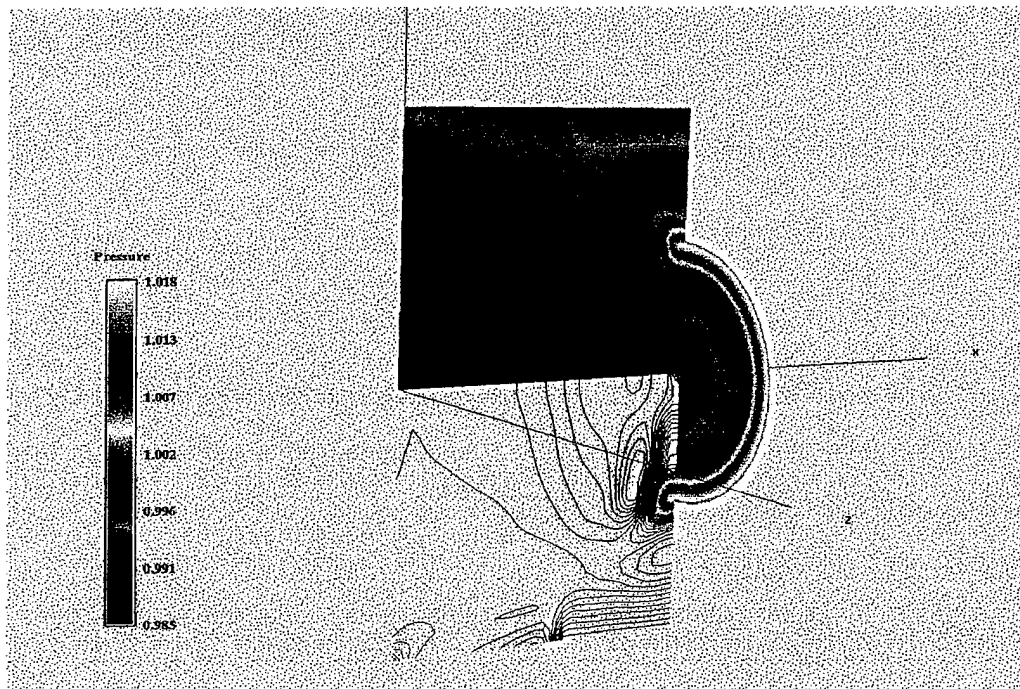


Figure 5a. $\frac{P}{P_0}$ Distribution / 285 Hz Disk Frequency

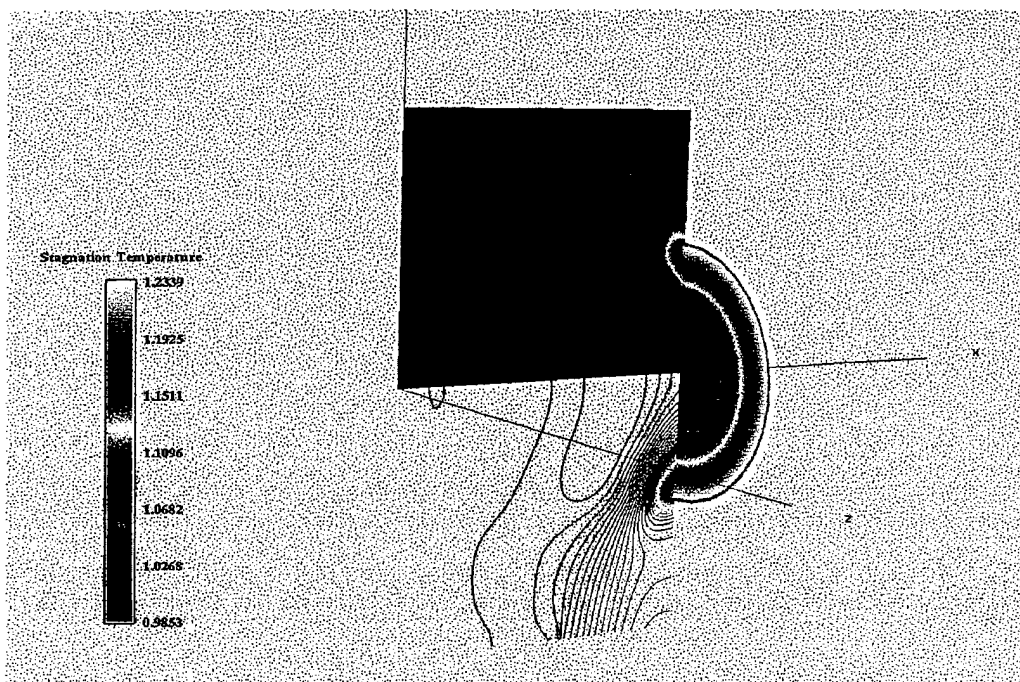


Figure 5b. $\frac{T_t}{T_{to}}$ Distribution / 285 Hz Disk Frequency

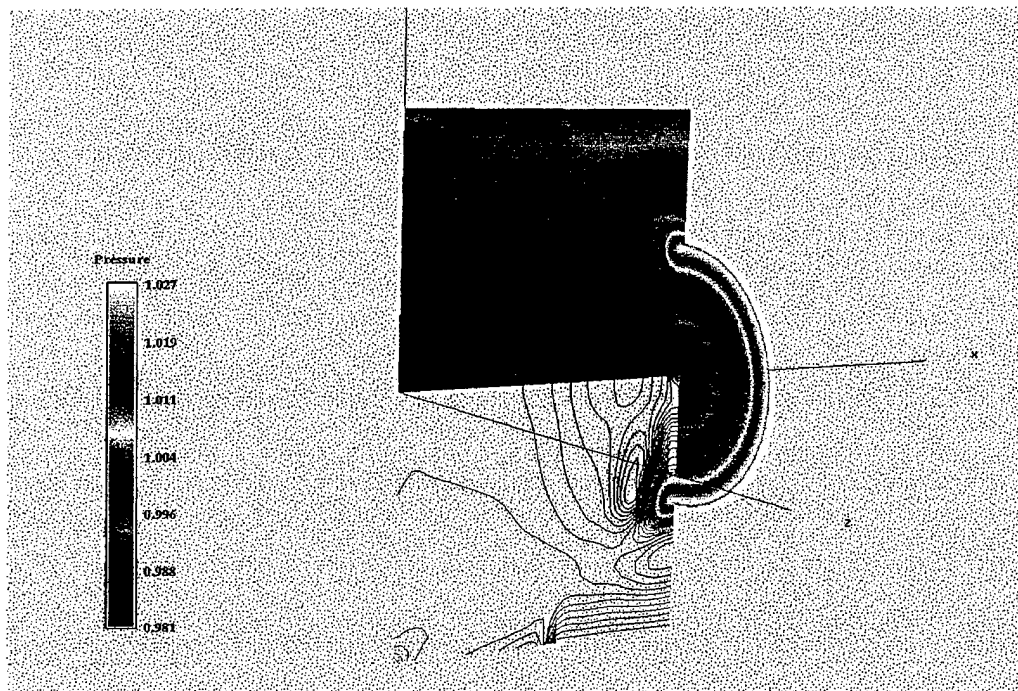


Figure 6a. $\frac{P}{P_o}$ Distribution / 333 Hz Disk Frequency

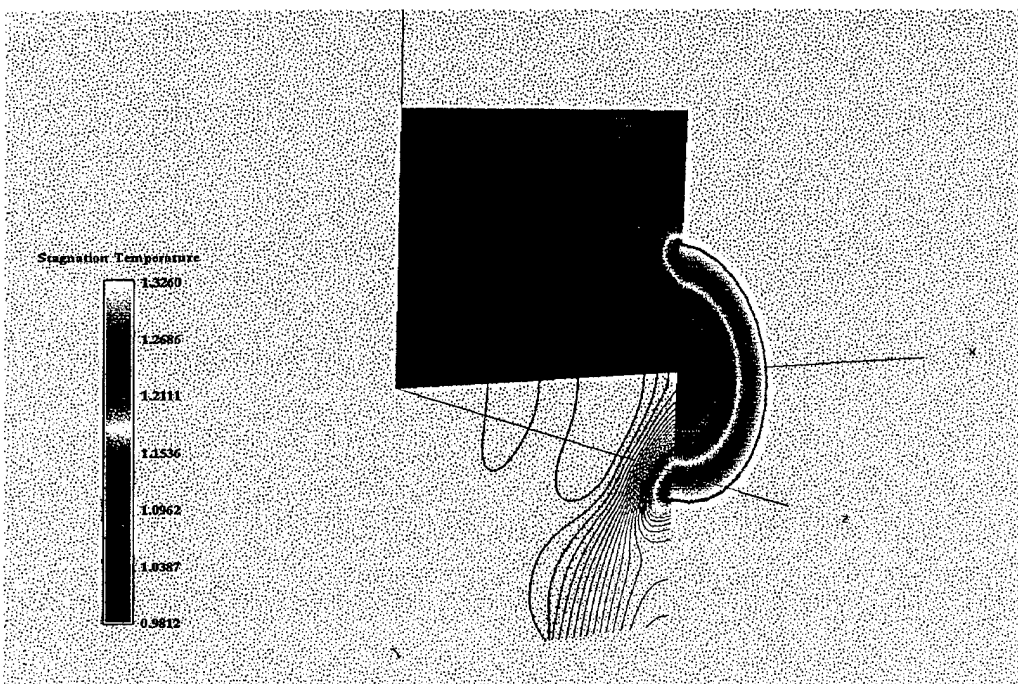


Figure 6b. $\frac{T_t}{T_{to}}$ Distribution / 333 Hz Disk Frequency

III. EXPERIMENTAL SETUP AND CONSIDERATIONS

Figure 7 shows the experimental setup. An air-powered turbine was used to rotate the dual-blade disk-rotor. The rotor was continuously and evenly illuminated and the steady, relative pressure distribution was measured by integrating a series of low light image captures, with the final image representing an averaged intensity distribution. A once-per-revolution pulse produced by a LED / photodiode pair triggered the image acquisition system through a phase-locked, monostable pulse circuit. The acquisition system consisted of a charge-coupled device (CCD) camera and control unit (CCU), operating with a video frame grabber / image processing system. A function generator provided triggering for "wind-off" and dark current imaging. A description of the system components follows.

A. HAMILTON STANDARD TURBINE-DRIVEN FUEL PUMP

To attain a transonic condition at the tip of the disk-rotor, a Hamilton Standard turbine-driven fuel pump, Model TPC-13, was mounted within an existing spin chamber. Powered by a 300 psi, 8000 cu ft air supply, the pump was capable of providing wheel speeds to 28,500 rpm continuously (Hamilton Standard, 1968). Turbine mounting, bearing lubrication, air supply, and disk-rotor alignment were the primary considerations in the installation and are discussed separately.

A box cradle was designed and built from 3/4 inch 6061-T6 aluminum plate to mount the turbine to a shelf inside the protective spin chamber. The turbine and mount are shown in Figures 8 and 9. The spin chamber described by Varner (1995) was adapted to accommodate the turbine and cradle and the chamber assembly was secured to a heavy steel mounting table inside the Gas Dynamics laboratory. Air supply and bearing lubrication plumbing were provided to the turbine housing. Figure 10 shows the housing and turbine in place. The mechanical drawings for the turbine mount are given in Appendix B.

Due to the high rotational speeds, turbine bearing lubrication was critical. Reviewing lubrication requirements of similar high performance type bearings and referring to the drawings for the bearing geometry (Hamilton Standard, 1968), a DN value of 1,050,000 mm-rpm was determined. This allowed a circulating oil lubrication system to be applied (Torrington Company). Although the turbine was designed to use diverted aviation type fuel as the bearing lubricant, military specification MIL-L-7808 lubricating oil was substituted. Circulation oil pressure was provided by a flushed and converted hydraulic pump, capable of providing oil pressures to 3000 psi. Because this far exceeded the turbine design limitations, careful control of the oil pressure to the bearings was observed. A maximum pressure of 60 psi was applied which forced oil through the bearing housing to the sump return line. A

temperature-sensing thermocouple was installed in the return line prior to the sump to monitor bearing temperature. Figure 11 shows the lubrication pump setup and Table 2 summarizes the turbine operating limits observed in the present testing (Hamilton Standard, 1968).

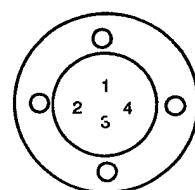
Parameter	Operating Limit
Operating Speed	28,500 rpm ¹
Outlet Oil Temperature	175°F
Inlet Oil Pressure	60 psia

Note (1): A bearing limitation. The disk-rotor was stress limited to 20,000 RPM.

Table 2. Turbine Bearing Lubrication Limitations

The air supply was plumbed to the turbine using two-inch steel piping and a flexible coupling. A threaded connecting flange required to mate the air supply plumping with the turbine air inlet was manufactured from stainless steel and secured with a Marman clamp. The detailed drawings for the part are given in Appendix B. The air supply was controlled using a regulator at the control panel. A lock nut was incorporated to constrain the air supply valve once test speed was attained, thereby limiting speed variation during the test.

Following installation, the disk-rotor was aligned to the turbine drive flange. A machine indicator with a ± 0.001 inch resolution was clamped to the mounting bracket for reference. Axial runouts at the disk rim and mid-radius locations were measured and shim washers were placed between the disk and drive flange to bring the axial rim runout to within 0.005 inches. Table 3 lists the shims required at each attachment hole, numbered counterclockwise facing the turbine attachment flange.



Attachment Point	Alignment Requirement
1	0.005"
2	0.015"
3	0.000"
4	0.003"

Table 3. Shim Requirements for Turbine Alignment by Attachment Hole

B. DISK-ROTOR

The test disk-rotor, pictured in Figure 12, was built and tested previously by Varner, (1995). It consisted of a .25 inch thick, 6061 aluminum disk with two opposing 2.18" W x .125" H blades designed to produce a measurable pressure event. The disk was adapted to fit the turbine drive flange for the present study. A structural analysis was undertaken and 20,000 rpm was found to give the radial stress structural limit. A summary of the analysis is presented in Appendix E. The radial and tangential stress distributions based on the solution for a disk with a central hole (Baumeister, 1967), are shown in Figure E1. A MSC NASTRAN¹ modal analysis of the disk-rotor was also completed. Plate elements were used in the formulation. The disk hub was constrained in the three translational directions and in the transverse and lateral rotational planes. Figure E2 depicts the NASTRAN mesh geometry and Table E1 lists the natural frequencies and the corresponding modes. The results show modes with complementary frequencies due to the symmetry of the model. The primary bending and flapping modes were shown to occur at low frequencies. A pitching mode, however, was found at 313 Hz and turbine operation in the vicinity of this frequency was monitored for excessive vibration. Figure E3 shows normalized deformation contours for the primary modes and exemplifies the solution symmetry in the second and third bending modes.

C. ONCE-PER-REVOLUTION (1/REV) TRIGGERING

The 1/rev triggering circuit is shown in Figure 13. A light emitting diode (LED) (type SLA580LT3F) excited a planar-diffused PIN photodiode (PIN 3CD) through a 3/32 hole in the disk-rotor. An analog voltage pulse was generated through a basic photo-conductive circuit (UDT Sensors, 1996). The pulse was relayed first to an operational amplifier and then to a wave-shaping circuit to produce a trigger for the CCD camera and to a counter to record the wheel frequency. LED and photodiode characteristics are provided in Table 4. Simplified radiometry (radiance) and photometry (luminance) conversions (Roberts, 1993) were applied to ensure the pulse width and amplitude supplied to the wave-shaping circuit for triggering were sufficient over the operational frequency spectrum. Additionally, the response of the photodiode circuit was set to a lower order (0.01 μ sec) than the gate speed of the camera (0.1 μ sec).

¹MSC NASTRAN for WINDOWS provided under license.

Model	Characteristic	Specification
LED SLA580LT3F	Luminous Emission Wavelength Intensity FWD / REV Voltage	2000 mcd 660 nm 2.5 V / 4 V
PIN 3CD Photodiode	Responsivity Capacitance (@ 28V) Breakdown Voltage Rise Time ($2.2R_L C_J$)	0.35 amps / Watt 8.5 pf 50 V 37.4 nsec

Table 4. 1/REV Trigger Component Specifications

The LED, photodiode and associated wiring were cased in cylindrical housings (electrically non-conductive for the photodiode casing) and fit into a mounting bracket, shown in Figure 14. The bracket, machined from .375 inch aluminum plate, was attached to the turbine mount. Adjustment set screws in the bracket allowed axial translation of the LED and photodiode casings. Mechanical drawings are given in Appendix B.

D. IMAGE ACQUISITION SYSTEM

1. CCD Camera and Control Unit

The images were acquired with an intensified, electronically-gated Xybion ISG-350 CCD camera and its associated CCU (Varner,1995). The camera was fitted with a 75mm, f1.4 Cosmicar™ television lens and Oriel™ interference filter #53590. The camera was focused manually and a 10mm extension for the lens was required for the present application. The camera was secured to a tripod which allowed fine adjustment of the camera position. Characteristics of the CCD camera are given in the ISG-350 users manual (Xybion Electronic Systems, 1992). The interference characteristics of the filter are shown in Figure 15.

The 8-bit camera dynamic range was maximized by setting the CCU camera control switch to AUTO, which set a 38mV black level and OdB camera gain (Xybion Electronic Systems,1990). This gain setting avoided potential image noise created by increased gain settings. However, part of the 8-bit resolution was lost due to heat-generated noise within the CCD elements, which required the black level to be set at the noise band threshold. Because full video potential was represented from 0-714mV, a portion of the video resolution was lost. The intensifier gain control on the CCU-01 was set manually to a maximum. Due to short gate durations, discussed in the following, this setting amplified the low intensities 'seen' by the camera prior to their distribution into the CCD array, and eliminated the need for cumbersome intensifier gain measurements. In addition, the lens aperture was set full open to the $f=1.4$ setting, maximizing the amount of light introduced to the camera intensifier.

To make full use of the video resolution present, pixel distortion in the integrated image was eliminated by gating the camera to freeze the movement of the disk-rotor blade to within one pixel of travel. Table 5 lists the gate speed requirements for varying spatial resolutions and angular frequencies at the limiting horizontal video resolution of 752 pixels. The gate speed, a function of the rotational speed of the disk, was set manually using the CCU-01. The manual gate adjustment was made while displaying the signal on a digital oscilloscope via the gate readout BNC connector on the CCU-01 rear panel.

2 . Illumination System

Paint illumination was produced using a 1000-Watt quartz tungsten-halogen lamp, Model 66200, equipped with an F/0.7 lens and controlled by its associated Oriel lamp controller, Model 6405. The lamp was filtered using an ORIEL blue-gel filter #66228 and ORIEL interference filter #57521 yielding a 380nm excitation source. Lamp controller voltage was maximized, sacrificing filament lifetime for maximum illumination intensity. Illumination source and filtering characteristics are described by Seivwright (1996). Documented lamp ramp-up times (Oriel Corporation, 1992) were conservatively observed prior to image acquisitions.

3 . Frame Grabbing and Image Display

An EPIX 4MEG Video Model 12 integrated-circuit board and EPIX 4MIP V2.8 software were installed in a 120MHz clock speed Pentium™ personal computer. Video resolution was set to 752H x 480V pixels which configured the video memory into eleven buffered segments. Each image was downloaded to the frame-grabber board after the camera image integration period. The dynamic range of the frame-grabber board was adjusted to match that of the camera (EPIX Incorporated, 1993). Acquired images were displayed for post-processing on a Sony PVM 1954Q color video monitor. The monitor allowed red/green/blue (RGB) inputs from standard RS-170 video input. Monitor channel A / RGB was used (Sony Corporation, 1993). At the conclusion of the present work, the requirement for increased video memory was identified and the frame-grabber board was upgraded to EPIX 4M12-IM-64/430-14.3 (64 megabytes of memory) which, at the same resolution, segmented into 178 video buffers. Additionally, the software upgrade to EPIX 4MIP for WINDOWS95™ V3.2 was installed.

4 . Monostable Wave-Shaping Circuit

The amplified triggering pulse produced by the LED / photodiode / op-amp circuit was converted to a 5V active-low camera trigger through a previously developed wave-shaping circuit (Varner, 1995). BNC connections were made as shown in Figure 7.

Frequency (Hz)	100	133	166	200	233	250	266	285	300	333
Wheel Speed RPM	6000	7980	9960	12000	13980	15000	15960	17100	18000	19980
Rim Velocity (fps)	314.15	417.83	521.50	628.31	731.99	785.39	835.66	895.35	942.47	1046.15
Gate Setting (usec)										
0.7	1.09852	0.82595	0.66176	0.54926	0.47146	0.43940	0.41297	0.38544	0.36617	0.32988
0.725	1.06064	0.79747	0.63894	0.53032	0.45521	0.42425	0.39873	0.37215	0.35354	0.31851
0.75	1.02528	0.77089	0.61764	0.51264	0.44003	0.41011	0.38544	0.35975	0.34176	0.30789
0.775	0.99221	0.74602	0.59771	0.49610	0.42584	0.39688	0.37301	0.34814	0.33073	0.29796
0.8	0.96120	0.72271	0.57904	0.48060	0.41253	0.38448	0.36135	0.33726	0.32040	0.28865
0.825	0.93208	0.70081	0.56149	0.46604	0.40003	0.37283	0.35040	0.32704	0.31069	0.27990
0.85	0.90466	0.68020	0.54497	0.45233	0.38826	0.36186	0.34010	0.31742	0.30155	0.27167
0.875	0.87881	0.66076	0.52940	0.43940	0.37717	0.35152	0.33038	0.30835	0.29293	0.26390
0.9	0.85440	0.64241	0.51470	0.42720	0.36669	0.34176	0.32120	0.29979	0.28480	0.25657
0.925	0.83131	0.62504	0.50079	0.41565	0.35678	0.33252	0.31252	0.29168	0.27710	0.24964
0.95	0.80943	0.60860	0.48761	0.40471	0.34739	0.32377	0.30430	0.28401	0.26981	0.24307

¹ Spatial resolution of the blade chord in pixels normalized by the horizontal pixel resolution ('/52 pixels).

Table 5. Gate Speed Settings Varying Spatial Resolution and Wheel Speed (μsec per pixel)

This circuit consisted of a waveshaper, voltage divider / inverter, TTL logic control gate, and monostable pulse circuit. Figure 16 details the pulse shaping for each circuit element and Figure 17 shows the image acquisition instrumentation setup. The waveshaper and voltage divider/inverter converted the amplified pulse to a 5V high TTL pulse. This was input both to the TTL logic gate and to a frequency counter for wheel frequency indication. The TTL pulse at the TTL logic gate was relayed to the camera only on external initiation from a Wavetek function generator pulse to the monostable pulse circuit. The monostable pulse circuit generated two 5V high TTL pulses, widths of which were dependent on variable RC time constants. The first was the image-inhibit period, during which the camera was triggered and images integrated. The second allowed the completed integrated image to be downloaded to the frame grabber. The monostable pulse circuit was modified from its previous configuration to generate longer time constants, up to 35 seconds. Additionally, a binary-coded decimal (BCD) counter was built to count the trigger pulses relayed to the camera. Appendix C contains circuit specifications for these devices.

5. Image Capture and Processing

To best use the 8-bit video resolution available, image integration times were adjusted so intensities in the integrated images were three decimal significant digits (100-255 greyscale value). This allowed greater pressure resolution in the ratioed image, as arithmetic operations in the EPIX 4MIP image processing software used the computer 32 bit accuracy. It was determined experimentally that 20.0 seconds was a necessary integration period for the gate speeds required. Image blooming during this integration period was not observed as reported by Varner (1995) or suggested by Xybion (1992). “Wind-on”, “wind-off”, dark-current, and calibration image captures were scripted with the available scripting macro in the 4MIP software (Epix Incorporated, 1993). This allowed image capture to be initiated at the personal computer interface and provided ‘hands-off’ image capture. The user was then freed to initiate image triggering and to monitor the system. Because two video fields were measured by the camera, the default field value of 0 in the TRIGGERED IMAGE CAPTURE menu was set to 2. Images were saved using a file naming construct given in Table 6. The scripted programs for image capturing and post-processing are listed in Appendix D.

1st digit	2nd digit	3rd, 4th, 5th digit	6th, 7th digit	suffix
X - experimental C - calibration	N - “wind-on” F - “wind-off” D - dark current	### - frequency (Hz)	Test #	.TIF

Table 6. File Naming Structure

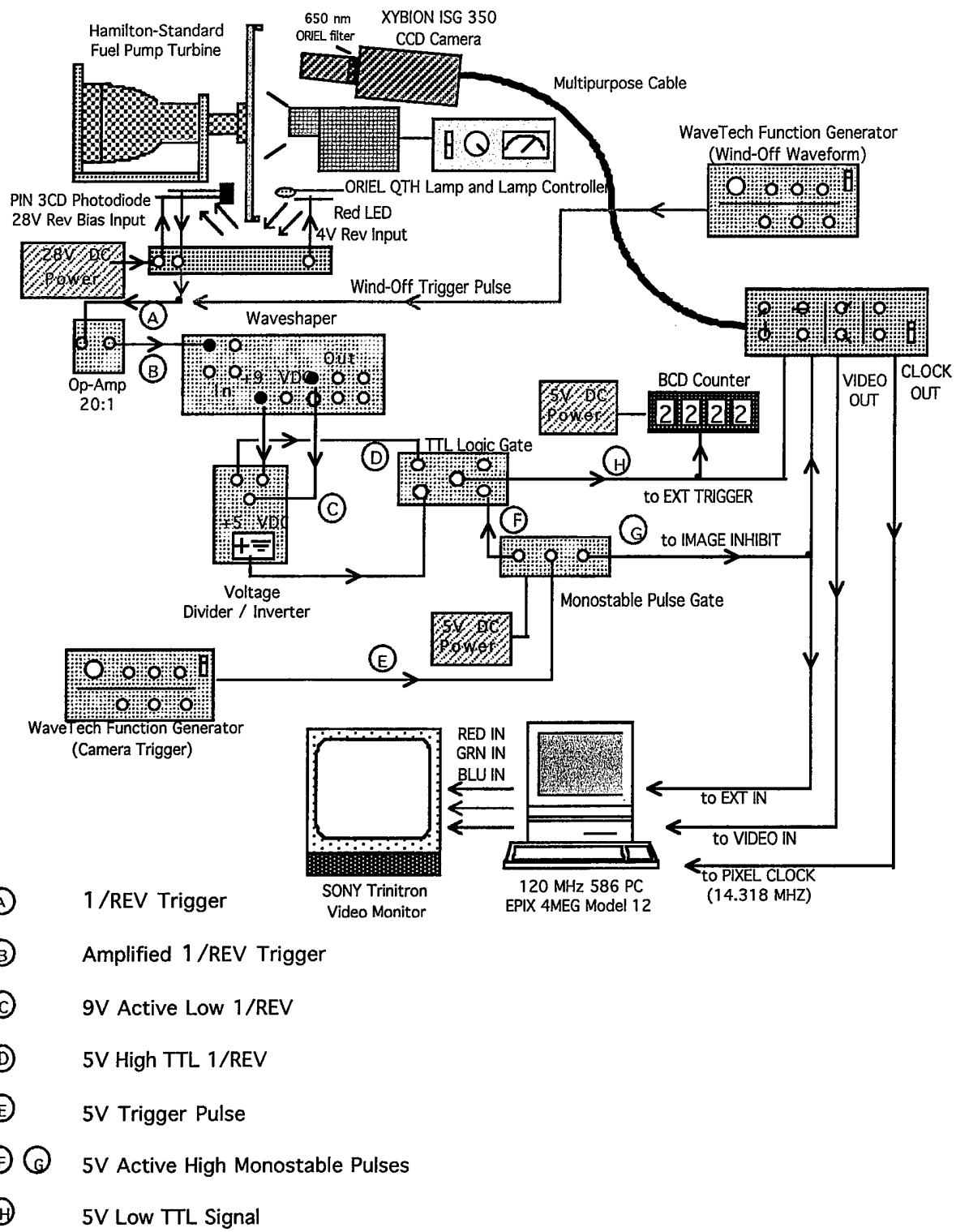
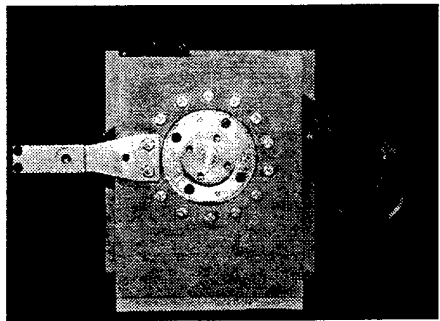
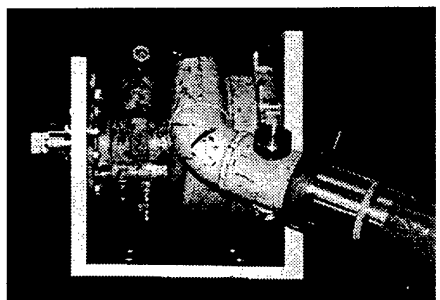


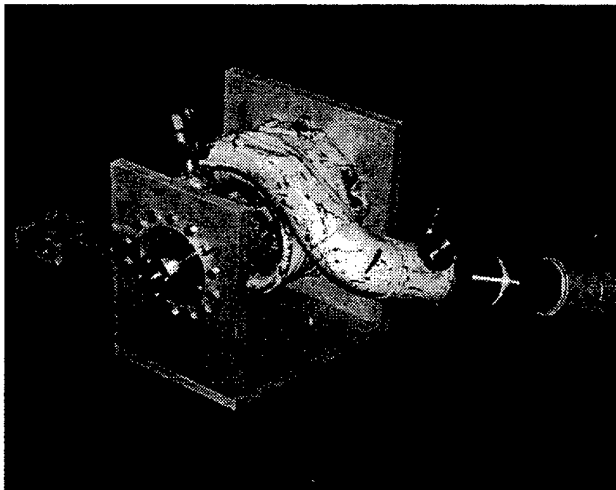
Figure 7. PSP Experimental Setup



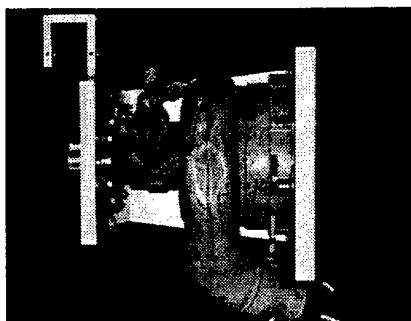
Turbine / Cradle Front View



Turbine / Cradle Left Side View



Turbine / Cradle Oblique View



Turbine / Cradle Top View

Figure 8. Four-View Aspect of Hamilton-Standard TPC13 Turbine Mount

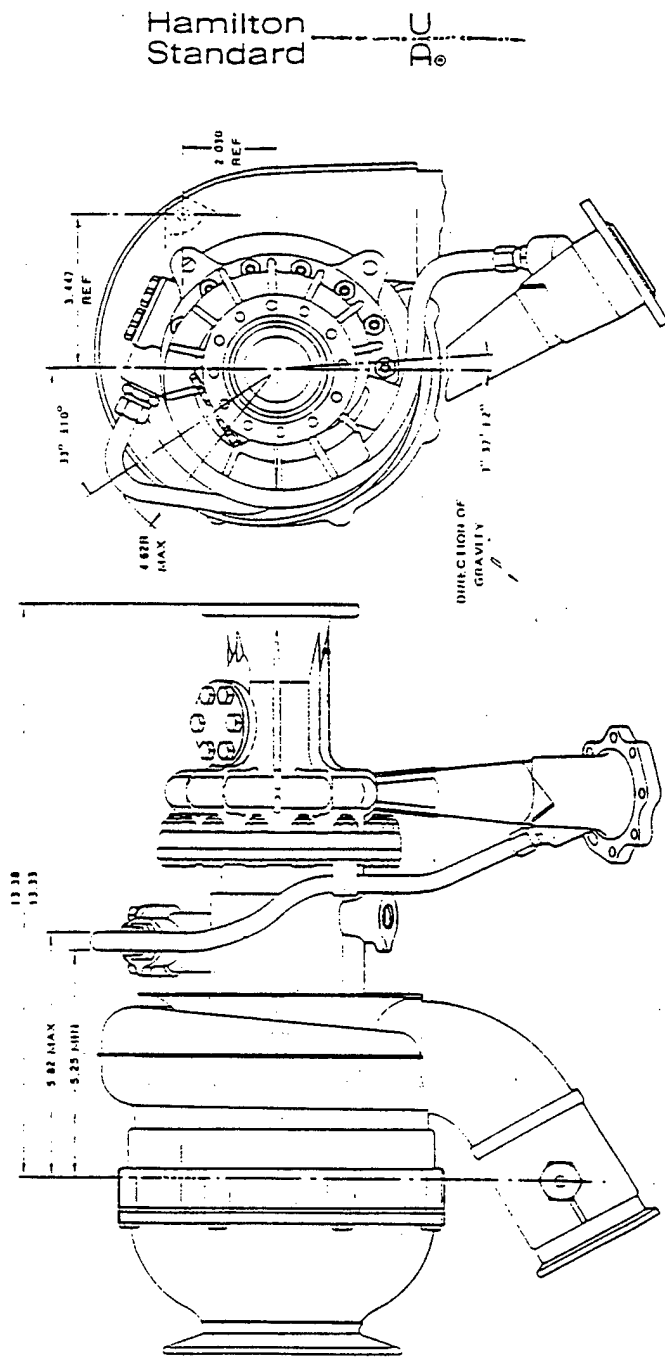


Figure 9. Hamilton Standard TPC13 Turbine Dimensional Illustration

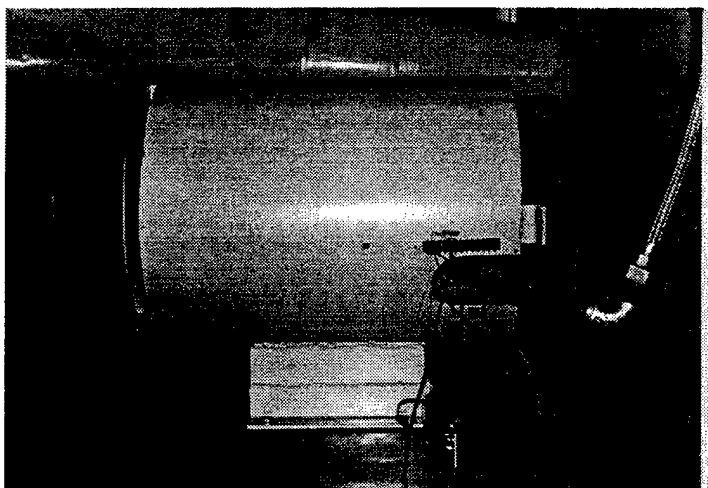


Figure 10a. Spin Chamber Side-View with Protective Front Plate Installed
(Air Supply Plumbing and 1/REV Trigger Circuit Wiring shown)

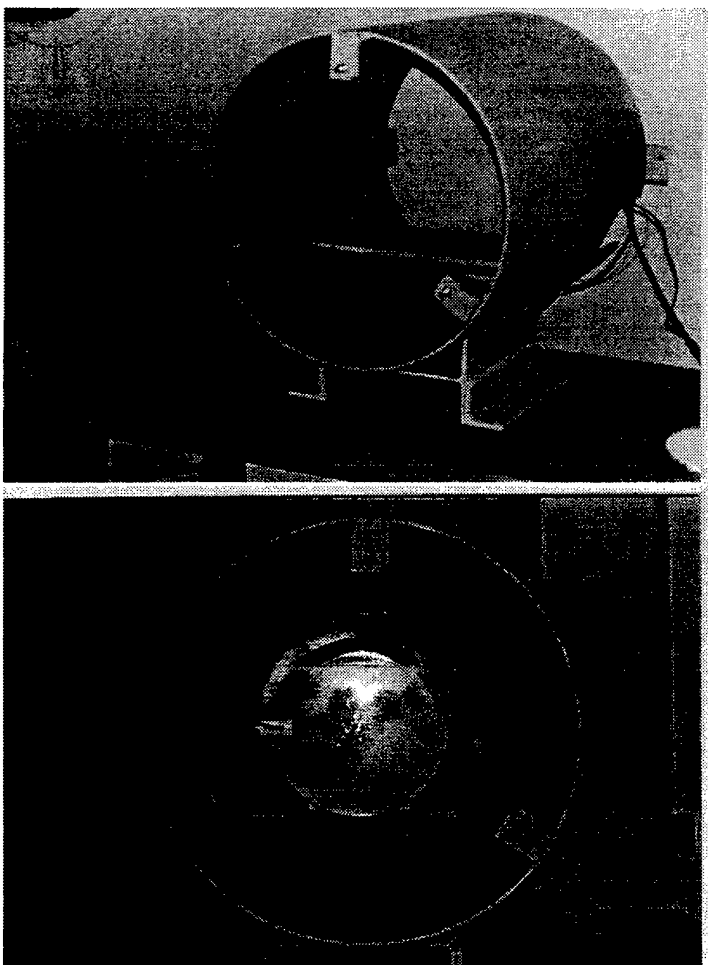


Figure 10b. Spin Chamber Views;
Turbine Uninstalled (Top) and Installed (Bottom)

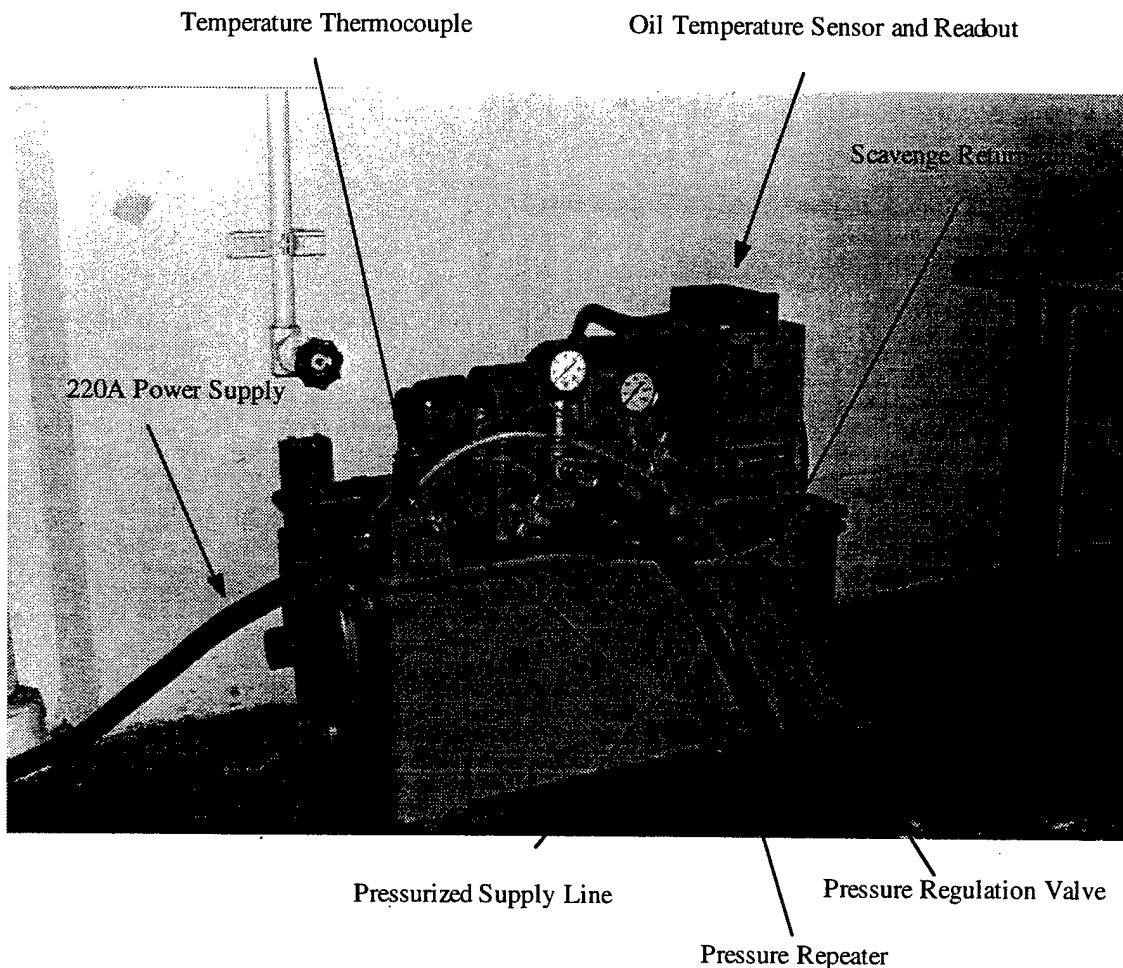
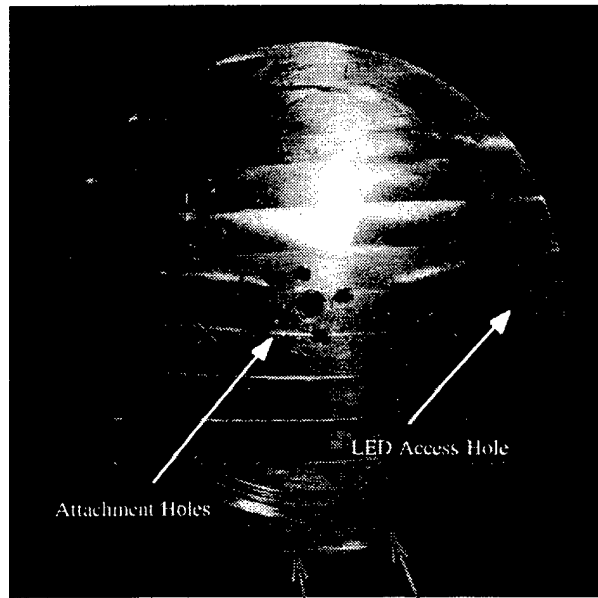
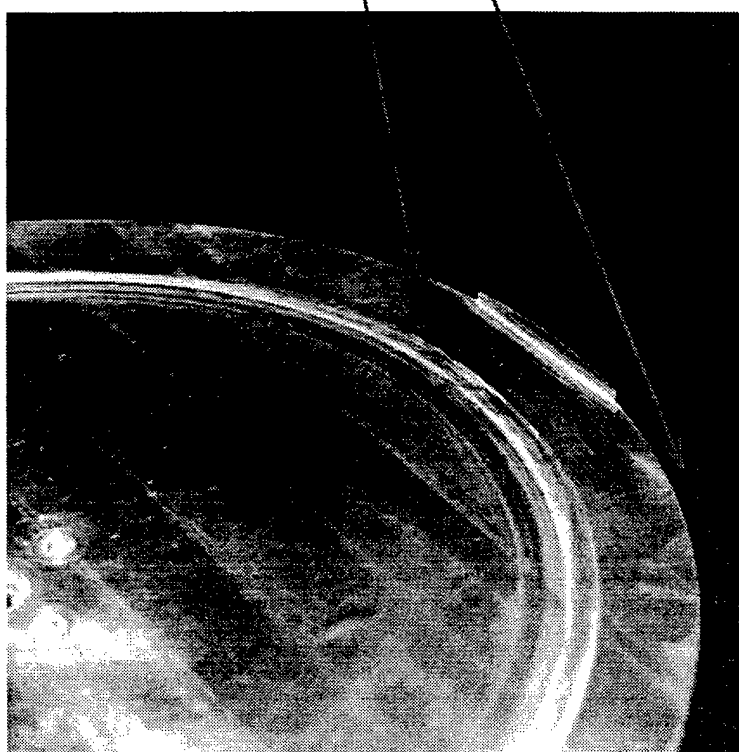


Figure 11. Turbine Lubrication System

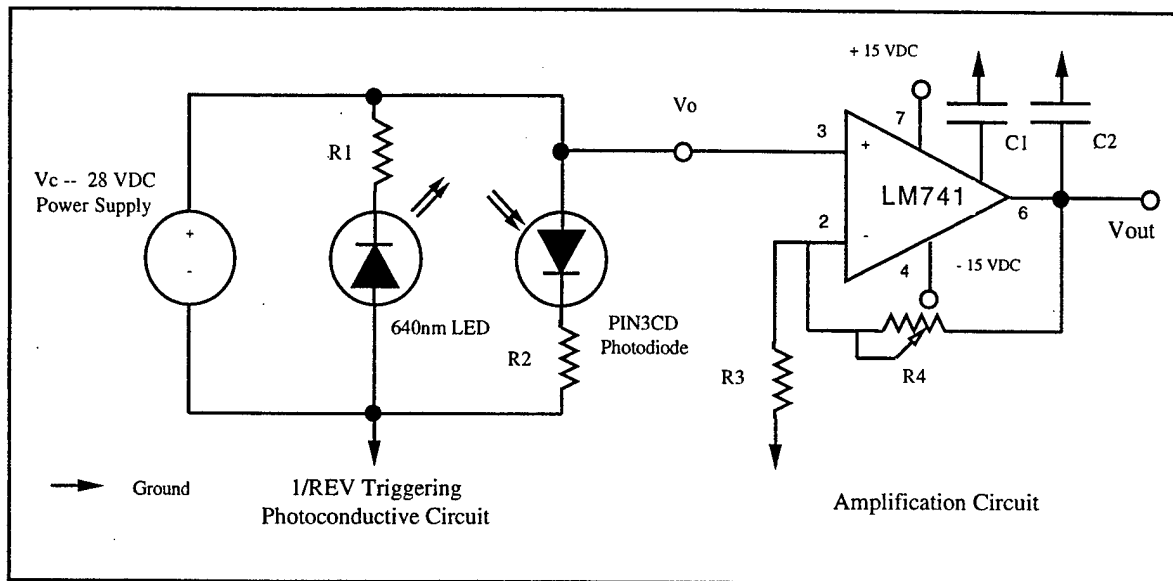


Dual-Bladed Disk-Rotor



Disk-Rotor Blade Expanded View

Figure 12. Dual-Bladed Disk-Rotor



Vc	28 VDC	R1	2.2 kΩ
Vo	300 mV	R2	10 kΩ
C1	0.1 μF	R3	10 kΩ
C2	0.1 μF	R4	0-200 kΩ

Figure 13. Triggering Circuit Diagram

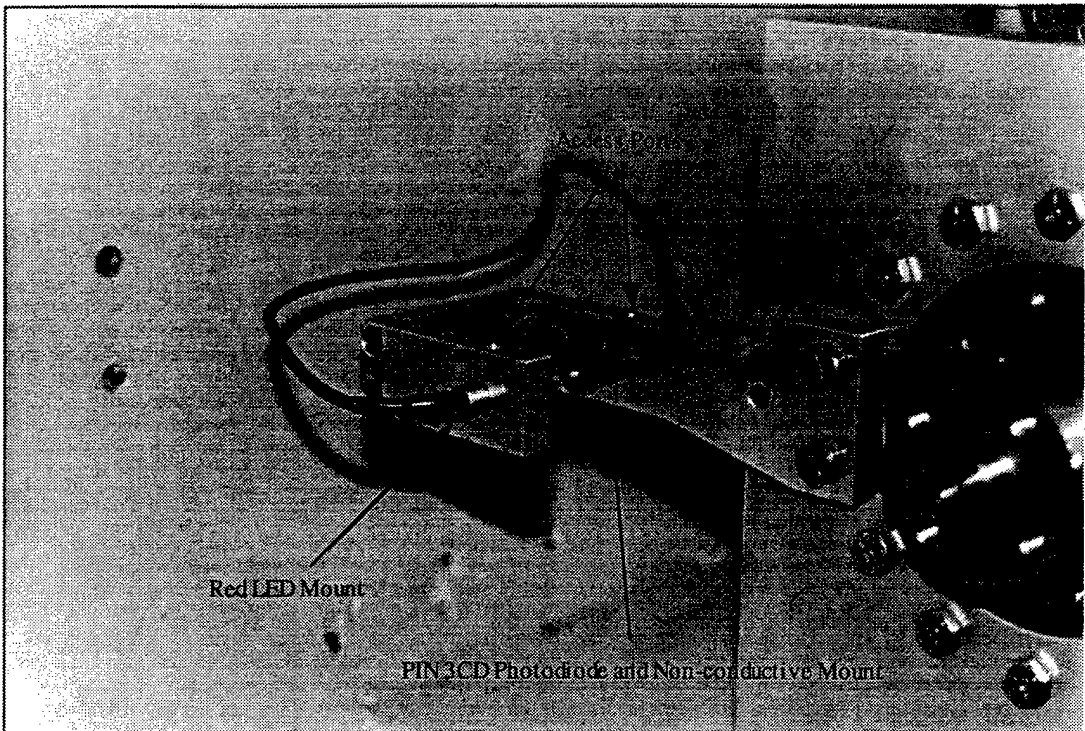


Figure 14. LED / Photodiode Pair and Mounting Bracket

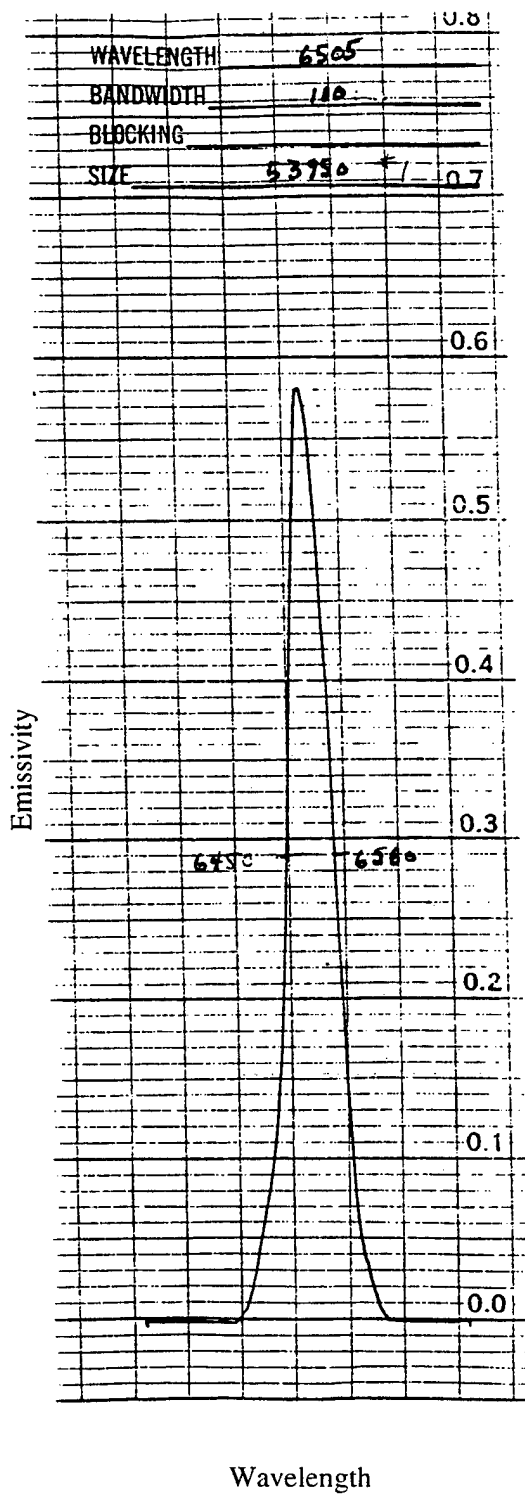


Figure 15. ORIEL Camera Filter #53590 Characteristics
28

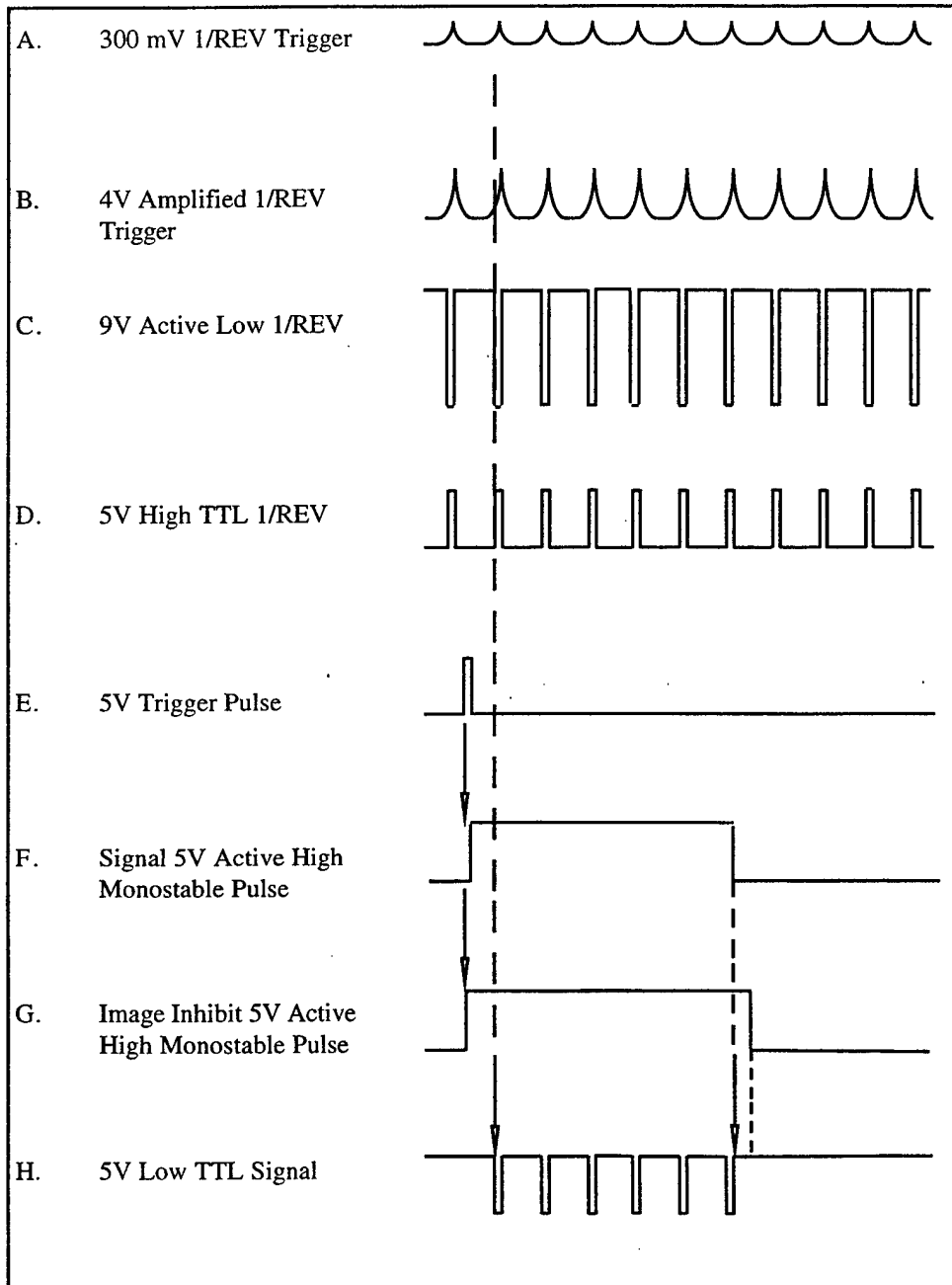


Figure 16. Waveform Shaping Schematic

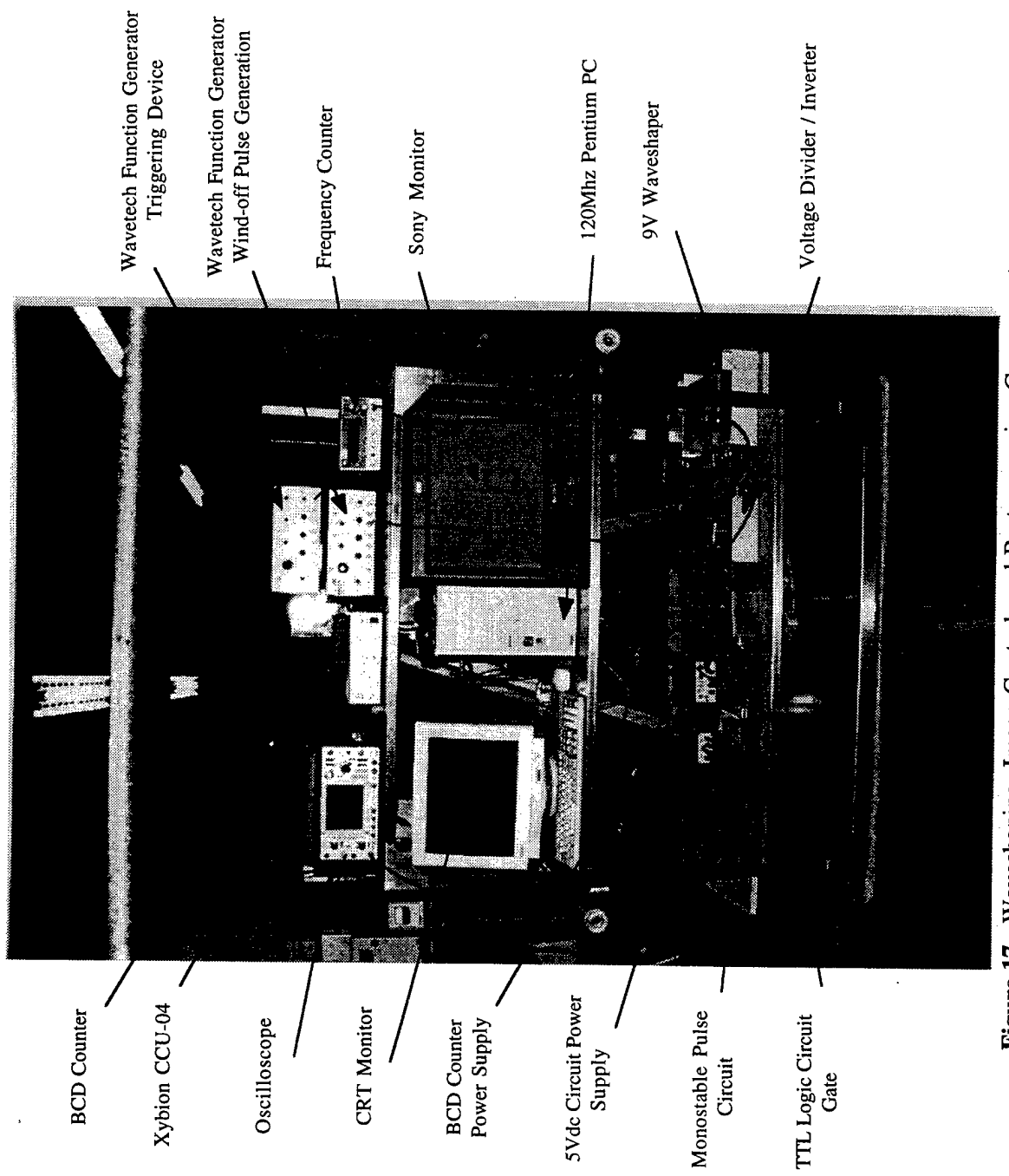


Figure 17. Waveshaping, Image Control, and Postprocessing Components

IV. EXPERIMENTAL PROCEDURE

A. ROTOR PREPARATION

The disk-rotor was prepared in the manner described by Varner (1995). Seivwright describes in detail the paint application process (Seivwright, 1996). In summary, a white, glossy Krylon (#1501) undercoating was applied and allowed to dry completely. The pressure-sensitive paint, PtEOP probe molecules immersed in a GP-197 silicon matrix binder, was applied with an airbrush over the blade area. A vertical reference mark was made at the center of the blade with a fine razor for alignment of "wind-on" and "wind-off" images. The spatial resolution of this reference mark was generally 2-3 horizontal pixels when imaged. The disk was attached at the four attachment points with steel bolts, with the balance shims (Table 2) inserted about the bolts between the turbine attachment disk and the rotor disk. The attachment fasteners were torqued to 30 in-lbs with a torque wrench, ensuring a consistent plane of rotation. The machine indicator, discussed in the disk balance section, was used to verify that the rotor disk rim runout remained within 0.005 in. Figure 10b shows the installed painted disk. The spin-chamber face plate was then secured and the lamp and camera set in place. When viewed, the blade, at the twelve o'clock position, was in the upper 100 vertical pixels of the display.

B. CAMERA AND LAMP PLACEMENT

Upon setting the lamp and camera in place, a spirit level and inclinometer were used to verify the camera and light source axes were normal to the disk-rotor plane to within $\pm 1.0^\circ$. The camera was required to view the blade at a $4.5^\circ \pm 0.1^\circ$ inclination from the horizontal at a distance of 17.5 ± 0.1 inches due to the spin chamber face plate configuration. The lamp lens assembly was placed 15.2 ± 0.1 inches from the disk center. The lamp intensity was set to a maximum with the variable intensity adjustment and was turned off between tests using the power switch on the lamp controller, to ensure the same intensity was produced for both "wind-on" and "wind-off" images.

C. FOCUS AND GATING

With the camera and lamp positions verified, the blade edge was focused manually with the camera lens focus adjustment. This process was accomplished with the lamp illuminating the painted surface in laboratory darkness. The total paint illumination time was monitored due to the photo-degradation characteristics of the paint. Using the PIXEL PEEK

/ POKE feature in the 4MIP software, the blade was measured in horizontal pixels and its 2.18 inch physical length was related as a percentage of overall horizontal video resolution. The correct gate speed from Table 5 was then selected and set using a separate Wavetek function generator to provide a simulated trigger (see Figure 7).

D. "WIND-ON" ACQUISITION

The first measured image was the "wind-on" acquisition. With the camera and circuit settings ready, the lubrication system for the turbine was started and air was introduced slowly to the turbine to initiate a steady turbine run-up. Oil temperature, atmospheric pressure and laboratory temperature were recorded during run-up. Once test operating frequency was achieved, the lock nut for the butterfly valve on the air control console was secured and frequencies were maintained to within ± 1 Hz. The lamp was turned on, allowed to ramp to its set intensity, and the disk was illuminated for at least ten seconds prior to imaging to allow the paint time to respond. "Wind-on" script initiation presented the 4MIP triggered-image capture menu and the image was triggered with a single function generator pulse. Following the 20.0 second image integration period, the count from the BCD counter was recorded manually while the script cycled to the next available buffer and prompted another image capture. This process was repeated for the eleven available image buffers, which were subsequently averaged with the 4MIP IMAGE PROCESSING - IMAGE SEQUENCE OPERATIONS menu. The resulting image was saved in a .TIFF picture format in the hard drive memory of the PC under directory C:/4MIP/IMAGES/. The turbine was then shut down and the recorded trigger count was totalled.

E. DARK CURRENT ACQUISITION

Dark current was recorded in laboratory darkness with the camera lens cap off, accounting for the influence of the LED. A second Wavetek generator was used to produce a pulse trigger similar to that produced by the 1/REV circuit and then input into the operational amplifier. The remainder of the circuitry settings remained identical to the "wind-on" settings. The same procedure was then followed, with image counts recorded over the eleven image buffers. The averaged image was saved as above. Because dark current builds as circuitry components become warmer, dark current imaging was conducted between "wind-on" and "wind-off" to approximate an averaged 'warm' condition of respective system components.

F. "WIND-OFF" ACQUISITION

The "wind-off" imaging process followed the identical format of the dark current imaging. However, the image was registered to the "wind-on" image and the lamp was switched on. This was accomplished by loading the "wind-on" image into buffer 1 and marking the vertical reference mark with the cross hairs from within the PIXEL PEEK / POKE menu. The CCU gating knob was set to AUTO without adjusting the vernier gate timing knob, allowing for a return to the exact gate setting used in the previous imaging processes. The lamp was turned on and the image displayed in real time due to the AUTO setting feature. The disk was manually moved until the vertical reference was located at the marked location of the "wind-on" image. The gate selection was reset to its manual gate position. Script initiation, image capture, buffer averaging, and file saving were accomplished as described above.

G. POSTPROCESSING

Scripting of the post processing sequence loaded "wind-off", "wind-on", and dark current images respectively into the first three buffers. The dark current was subtracted with the 4MIP IMAGE PROCESSING / TWO IMAGE ARITHMETIC menu using the MOD 256 subtraction option (Epix Incorporated, 1993, p.28-1). With the dark current subtracted, the images were ratioed, "wind-off" to "wind-on", in the same menu under RATIO IMAGES. A ratio coefficient, C0, was selected which appropriately shifted the ratioed images to an optimum resolution. Linear pseudocoloring of the image provided visual enhancement of the intensity distribution. The RGB lookup function is presented in Figure 18. This process is discussed in detail by Seivwright (1996). Pressure ratios were then estimated through application of the Stern-Volmer relationship to the ratioed intensities.

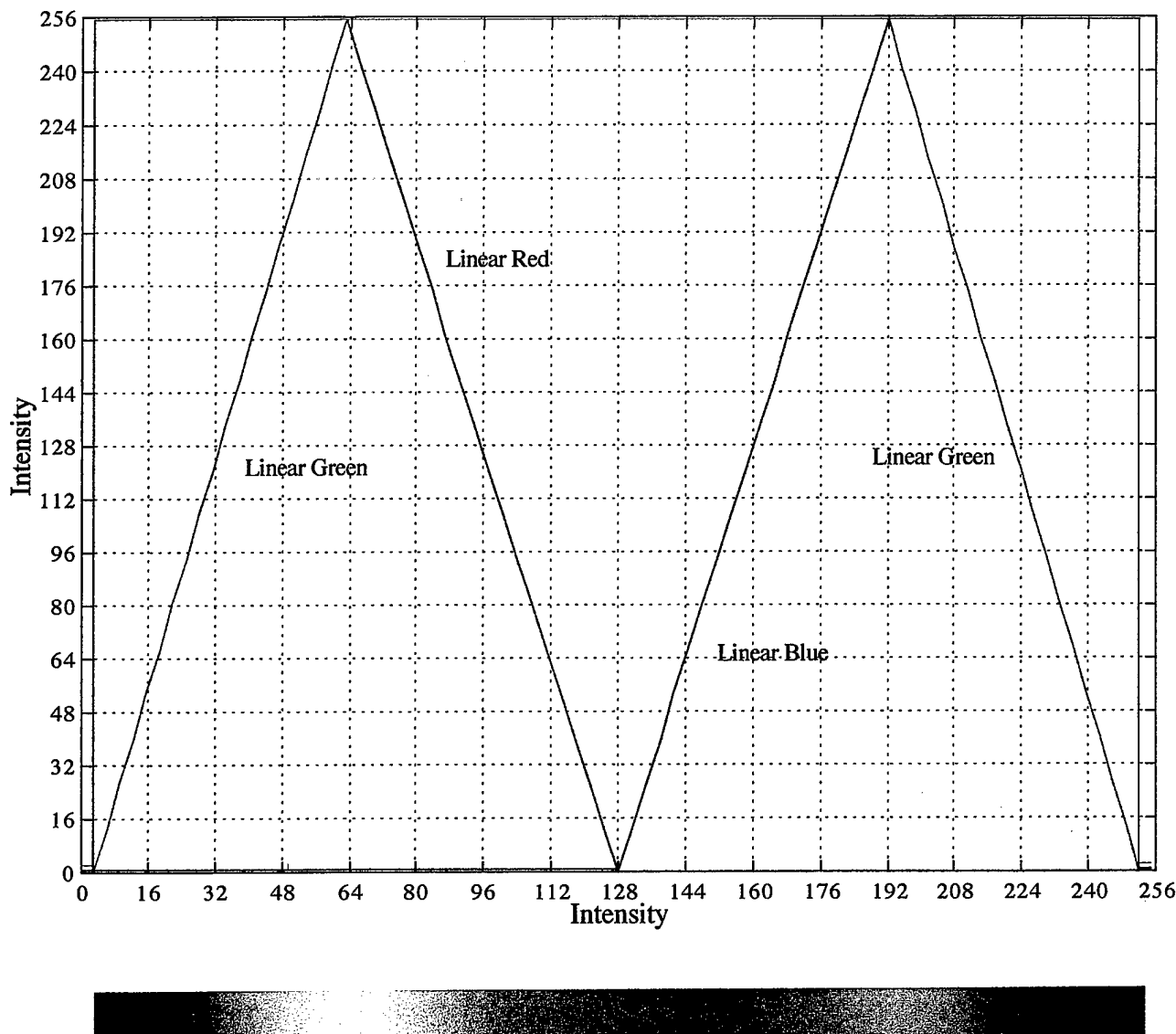


Figure 18. Plot of Linear RGB Pseudocoloring Functions and Color Palette

V. RESULTS AND DISCUSSION

Ratioed images were acquired for four rotor frequencies; 166 Hz, 266 Hz, 285 Hz, and 333 Hz. The Io/I ratios were multiplied by a factor of 50, providing a common reference and allowing continuous greyscale resolution. The technique developed for this application resulted in Table 7, which summarizes each case and its image gating, integration timing, and average image counts. The variation in the integration periods resulted in less than 0.63% difference between "wind-off", "wind-on", and dark-current on-times. The colorized images are shown in Figures 19-22. Image quality was affected by image integration times during which noise was introduced proportionally and resulted in a 'blotchy' effect in the images. This effect was able to be reduced by increasing the number of images used in the averaging. However, the number of averaged images was limited due to the photodegradation effect of the paint. For each case, the total PSP excitation time was approximately fifteen minutes, keeping the response of the PSP to within 90% of its initial value (Kavandi, 1990).

Figure 19, the 166 Hz case, shows a nearly constant intensity distribution at a ratio of approximately 1.2. Proper "wind-off" / "wind-on" registration was verified by the lack of blade spatial detail and constant intensity. Figure 20, the 266 Hz case, shows similar traits but with the intensity ratio increasing from 1.75 to 2.25 radially. A vertical reference mark made on the blade can be identified at the central, upper disk rim in a low intensity. This case image was also characterized by PSP shedding in the area below the blade trailing edge. This effect resulted from horizontal and vertical reference marks in the paint, made using a scalpel, along which PSP was shed progressively during the "wind-on" acquisition. Because the referencing caused PSP shedding, the referencing was not used at higher speeds. The 285 Hz case, Figure 21, shows a similar intensity distribution radially, but with slightly increased intensity ratios, from 1.9 to 2.4. Figure 22, imaged at 333 Hz, showed the results of the increased wheel speed. A dramatic intensity change in the radial direction was apparent, with high intensities shown under the blade edge. Ratios from 2.6 to 4.3 were present in this image. Also characterizing this image was PSP shedding at approximately 20% blade chord. No reference marking had been done in this region.

Using the Stern-Volmer relation to relate the intensity maps of Figures 19-22 to surface pressure does not give physically meaningful results since pressure ratios ranging from 1.2 to 6.0 would be calculated for the four cases based on previous calibrations of the PSP used (Varner, 1995). The intensity distributions are, however, qualitative. Figure 22, with a rim Mach number of 0.865 shows increased intensity under the blade edge, indicative of the stagnation effect on the radially pumped fluid mass. Because PSP was shed in the

Case	1	2	3	4
f {Hz}	166	266	285	333
N {rpm}	10,000	16,000	17,000	20,000
U {fps}	521.5	835.7	895.4	1046.2
Mach No	.442	.709	.794	.865
Blade Spatial Resolution (C)	.675	.701	.773	.718
Integration Period (T) {sec}	19.87	19.75	20.16	20.13
Gate Speed (G) {μsec}	0.65	0.40	0.33	0.30
No Images in Average	11	11	11	11
Avg Wind-Off Images in Integration	3298	5247	5738	6725
Avg Wind-On Images in Integration	3302	5232	5739	6682
Avg Dark Current Images in Integration	3292	5259	5748	6711
Avg Wind-Off On-Time / Image {μsec}	2144	2099	1894	2017
Avg Wind-On On-Time / Image {μsec}	2146	2093	1894	2004
Avg Dark Current On-Time / Image {μsec}	2139	2104	1897	2014
P _{atm} {in Hg}	29.94	29.95	30.03	30.03
T _{atm} °R	529	529	529	530

Table 7. Imaging Data Comparison by Case

vicinity where a shock might begin to develop in a transonic flow, the edge at which the paint was shed may represent a shock structure. However, the pressure sensitivity of the probe molecule was a lesser contributor to the intensity distributions than the temperature sensitivity. An approximate physical verification of increased plate temperature was made following each test by placing a contact thermocouple against the disk after the turbine stopped windmilling. The increased disk temperatures measured were consistent with the numerical stagnation temperature solutions in Figures 3-6.

To examine the intensity change radially, Figures 23a-b graphically compare the intensities along two vertical lines of pixels, in the radial direction at 15% and 50% chordwise locations. Figure 23c provides a comparison along a horizontal line of pixels, the chordwise direction at 83% radial location. Figures 23a-b show the effect of radially increasing velocity on the local stagnation temperature, which was verified in the numerical stagnation temperature predictions. The increase in slope between each case confirms the dependence on both temperature and pressure, as greater effects are found at higher wheel speeds. Figure 23c verifies the uniformity of pressures and temperatures at nearly constant radius.

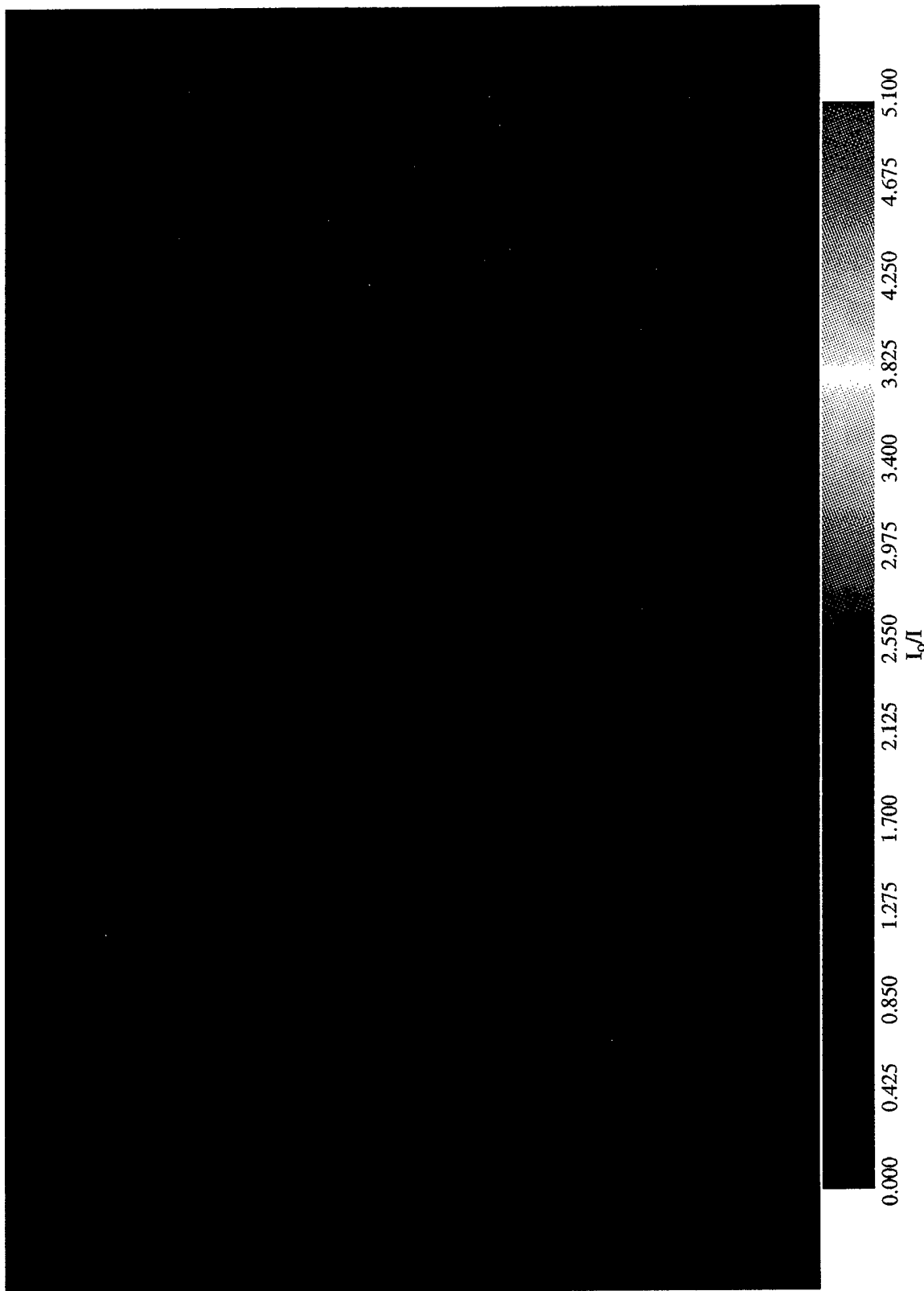


Figure 19. Ratioed Intensity Image at 166 Hz Disk Frequency

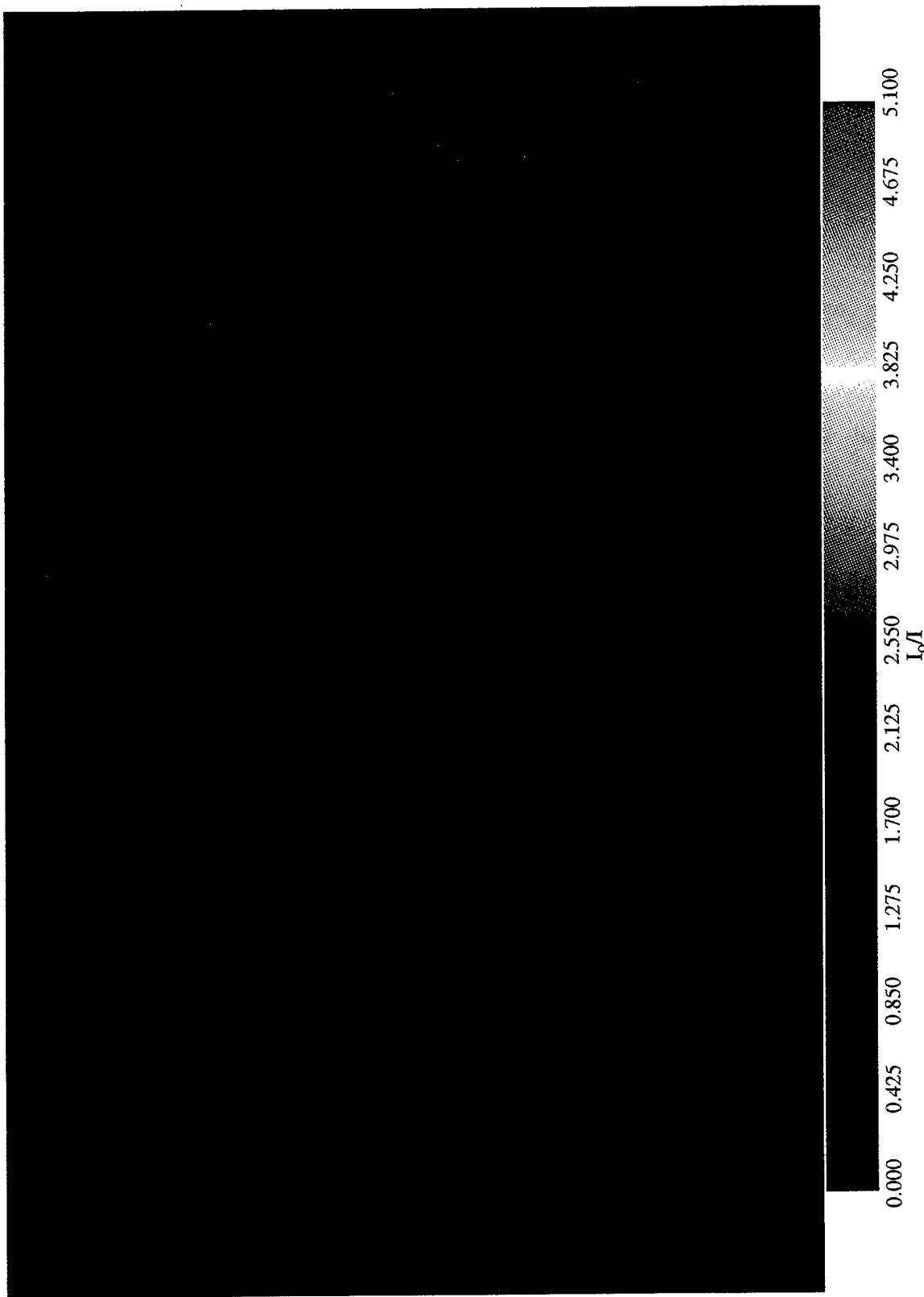


Figure 20. Ratioed Intensity Image at 266 Hz Disk Frequency

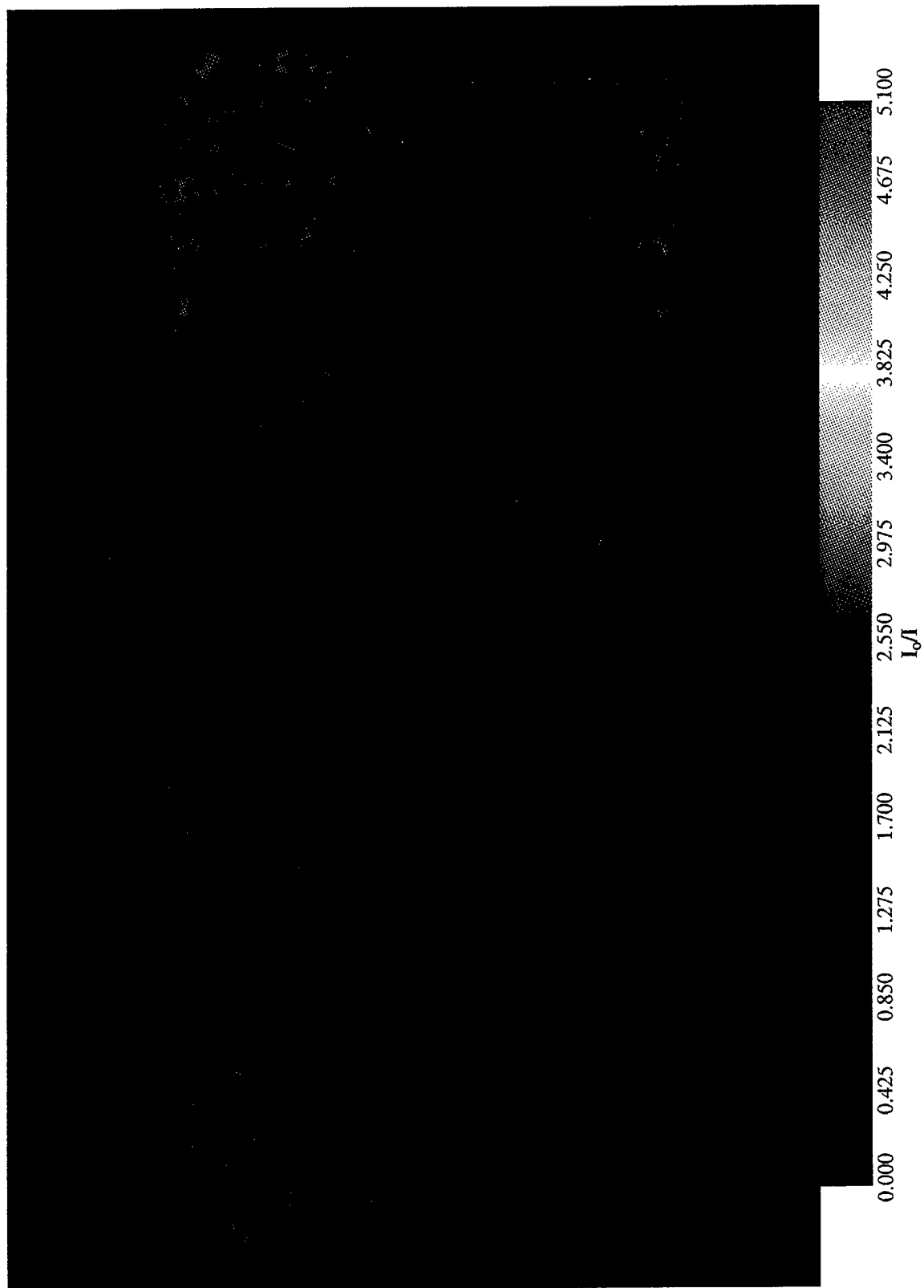


Figure 21. Ratioed Intensity Image at 285 Hz Disk Frequency

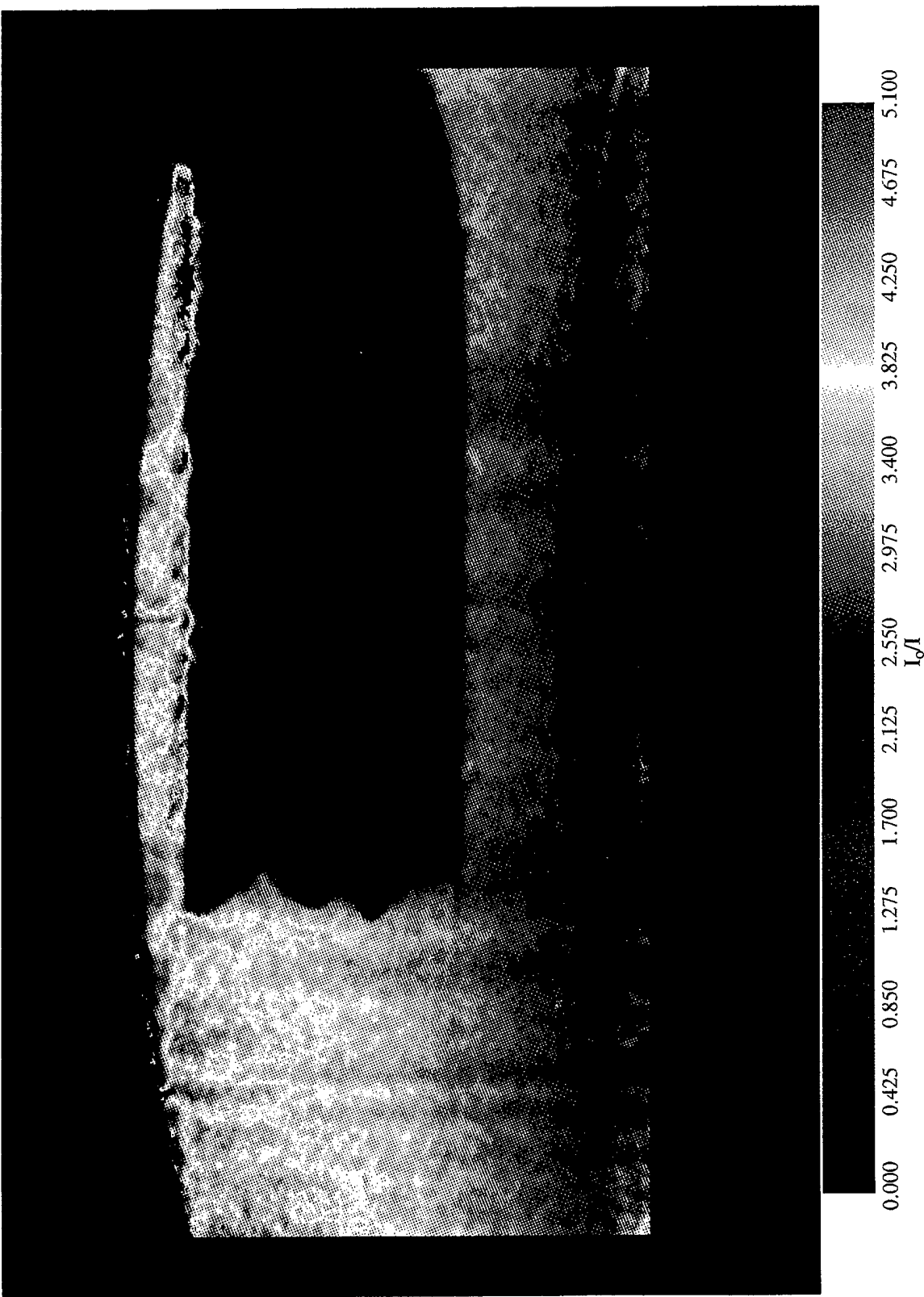


Figure 22. Ratioed Intensity Image at 333 Hz Disk Frequency

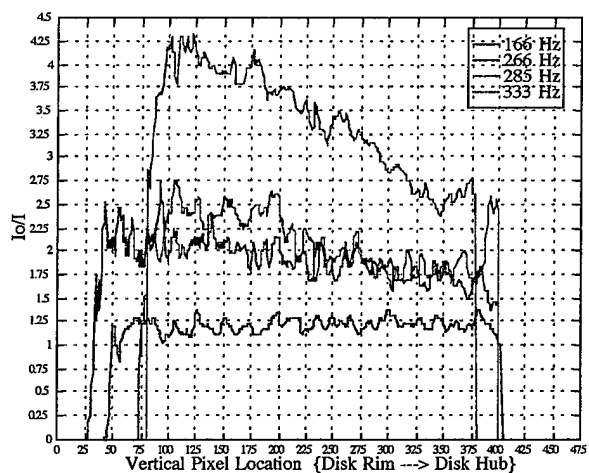


Figure 23a. Vertical I_0/I Distribution at Horizontal Station $X = 15\%$ Blade Chord

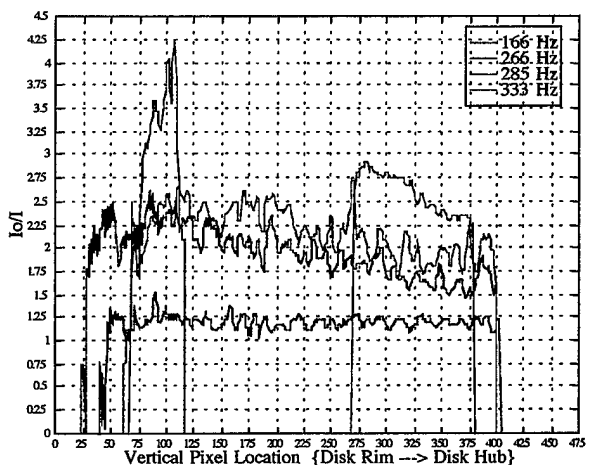


Figure 23b. Vertical I_0/I Distribution at Horizontal Station $X = 50\%$ Blade Chord

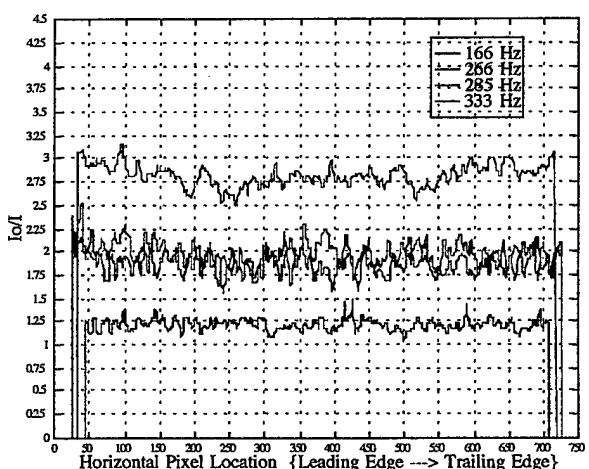


Figure 23c. Horizontal I_0/I Distribution at Vertical Station $Y = 83\%$ Disk Radius

VI. CONCLUSIONS AND RECOMMENDATIONS

The potential use of pressure sensitive paint as a pressure mapping technique in transonic turbomachinery design validation has been furthered by the successful development and application of a phase-locked imaging technique, providing optimum resolution and eliminating pixel blur. Incorporation of a BCD counter allowed verification of equivalent 'on-times' between respective images while trigger signal amplification allowed reliable circuit triggering throughout the frequency range tested. Development of the amplifier and waveshaping circuit given in Appendix C would enhance the overall reliability of the phase-locked circuit, eliminate incompatible circuit components, and improve system response.

The turbine installation and successful operation to 20,000 RPM provided a working test-bed for further PSP development in the transonic range. The 1/rev detection and associated circuitry proved suitable for the application. Bearing lubrication, however, was not adequate for continuous operation at higher wheel speeds because the lubricant was not scavenged from the bearing case, creating high bearing temperatures. Suction pressure on the return line will alleviate this problem. To allow higher wheel speeds and the generation of a greater pressure differential on the disk, a redesign of the disk for constant stress at a design condition of 30,000 RPM was carried out and is presented in Appendix E. Machining of the redesigned disk-rotor was initiated at the conclusion of the present study.

The relationship of the intensity change to radially changing stagnation temperature has been shown, providing the understanding needed to obtain fully quantitative results. Because "wind-on" imaging took place under a radial temperature change and "wind-off" imaging took place subsequent to turbine shut down, the exact effect of temperature can not be deduced. To effectively quantify the effect of temperature on the PSP, the effect of oxygen quenching due to pressure would have to be eliminated and only the effect of temperature measured. Therefore, using two "wind-on" images, one with the effect of pressure and one with the effect of pressure and temperature, the images could in principle be reduced using calibration data.

To obtain quantitative measurements in the NPS Turbopropulsion Laboratory transonic compressor test-rig, further technique development first must occur on the test bed developed in the present study. In addition, practical PSP application techniques for the transonic rotor must be considered. Recommendations include:

1. Apply suction pressure to the turbine lubrication return to reduce bearing temperatures.
2. Align and balance the new disk-rotor and operate to 30,000 RPM.

3. Redesign the waveshaper to ensure optimum circuit response at higher wheel speeds.
4. Identify an oxygen impermeable binder in which PtEOP may be suspended thereby yielding a temperature sensitive paint. Alternatively examine the potential of sealing the current PSP from oxygen, eliminating the quenching created by collisions with oxygen. Consideration in this regard must be made to the effect of a sealant on image distortion.
5. Re-derive the quantum equations including temperature as a variable to appropriately determine how to register temperature sensitive and pressure sensitive images for quantification.
6. Identify the effect of blade curvature and angled camera placement on intensity distributions.
7. Determine the adherence qualities of the PSP at higher wheel speeds, with and without a Krylon undercoating.
8. Quantify the effect of the white Krylon undercoating as an image enhancer and determine its necessity in application to the transonic rotor, where paint thickness and weight present additional balance and flowfield distortion considerations.
9. Develop a registration technique for "wind-off" / "wind-on" images of the transonic compressor test rotor accounting for the mechanical deformation of the "wind-on" condition.
10. Identify image postprocessing filtering requirements to aid in reducing signal noise resulting from image integration.

APPENDIX A.

OVERFLOW NUMERICAL SOLUTION

A. CODE INPUT

The numerical solutions obtained for the rotating flat-plate disk were solved on the computational domain previously described, shown in Figure 1. Table A1 describes the relation of coordinate systems in defining the geometry. The output of GRIDGEN, the geometry generating code, was a standard PLOT3D format. Buning (1995) provides PLOT3D grid format detail. The grid was converted to an unformatted binary file for use by the OVERFLOW solver. The input grid was defined as boundary conditions through the OVERFLOW input file, 'overflow.in'. Table A2 details boundary condition definition for the Euler and viscous cases. To verify the grid compatibility, boundary condition applicability, and test the solution independence, an Euler solution was conducted by defining a low input Mach number (to $M=0.21$) at the input plane and defining the exit plane as an adiabatic wall. This solution displayed the predicted symmetric, radial flow at the wall with a converged solution indicated in the L2-norm and density residuals. A similar stationary, viscous solution was computed.

Domain	Physical	GRIDGEN	OVERFLOW	Computational
Coordinates	θ, R, Z	I, J, K	J, K, L	ξ, ζ, ψ

Table A1. Grid Domain and Coordinate Relation

Boundary Condition Description	Type	Direction Assigned
Periodic	10	+1; all J=1, all K, all L
Axis (K around)	15	+2; all J, K=1, all L
Characteristic condition	47	-2; all J, K=K _{max} , all L
Supersonic/Subsonic inflow/outflow	32	+3; all J, all K, L=1
Inviscid, adiabatic wall (pressure extrapolation)	1	-3; all J, K ^{1, 2} , L=L _{max}
Viscous, adiabatic wall (pressure extrapolation)	5	-3; all J, K=1 to K _{edge} ³ , L=L _{max}

¹Euler solns -- all K
²Viscous solns -- K=K_{edge} to K_{max}
³Viscous solns only

Table A2. OVERFLOW Boundary Conditions

Initial solutions were obtained on the Naval Postgraduate School CRAY processor through batch submission. Due to administrative waits for processor access and the relatively small grid size used in the solution, the OVERFLOW code was compiled on a Department of Aeronautics and Astronautics Silicon Graphics (SGI) workstation. The application represented the first successful compilation of the code on an NPS workstation. Use was made of ‘makefile.sgi_mips2’ in compiling the code. The ‘Makefile’ compiler allowed individual code modification for deriving the solution for the rotating disk at varying speeds.

B. SOLUTION METHOD

To obtain the solution for a rotating planar disk, the OVERFLOW program code was adapted in the boundary condition subroutine. Table A3 gives the path and subroutine calls which were modified, in descending hierarchy.

.../over1.6aw/ns/bc.F
.../over1.6aw/ns/bc/bcvwp.x.F
.../over1.6aw/ns/bc/bcnosl.F

Table A3. Modified OVERFLOW Subroutines

The rotation of the disk was produced by imparting a radially varying velocity distribution in ‘v’ and ‘w’ at each grid point which defined the viscous disk. In producing this no-slip rotating frame, the actual code modification required was minimal. The primary modification was made in bcnosl.F. First the physical grid coordinates were entered as arguments in the respective subroutine call. The coordinates were required to apply the appropriate radial location for tangential velocity computation from the rate of rotation. Second, the internal call to subroutine uvwrho.F, which provided time metrics for the contravariant velocities, was commented out. Next, the appropriate velocity distribution was computed and subsequently multiplied by the density. Because updates to the density (q_1) occurred prior to the velocity extrapolation at the next time step, correct updates were made to the solution vector Q, shown by Equation A1.

$$[q_1 \ q_2 \ q_3 \ q_4 \ q_5] = [\rho \ \rho u \ \rho v \ \rho w \ e] \quad (\text{A1})$$

To obtain the appropriate velocity distribution at the disk surface, the internal call to bczero.F was retained to impart a zero ‘u’ (axial) velocity. The ‘v’ and ‘w’ velocities were then computed from the tangential velocity, V_θ , in non-dimensional form. Additional inputs to the solution file included the implicit time step, ‘dT’, a minimum Courant-Freidrichs-Levy

(CFL) number, and turbulence parameters. Buning (1995) provides recommendations for these solution variables. The parameters listed in the ‘overflow.in’ file provided remained constant for all solution cases.

The calculation of the non-dimensionalized ‘v’ and ‘w’ velocity components at the disk boundary follows in Equations A2-A3. Non-dimensional quantities are shown with asterisks. Taking wheel speed in RPM (Ω), the angular rotational rate was given by

$$\omega = \frac{\Omega\pi}{30} \quad (\text{A2}).$$

The angular frequency was non-dimensionalized by the freestream speed of sound, a_∞ , and the length scale of the grid; one disk radius, R.

$$\omega^* = \frac{\omega R}{a_\infty} \quad (\text{A3}).$$

The velocity components in the standard Cartesian sense were transformed from the non-dimensional tangential velocity, V_θ^* , which was obtained from multiplication of the angular frequency, ω^* , by the radial location, \bar{r} . The axisymmetric-to-Cartesian transformation was made by incrementing the angle by quantity $d\theta$ and resolving the v^* and w^* components based on the angular, or ‘J’, position. The ‘ JKL_{\max} ’ subscripts generalize the location on the disk for which the computation was solved. Equations A4-A7 show the velocity computation.

$$V_\theta^* = \omega^* \bar{r} \quad (\text{A4}).$$

$$d\theta = \frac{2\pi}{J_{\max} - 1} \quad (\text{A5}).$$

$$v^*_{JKL_{\max}} = V_\theta^* \sin(J * d\theta) \quad (\text{A6}).$$

$$w^*_{JKL_{\max}} = V_\theta^* \cos(J * d\theta) \quad (\text{A7}).$$

C. SOLUTION OUTPUT

The solutions represented in Figures 3 through 6 were graphically portrayed using the computational fluid dynamics solution modeler FAST . The solution set was output in unformatted binary construct in a file ‘q.save’. This file was read into FAST for graphical display. Additional output files included the residual data in ‘resid.out’. This file, in text format, was used to observe the convergence history of the solution sets. Figure A1 shows the L2-norm and density residual history for the 333 Hz case. This convergence history is representative of all the cases presented in this study. 2500 iterations proved sufficient in attaining converged solutions.

D. PROGRAM CODES

The following codes are listed for reference. The ‘Overflow.in’ file was used in each test case for consistency. Modifications made within the OVERFLOW subroutines ‘bcnosl.F’, ‘bc.F’, ‘bcvwpox.F’ are denoted in boldface type and are remarked in italics.

1. Overflow.in
2. *bcnosl.F*
3. *bc.F*
4. *bcvwpox.F*

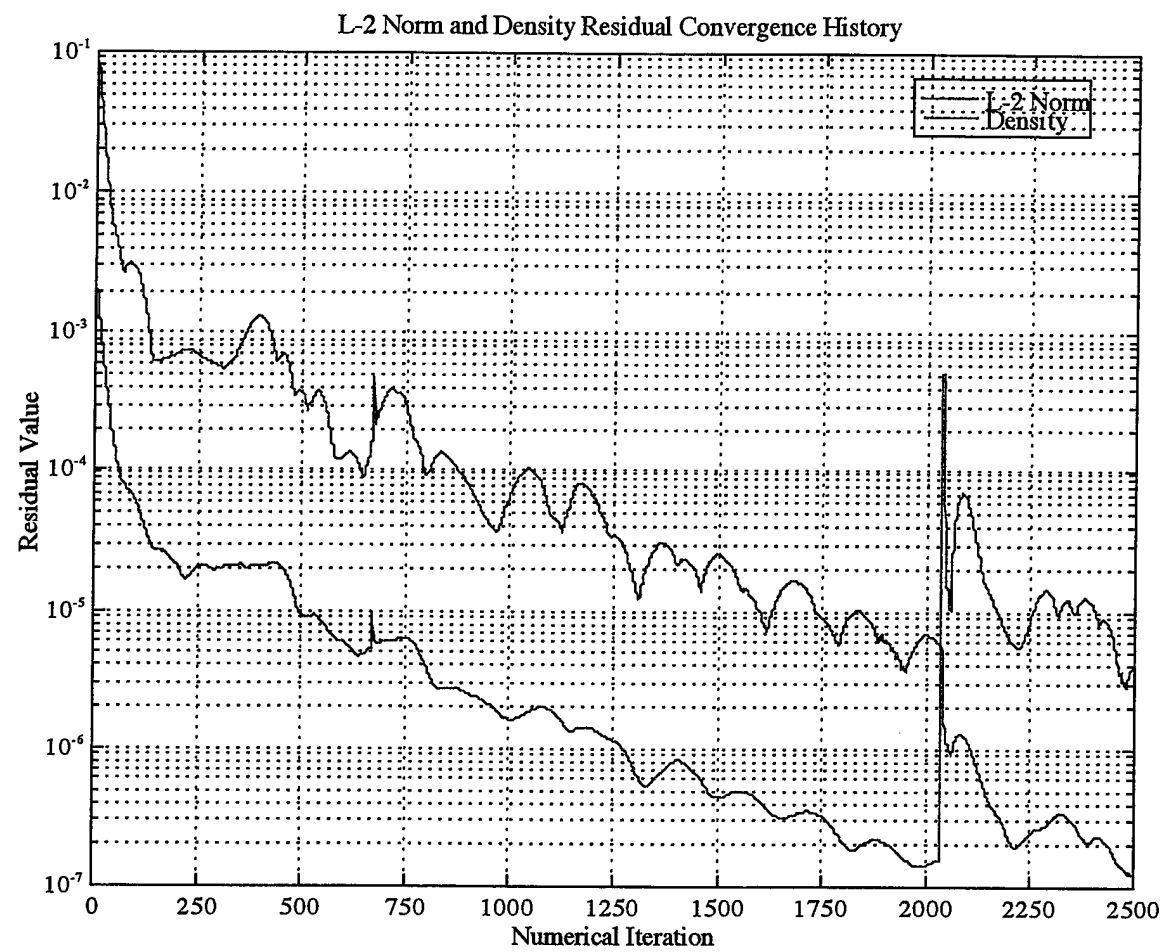


Figure A1. 333 Hz Case Convergence History

1. 'OVERFLOW.IN'

```
$GLOBAL
  CHIMRA= .F., NSTEPS=2500, RESTRT= .F., NSAVE =2500,
  NQT = 0,
  $SEND
$FLOINP
  ALPHA =0.0, FSMACH= 0.015, REY = 6.00E6, TINF = 520.000,
  $SEND
$VARGAM
  $SEND
$GRDNAM
  NAME = 'Viscous Flow Against Disk, 31x31x41',
  $END
$NITERS
  $SEND
$METPRM
  IRHS = 0, ILHS = 2, IDISS = 2,
  $SEND
$TIMACU
  DT = 0.5, ITIME= 1, TFOSO = 1.00, CFLMIN=0.01,
  $SEND
$SMOACU
  ISPECJ= 2, DIS2J = 2.00, DIS4J = 0.2,
  ISPECK= 2, DIS2K = 2.00, DIS4K = 0.2,
  ISPECL= 2, DIS2L = 2.00, DIS4L = 0.2,
  SMOO = 1.00,
  EPSE = 0.35,
  $SEND
$VISINP
  VISCJ = .F., VISCK = .F., VISCL = .F.,
  NTURB = 1,
  ITTYP = 1,
  ITDIR = -3,
  JTLS = 1,
  JTLE = 31,
  KTLS = 1,
  KTLE = 31,
  LTLS = 1,
  LTLE = 41,
  TLPAR1= 0.3,
  $SEND
$BCINP
  NBC = 6,
  IBTYP = 5,      1,      47,      47,      14,      10,
  IBDIR = -3,     -3,      3,       -2,       2,       1,
  JBCS = 1,        1,       1,       1,       1,       1,
  JBCE = 31,       31,      31,      31,      31,      1,
  KBCS = 1,        21,      1,       31,      1,       1,
  KBCE = 20,       31,      31,      31,      1,       31,
  LBCS = 41,       41,      1,       1,       1,       1,
  LBCE = 41,       41,      1,       41,      41,      41,
  $SEND
$SCEINP
$END
```

```

SUBROUTINE BCNOSL( IDIR,JS,JE,KS,KE,LS,LE,Q,
XX,XY,XZ,YX,YY,YZ,ZX,XY,ZZ,XT,YT,ZT,
JD,KD,LD,X,Y,Z )

% Set no-slip velocity condition at the wall.
% #include "precis.h"
DIMENSION Q(JD,KD,LD,5)
DIMENSION XX(JD,KD,LD), XY(JD,KD,LD), XZ(JD,KD,LD),
YX(JD,KD,LD), YY(JD,KD,LD), YZ(JD,KD,LD),
ZX(JD,KD,LD), ZY(JD,KD,LD), ZZ(JD,KD,LD),
XT(JD,KD,LD), YT(JD,KD,LD), ZT(JD,KD,LD),
X(JD,KD,LD), Y(JD,KD,LD), Z(JD,KD,LD),
%
PARAMETER ( I3=3 )
%
% First set contravariant velocity components to zero in Q(2-4).
%
CALL BCZERO( IDIR,JS,JE,KS,KE,LS,LE,I3,Q(1,1,1,2),JD,KD,LD )
%
% Then convert the contravariant velocity to cartesian momentum,
% including time-varying metric terms.
%
CALL UVWRHO( IDIR,
JS,JE,KS,KE,LS,LE,Q,
XX,XY,XZ,YX,YY,YZ,ZX,XY,ZZ,XT,YT,ZT,
JD,KD,LD )
%
% *** KJ Quinn edit 6/10/96 to include X,Y,Z in CALL statement and *****
% the following code to impose a counterclockwise velocity on the plate
% surface. The rotation rate is non-dimensionalized by the freestream
% speed of sound and the length scale of 1 radius. In addition, the
% UVWRHO subroutine which accounts for time metrics was commented.
% ***** ****
IADIR = ABS(IDIR)
PI = 4*ATAN(1.0)
RPM = 20000.00
AINF = 1127.7
RAD = 0.5

```

51

```

SUBROUTINE BC ( IGRID,ISTEP,NQ,NQT,NBC,IBTYP,P,JBDIR,
   JBCS,JBC,E,KBCS,LBCS,LBCE,BCPAR1,BCFILE,
   FSMACH,
   GAMINF,TINF,PINF,UINF,VINF,WINF,E0INF,
   JPER,JSYMS,JSYME,I2D,JAXI,
   KPER,KSYMS,KSYME,K2D,KAXI,
   LPER,LSYMS,LSYME,L2D,LAXI,
   Q,VGAMMA,TSCAL,IBLANK,X,Y,Z,
   VOL,XX,XY,XZ,YX,YY,YZ,ZX,ZZ,XT,YT,ZT,
   TMP,TMP2,
   JD,KD,LD,MD,M2D )

% Explicit boundary condition routines. These change ONLY Q(1-6).
% include "precis.h"
DIMENSION IBTYP(*),IBDIR(*),
   JBCS(*),JBC,E(*),KBCS(*),LBCE(*),
   BCPAR1(*)
CHARACTER(*),BCFILE(*)
LOGICAL JPER,KPER,LPER,J2D,K2D,L2D,JAXI,KAXI,LAXI
DIMENSION Q(JD,KD,LD,NQ)
DIMENSION VGAMMA(JD,KD,LD)
DIMENSION TSCAL(JD,KD,LD)
DIMENSION IBLANK(JD,KD,LD)
DIMENSION X(JD,KD,LD),Y(JD,KD,LD),Z(JD,KD,LD),
DIMENSION VOL(JD,KD,LD)
DIMENSION XX(JD,KD,LD),XY(JD,KD,LD),XZ(JD,KD,LD),
   YX(JD,KD,LD),YY(JD,KD,LD),YZ(JD,KD,LD),
   ZX(JD,KD,LD),ZY(JD,KD,LD),ZZ(JD,KD,LD),
   XT(JD,KD,LD),YT(JD,KD,LD),ZT(JD,KD,LD)
DIMENSION TMP(MD,2),TMP2(MD,5)

LOGICAL SLOWST
LOGICAL QVELS
PARAMETER ( QVELS=.TRUE. )
PARAMETER ( II=1,I2=2,I3=3,I6=6 )

% Develop rules for faster convergence:
% o Use slow-start of wall boundary conditions if the freestream Mach
% number is above 0.5.
% SLOWST = .FALSE.
IF (FSMACH.GT.0.5) SLOWST = .TRUE.

% Process list of boundary conditions.

DO 10 IB=1,NBC
  IDIR = IBDIR(IB)
  JS = JBCS(IB)
  JE = JBCE(IB)
  KS = KBCS(IB)
  KE = KBCE(IB)
  LS = LBCE(IB)
  LE = LBCE(IB)

% WALL BOUNDARY CONDITIONS.

% Inviscid adiabatic solid wall: density extrapolation,
% tangency and pressure extrapolation (with slow start).
% NO IBLANK REQD.
% IF (IBTYP(IB).EQ. 1) THEN
  CALL BCIWPX( IDR,ISTEP,SLOWST,NSLOW,
   RINF,UINF,VINF,WINF,E0INF,GAMINF,
   JS,JE,KS,KE,LS,LE,
   I6,Q,VGAMMA,X,Y,Z,
   XX,XY,XZ,YX,YY,YZ,ZX,ZZ,XT,YT,ZT,
   JD,KD,LD )

% Inviscid adiabatic solid wall: internal energy extrapolation,
% tangency and normal momentum (with slow-start).
% (Do this after symmetry conditions, etc. Pressure at edges may be

```

```

% lagged.)
% NEEDS IBLANK.

% ELSE IF (IBTYP(B),EQ. 2) THEN
CALL BCWAL(IDIR,ISTEP,SLOWST,NSLOW,
RINF,UINF,VINF,WINF,E0INF,GAMINF,
JPER,JSYMS,JSYME,J2D,JAXI,
KPER,KSYMS,KSYME,K2D,KAXI,
LPER,LSYMS,LSYME,L2D,LAXI,
JS,JE,KS,KE,L,S,LE,
I6,Q,VGAMMA,X,Y,Z,IBLANK,
XX,XY,XZ,YY,YZ,ZX,ZY,ZZ,XT,YT,ZT,
TMP2,
JD,KD,LD,M2D)

% Inviscid constant temperature solid wall: constant wall
% temperature, tangency and pressure extrapolation (with slow start).
% NO IBLANK REQD.

% ELSE IF (IBTYP(B),EQ. 3) THEN
CALL BCWP(B,DIR,ISTEP,SLOWST,NSLOW,
TINF,BCPAR1(B),
RINF,UINF,VINF,WINF,E0INF,GAMINF,
JS,JE,KS,KE,L,S,LE,
I6,Q,VGAMMA,X,Y,Z,
XX,XY,XZ,YY,YZ,ZX,ZY,ZZ,XT,YT,ZT,
JD,KD,LD)

% Inviscid constant temperature solid wall: constant wall
% temperature, tangency and normal momentum (with slow-start).
% (Do this after symmetry conditions, etc. Pressure at edges may be
% lagged.)
% NEEDS IBLANK.

% ELSE IF (IBTYP(B),EQ. 4) THEN
CALL BCWAT(IDIR,ISTEP,SLOWST,NSLOW,
TINF,BCPAR1(B),
RINF,UINF,VINF,WINF,E0INF,GAMINF,
JPER,JSYMS,JSYME,J2D,JAXI,

```

***** KJ Quinn edit 6/10/96 to include X,Y,Z in CALL statement *****

```

ELSE IF (IBTYP(B),EQ. 5) THEN
CALL BCWP(B,DIR,ISTEP,SLOWST,NSLOW,
RINF,UINF,VINF,WINF,E0INF,GAMINF,
JS,JE,KS,KE,L,S,LE,
I6,Q,VGAMMA,
XX,XY,XZ,YY,YZ,ZX,ZY,ZZ,XT,YT,ZT,
JD,KD,LD,X,Y,Z)
% Viscous adiabatic solid wall: internal energy extrapolation,
% no slip and normal momentum (with slow-start).
% (Do this after symmetry conditions, etc. Pressure at edges may be
% lagged.)
% NEEDS IBLANK.

ELSE IF (IBTYP(B),EQ. 6) THEN
CALL BCWAL(IDIR,ISTEP,SLOWST,NSLOW,
RINF,UINF,VINF,WINF,E0INF,GAMINF,
JPER,JSYMS,JSYME,J2D,JAXI,
KPER,KSYMS,KSYME,K2D,KAXI,
LPER,LSYMS,LSYME,L2D,LAXI,
JS,JE,KS,KE,L,S,LE,
I6,Q,VGAMMA,IBLANK,
XX,XY,XZ,YY,YZ,ZX,ZY,ZZ,XT,YT,ZT,
TMP2,
JD,KD,LD,M2D)

```

```

% Viscous constant temperature solid wall: constant wall
% temperature, no slip and pressure extrapolation (with slow-start).
% NO IBLANK REQD.
%
ELSE IF (IBTYP(IB).EQ. 7) THEN
  CALL BCWWPT (IDIR,ISTEP,SLOWST,NSLOW,
               TINF,BCPAR1(IB),
               RINF,UINF,VINF,WINF,E0INF,GAMINF,
               JS,JE,KS,KE,L,S,LE,
               I6,Q,VGAMMA,
               XX,XY,XZ,YY,YZ,ZX,ZY,ZZ,XT,YT,ZT,
               JD,KD,LD)
%
% Viscous constant temperature solid wall: constant wall
% temperature, no slip and normal momentum (with slow-start).
% (Do this after symmetry conditions, etc. Pressure at edges may be
% lagged.)
% NEEDS IBLANK.
%
ELSE IF (IBTYP(IB).EQ. 8) THEN
  CALL BCWwat (IDIR,ISTEP,SLOWST,NSLOW,
               TINF,BCPAR1(IB),
               RINF,UINF,VINF,WINF,E0INF,GAMINF,
               JPER,JSYMS,JSYME,J2D,JAXI,
               KPER,KSYMS,KSYME,K2D,KAXI,
               LPER,LSYMS,LSYME,L2D,LAXI,
               JS,JE,KS,KE,L,S,LE,
               I6,Q,VGAMMA,IBLANK,
               XX,XY,XZ,YY,YZ,ZX,ZY,ZZ,XT,YT,ZT,
               TMP2,
               JD,KD,LD,M2D )
C
% GRID TOPOLOGY-RELATED BOUNDARY CONDITIONS.
%
% Periodic conditions are handled implicitly. Just overload last
% plane here.
% NO IBLANK REQD.
%
ELSE IF (IBTYP(IB).EQ.10) THEN
  CALL BCPER (IDIR,JS,JE,KS,KE,L,S,LE,NQ-NQT,Q,JD,KD,LD)
%
% Symmetry conditions: reflect Q about symmetry plane, zero
% perpendicular velocity on symmetry plane.
% NO IBLANK REQD.
%
ELSE IF (IBTYP(IB).EQ.11) THEN
  CALL BCSYM (IDIR,QVELS,I1,JS,JE,KS,KE,L,S,LE,I6,Q,
              JD,KD,LD)
%
ELSE IF (IBTYP(IB).EQ.12) THEN
  CALL BCSYM (IDIR,QVELS,I2,JS,JE,KS,KE,L,S,LE,I6,Q,
              JD,KD,LD)
%
ELSE IF (IBTYP(IB).EQ.13) THEN
  CALL BCSYM (IDIR,QVELS,I3,JS,JE,KS,KE,L,S,LE,I6,Q,
              JD,KD,LD)
%
% Axis condition: 0th- or 1st-order extrapolation to set slope at the
% axis to zero, then average around the axis.
% (Watch for extra points from symmetry condition. Exclude these from
% axis B%and do symmetry condition(s) after.)
% NEEDS IBLANK.
%
ELSE IF (IBTYP(IB).EQ.14) THEN
  CALL BCAXJ (IDIR,QVELS,JPER,JSYMS,JSYME,JAXI,KS,KE,L,S,LE,
              BCPAR1(IB),
              I6,Q,IBLANK,TMP(1,1),TMP(1,2),
              JD,KD,LD,MD)
%
ELSE IF (IBTYP(IB).EQ.15) THEN
  CALL BCAXK (
    IDIR,QVELS,JS,JE,KPER,KSYMS,KSYME,KAXI,L,S,LE,
    BCPAR1(IB),
    I6,Q,IBLANK,TMP(1,1),TMP(1,2),
    JD,KD,LD,MD)
%
ELSE IF (IBTYP(IB).EQ.16) THEN
  CALL BCAXL (
    IDIR,QVELS,JS,JE,KS,KE,L,PER,LSYMS,LSYME,LAXI,
    BCPAR1(IB),
    I6,Q,IBLANK,TMP(1,1),TMP(1,2),
    JD,KD,LD,MD)
%
% 2D condition: zero v velocity component and copy center plan

```

```

% into outer planes.
% NO IBLANK REQ'D.
%
% ELSE IF (IBTYP(IB),EQ.21) THEN
CALL BC2D ( IDIR,QVELS,JS,JE,KS,KE,LS,LE,I6,Q,
          JD,KD,LD )
%
% Axisymmetric condition: zero v velocity component and rotate center
plane about x into outer planes.
% NO IBLANK REQ'D.
%
% ELSE IF (IBTYP(IB),EQ.22) THEN
CALL BCAXSY( IDIR,QVELS,JS,JE,KS,KE,LS,LE,I6,Q,
          JD,KD,LD )
%
% OUTFLOW BOUNDARY CONDITIONS.
%
% Standard outflow condition: pure extrapolation.
% NO IBLANK REQ'D.
%
% ELSE IF (IBTYP(IB),EQ.30) THEN
CALL BCOOUT ( IDIR,JS,JE,KS,KE,LS,LE,I6,Q,JD,KD,LD )
%
% Characteristic condition: fix or extrapolate
% tangential velocity, entropy, and Riemann invariants.
% NO IBLANK REQ'D.
%
% ELSE IF (IBTYP(IB),EQ.31) THEN
CALL BCCHAR( IDIR,
          JS,JE,KS,KE,LS,LE,
          I6,Q,VGAMMA,X,Y,Z,
          XX,XY,XZ,YY,YZ,ZX,ZY,ZZ,XT,YT,ZT,
          JD,KD,LD )
%
% Supersonic/subsonic inflow/outflow boundary condition:
% supersonic inflow: fix (leave) everything;
% subsonic inflow: extrapolate pressure;
% subsonic outflow: extrapolate everything but pressure;
% subsonic outflow: extrapolate everything.
%
% NO IBLANK REQ'D.
%
% ELSE IF (IBTYP(IB),EQ.32) THEN
CALL BCSSIO( IDIR,
          JS,JE,KS,KE,LS,LE,
          Q,VGAMMA,X,Y,Z,
          XX,XY,XZ,YY,YZ,ZX,ZY,ZZ,XT,YT,ZT,
          JD,KD,LD )
%
% Specified pressure outflow condition: fix pressure, extrapolate
% everything else (with slow-start).
% NO IBLANK REQ'D.
%
% ELSE IF (IBTYP(IB),EQ.33) THEN
CALL BCPFIX( IDIR,ISTEP,SLOWST,NSLOW,
          PINF,BCPAR1(IB),
          RINF,UINF,VINF,WINF,E0INF,GAMINF,
          JS,JE,KS,KE,LS,LE,
          Q,VGAMMA,
          JD,KD,LD )
%
% INFLOW BOUNDARY CONDITIONS.
%
% Freestream condition: impose freestream values.
% NO IBLANK REQ'D.
%
% ELSE IF (IBTYP(IB),EQ.40) THEN
CALL BCFREE( IDIR,RINF,UINF,VINF,WINF,E0INF,GAMINF,
          JS,JE,KS,KE,LS,LE,Q,
          JD,KD,LD )
%
% Nozzle condition: hold p(0), T(0), flow angle constant,
% extrapolate Riemann invariant R2 (with slow-start).
% NO IBLANK REQ'D.
%
% ELSE IF (IBTYP(IB),EQ.41) THEN
CALL BCNOZ ( IDIR,ISTEP,SLOWST,NSLOW,
          RINF,UINF,VINF,WINF,E0INF,GAMINF,
          JS,JE,KS,KE,LS,LE,
          JD,KD,LD )

```

```

16,Q,VGAMMA,X,Y,Z,
XX,XY,XZ,YY,YZ,ZX,ZY,ZZ,XT,YT,ZT,
JD,KD,LD)
%
% Prescribed Q (read once from file).
%
% NO IBLANK REQ'D.
%
ELSE IF (IBTYP(B) EQ 42) THEN
  CALL BCREAD(IDIR,ISTEP,BCPAR1(B),.FALSE.,.FALSE.,NSLOW,
  BCFILE(B),NQ,
  RINF,UINF,VINF,WINF,E0INF,GAMINF,
  JS,JE,KS,KE,LS,LE,Q,
  JD,KD,LD)
  CALL BCSSIO(IDIR,
  JS,JE,KS,KE,LS,LE,
  Q,VGAMMA,X,Y,Z,
  XX,XY,XZ,YY,YZ,ZX,ZY,ZZ,XT,YT,ZT,
  JD,KD,LD)

%
% Prescribed Q/characteristic condition with slow start.
%
% NO IBLANK REQ'D.

%
ELSE IF (IBTYP(B) EQ 46) THEN
  CALL BCREAD(IDIR,ISTEP,BCPAR1(B),.TRUE.,.TRUE.,NSLOW,
  BCFILE(B),NQ,
  RINF,UINF,VINF,WINF,E0INF,GAMINF,
  JS,JE,KS,KE,LS,LE,Q,
  JD,KD,LD)
  CALL BCSSIO(IDIR,
  JS,JE,KS,KE,LS,LE,
  Q,VGAMMA,X,Y,Z,
  XX,XY,XZ,YY,YZ,ZX,ZY,ZZ,XT,YT,ZT,
  JD,KD,LD)

%
% Prescribed Q with slow-start (read from file).
%
% NO IBLANK REQ'D.

%
ELSE IF (IBTYP(B) EQ 43) THEN
  CALL BCREAD(IDIR,ISTEP,BCPAR1(B),.FALSE.,.TRUE.,NSLOW,
  BCFILE(B),NQ,
  RINF,UINF,VINF,WINF,E0INF,GAMINF,
  JS,JE,KS,KE,LS,LE,Q,
  JD,KD,LD)
  CALL BCSSIO(IDIR,
  JS,JE,KS,KE,LS,LE,
  Q,VGAMMA,X,Y,Z,
  XX,XY,XZ,YY,YZ,ZX,ZY,ZZ,XT,YT,ZT,
  JD,KD,LD)

%
% Actuator disk: average Q and impose delta p on two adjacent planes.
%
% NO IBLANK REQ'D.
%
% Freestream/characteristic condition.
%
% NO IBLANK REQ'D.

%
ELSE IF (IBTYP(B) EQ 47) THEN
  CALL BCFREE(IDR,RINF,UINF,VINF,WINF,E0INF,GAMINF,
  JS,JE,KS,KE,LS,LE,Q,
  JD,KD,LD)
  CALL BCSSIO(IDIR,
  JS,JE,KS,KE,LS,LE,
  Q,VGAMMA,X,Y,Z,
  XX,XY,XZ,YY,YZ,ZX,ZY,ZZ,XT,YT,ZT,
  JD,KD,LD)

%
% Prescribed Q/characteristic condition.
%
% NO IBLANK REQ'D.

%
ELSE IF (IBTYP(B) EQ 45) THEN

```

```

% Default boundary condition (no change).
% NO IBLANK REQD.

% ELSE IF (IBTYP(IB),EQ.49) THEN
% % FLOW-THROUGH BOUNDARY CONDITIONS.
%
% C-grid flow-through: average values one point above and
% below cut. Grid points line up. Region specified corresponds to
% one side of the flow-through cut.
% NO IBLANK REQD.

% ELSE IF (IBTYP(IB),EQ.51) THEN
CALL BCCJ (IDIR,JS,JE,KS,KE,LS,LE,I6,Q,JD,KD,LD)
ELSE IF (IBTYP(IB),EQ.52) THEN
CALL BCCK (IDIR,JS,JE,KS,KE,LS,LE,I6,Q,JD,KD,LD)
ELSE IF (IBTYP(IB),EQ.53) THEN
CALL BCCL (IDIR,JS,JE,KS,KE,LS,LE,I6,Q,JD,KD,LD)

% Fold-over cut flow-through: average values one point above and
% below cut. Points don't line up (values are interpolated and
% smoothed).
% NEEDS IBLANK.

% ELSE IF (IBTYP(IB),EQ.54) THEN
CALL BCCTJ (IDIR,IPER,KPER,LPER,
JS,JE,KS,KE,LS,LE,X,Y,Z,I6,Q,IBLANK,
TMP2(1,1),TMP(1,1),TMP(1,2),
JD,KD,LD,MD,M2D )
ELSE IF (IBTYP(IB),EQ.55) THEN
CALL BCCTK (IDIR,JPER,KPER,LPER,
JS,JE,KS,KE,LS,LE,X,Y,Z,I6,Q,IBLANK,
TMP2(1,1),TMP(1,1),TMP(1,2),
JD,KD,LD,MD,M2D )
ELSE IF (IBTYP(IB),EQ.56) THEN
CALL BCCTL (IDIR,JPER,KPER,LPER,
JS,JE,KS,KE,LS,LE,X,Y,Z,I6,Q,IBLANK,
TMP2(1,1),TMP(1,1),TMP(1,2),
JD,KD,LD,MD,M2D )

% MODIFY IBLANK CONDITIONS.
%
% Blank out region (set IBLANK=0).
% This was done in BCCHEK, called from INITIA.

% ELSE IF (IBTYP(IB),EQ.61) THEN
% % COPY TO/FROM CONDITION.
%
% Copy to: next boundary condition specifies matching "from" region.
% NO IBLANK REQD.

% ELSE IF (IBTYP(IB),EQ.70) THEN
IBP = IB+1
CALL BCTOFR (IDIR,JS,JE,KS,KE,LS,LE,
IBCS(IBP),IBCE(IBP),KBCS(TBP),KBCE(TBP),
LBCS(TBP),LBCE(TBP),
I6,Q,
JD,KD,LD)

% Copy from: do nothing.

% ELSE IF (IBTYP(IB),EQ.71) THEN
% % WIND TUNNEL WALL CONDITIONS.
%
% Slotted wind tunnel wall: density extrapolation, normal velocity
% extrapolation and pressure extrapolation (with slow-start).
% NO IBLANK REQD.

% ELSE IF (IBTYP(IB),EQ.81) THEN
CALL BCPRPX (IDIR,ISTEP,SLOWST,NSLOW,
BCPAR (IB),
RINF,UINF,VINF,WINF,E0INF,GAMINF,
JS,JE,KS,KE,LS,LE,
I6,Q,VGAMMA,X,Y,Z,
XX,XY,XZ,YY,YZ,ZX,ZY,ZZ,XT,YT,ZT,
JD,KD,LD)

```

```
%  
% Unknown boundary condition. This is a programming error, since  
% it got past routine BCCHEK without being caught.  
%  
ELSE  
    WRITE(*,9) IBTYP(IB),IGRID  
    9 FORMAT(7** ERROR ** UNKNOWN BOUNDARY CONDITION TYPE  
           ,  
           15,'IN GRID ',15)  
    STOP BC  
ENDIF  
10 CONTINUE  
%  
% RETURN  
END
```

```

SUBROUTINE BCWWPX( IDIR,ISTEP,SLOWST,NSLOW,
& RINF,UINF,VINF,WINF,E0INF,GAMINF,
& JS,JE,KS,KE,LS,LE,
& NO,Q,VGAMMA,
& XX,XY,XZ,YX,YY,YZ,ZX,ZY,ZZ,XT,YT,ZT,
& JD,KD,LD,XX,YY,ZZ )
% ** KJ Quinn edit 6/10/96 to include X,Y,Z in SUB statement ***
%
% Viscous, adiabatic% solid wall: density extrapolation,
% no slip and pressure extrapolation (with slow-start).
%
% Viscous solid wall: no slip and pressure extrapolation (with slow-start).
%
% NO IBLANK REQD.
%
#include "precis.h"
LOGICAL SLOWST
DIMENSION Q(JD,KD,LD,NQ)
DIMENSION VGAMMA(JD,KD,LD)
DIMENSION XX(JD,KD,LD), XY(JD,KD,LD), XZ(JD,KD,LD),
& YY(JD,KD,LD), YZ(JD,KD,LD), YZ(JD,KD,LD),
& ZX(JD,KD,LD), ZY(JD,KD,LD), ZZ(JD,KD,LD),
& XT(JD,KD,LD), YT(JD,KD,LD), ZT(JD,KD,LD)

PARAMETER ( I1=1 )

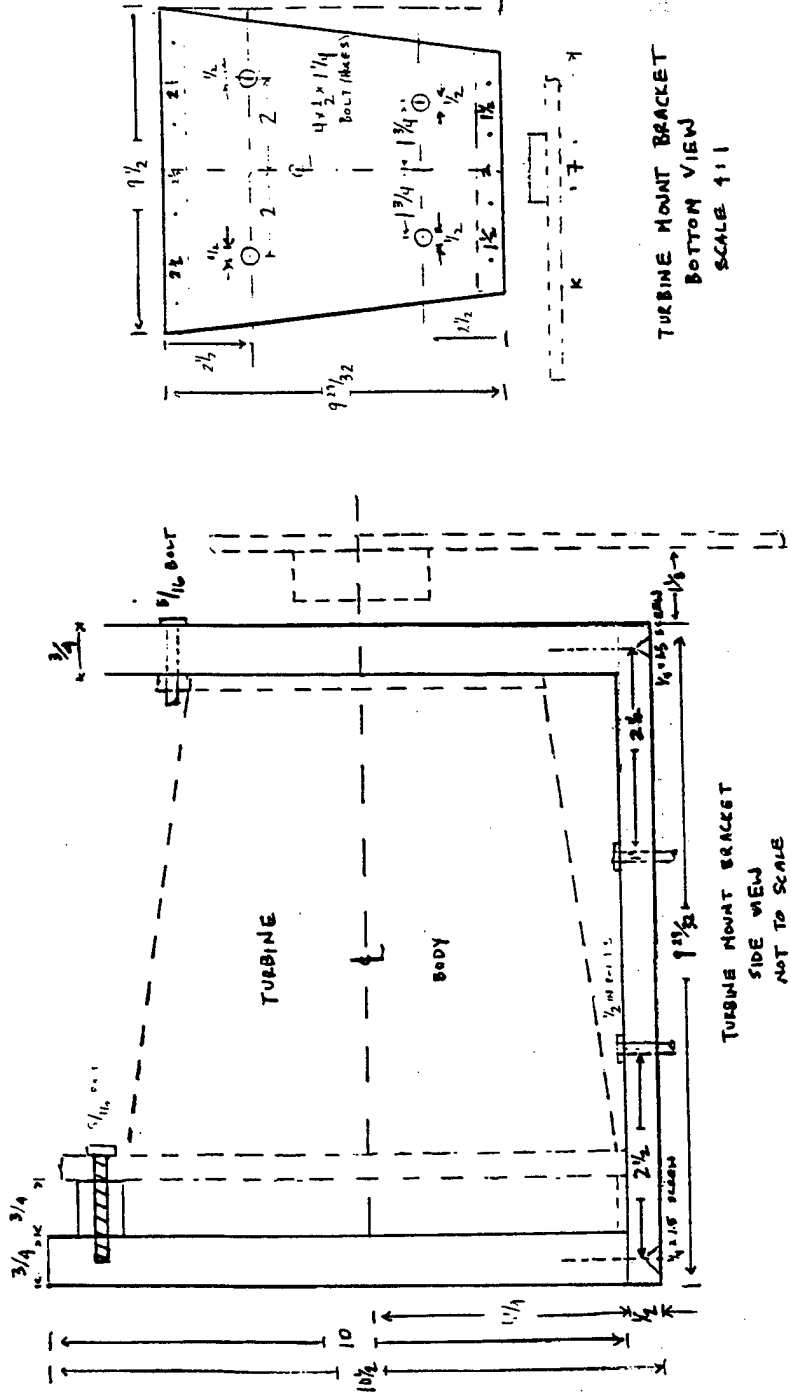
%
% Extrapolate other Q variables.
%
CALL BCQX ( IDIR,JS,JE,KS,KE,LS,LE,I1,Q(1,1,1,1),JD,KD,LD )
%
% Extrapolate density.
%
CALL BCQX ( IDIR,JS,JE,KS,KE,LS,LE,Q(1,1,1,1),JD,KD,LD )

%
% Set velocity to no-slip.
%
***** KJ Quinn edit 6/10/96 to include X,Y,Z in CALL statement *****
%
% CALL BCNOSL(IDIR,
& JS,JE,KS,KE,LS,LE,Q,
& XX,XY,XZ,YX,YY,YZ,ZX,XY,ZZ,XT,YT,ZT,

```


APPENDIX B.
TURBINE APPARATUS MECHANICAL DRAWINGS

1. Hamilton Standard TPC13 Turbine Mounting Bracket Sideview / Topview
2. Hamilton Standard TPC13 Turbine Mounting Bracket Front / Back View
3. Hamilton Standard TPC13 Turbine Mount / Spin Chamber Interface
4. LED / Photodiode Mount Bracket Views
5. Turbine Connecting Flange



KEVIN QUINN
 21 APRIL 1996
 ROTARY PSP MEASUREMENT THISIS PROJECT
 TURBINE MOUNT BRACKET
 SCALE 4:1
 DIMENSIONS IN INCHES

Figure B1. Turbine Mounting Bracket Detailed Drawing; Side / Bottom Views

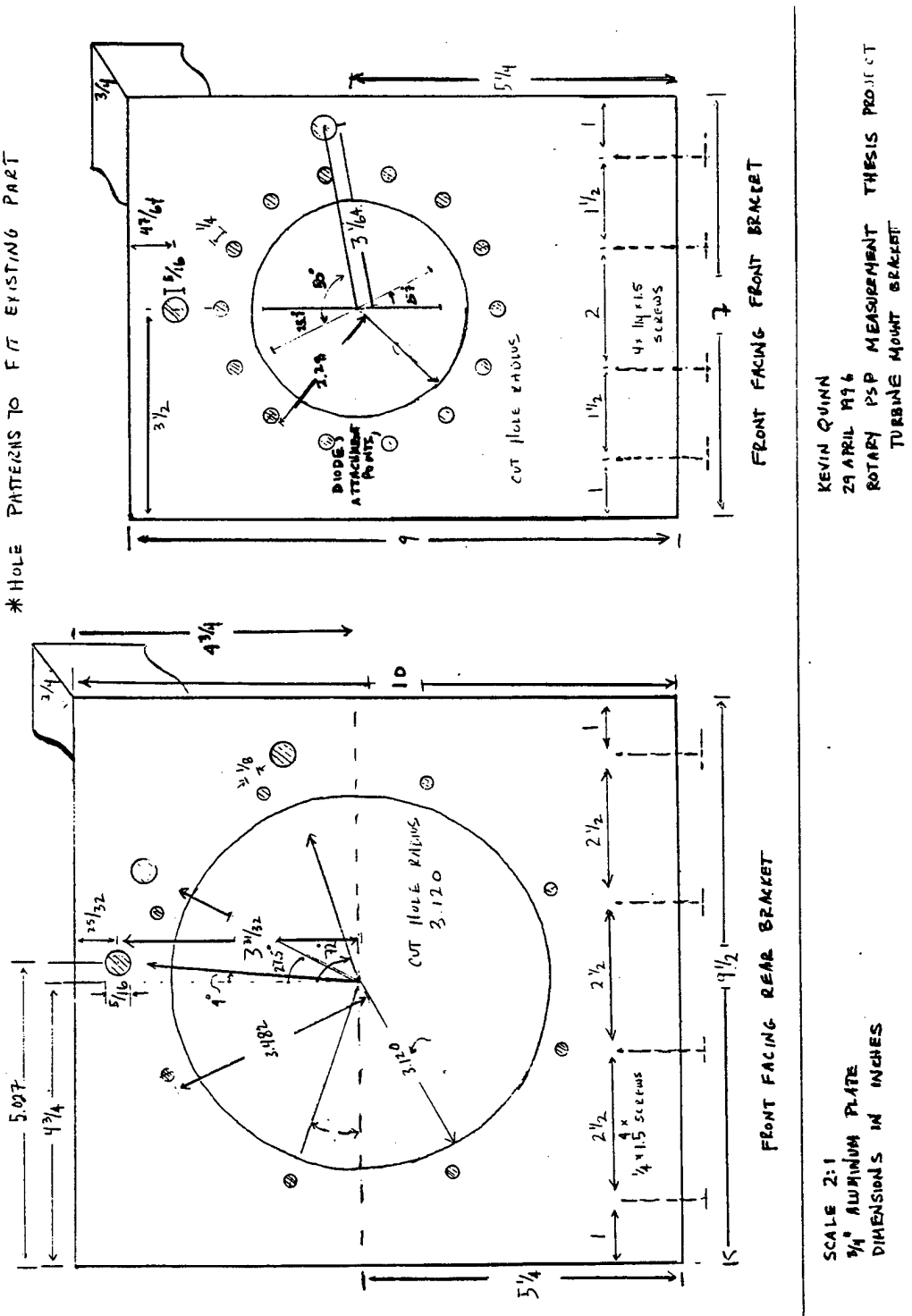


Figure B2. Turbine Mounting Bracket Detailed Drawing; Front / Rear Views

KEVIN QUINN
29 APRIL 1996
ROTARY PSP MEASUREMENT
TURBINE MOUNT BRACKET
THESIS PROJCT

KEVIN QUINN
29 APRIL 1996

SCALE 2:1
3/4" ALUMINUM PLATE
DIMENSIONS IN INCHES

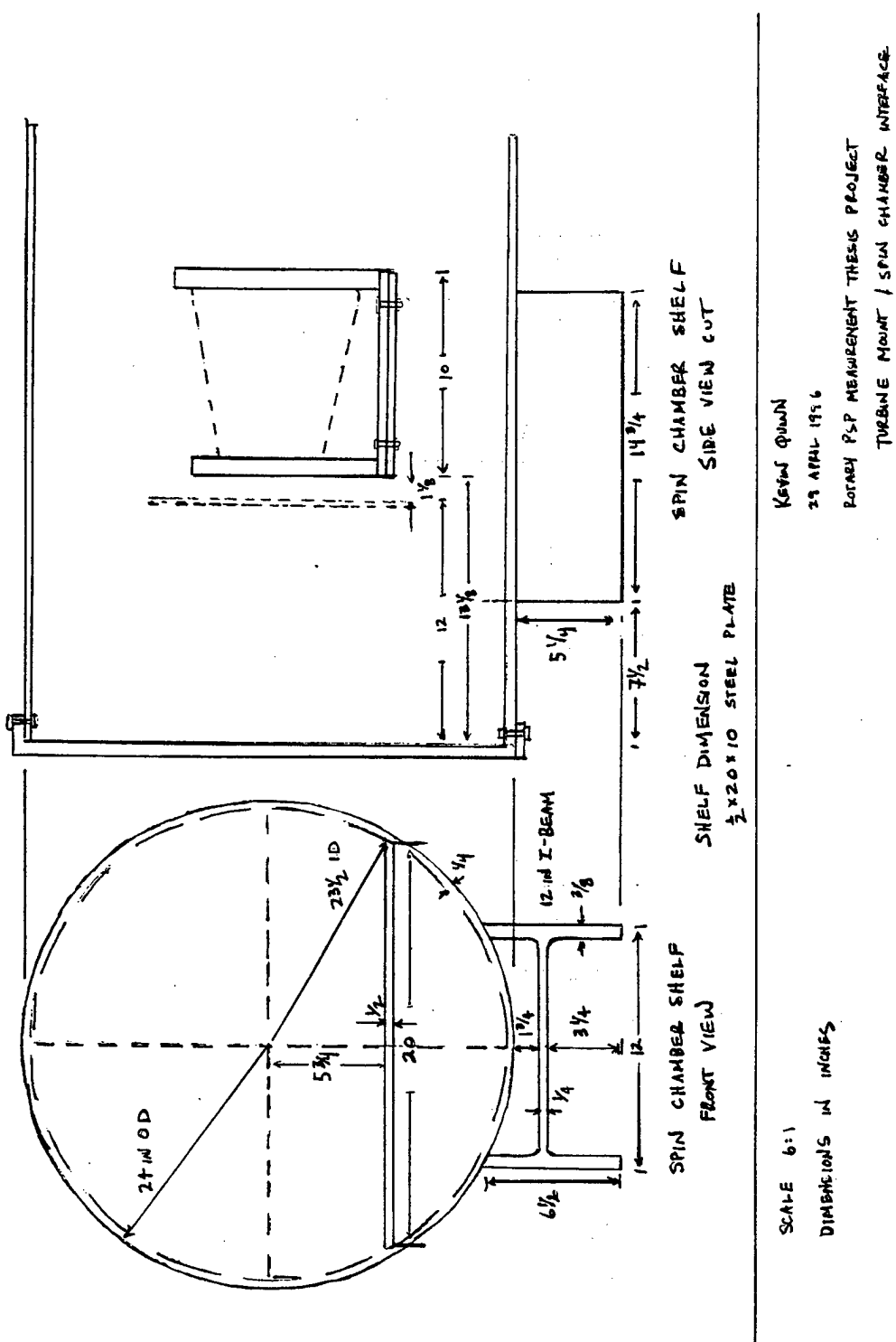


Figure B3. Turbine Mounting Bracket / Spin Chamber Interface Drawing

LED / PHOTOTRANSISTOR BRACKET
PSP MEASUREMENT THESIS
9 JULY 1996

KEVIN QUINN X 3463
PROFESSOR R. SHREEVE,
ADVISOR

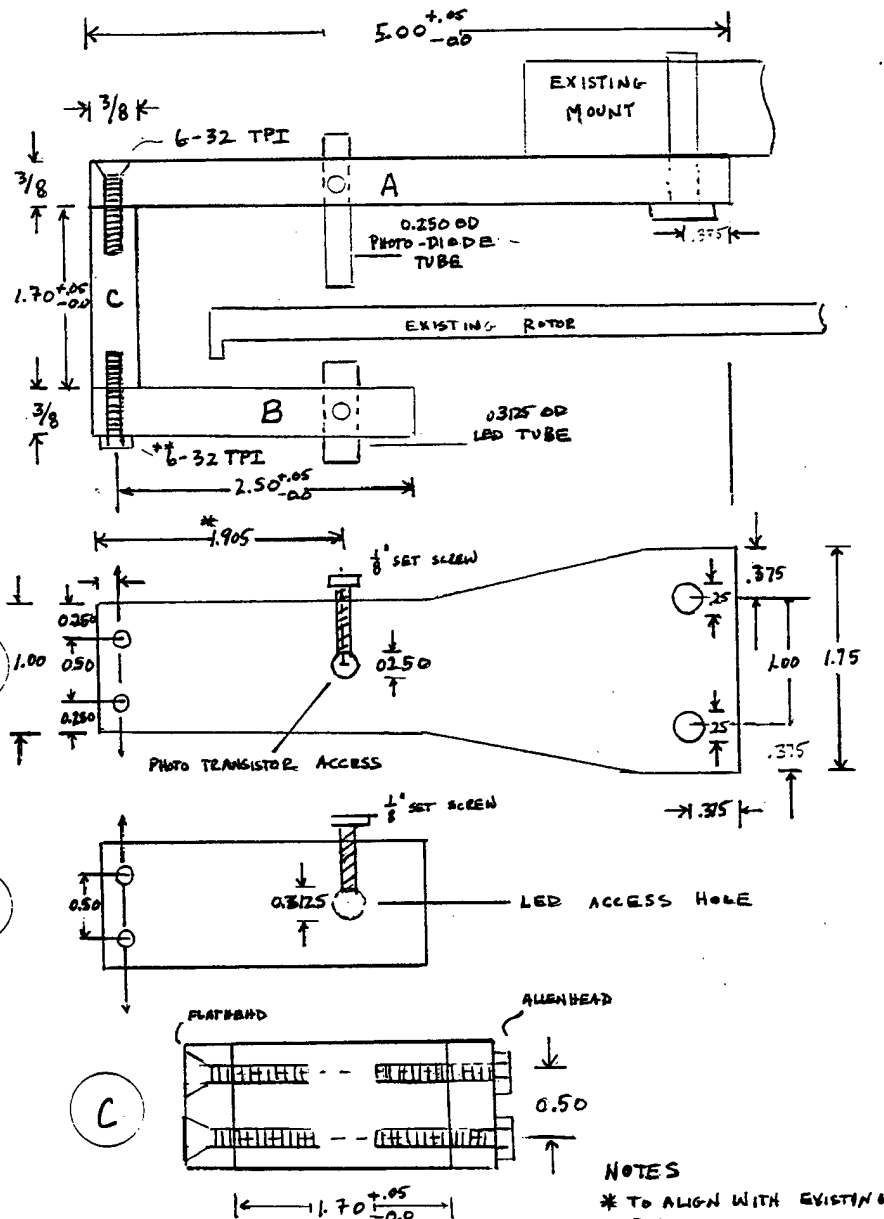


Figure B4. Light Emitting Diode / Photodiode Bracket Detailed Drawing

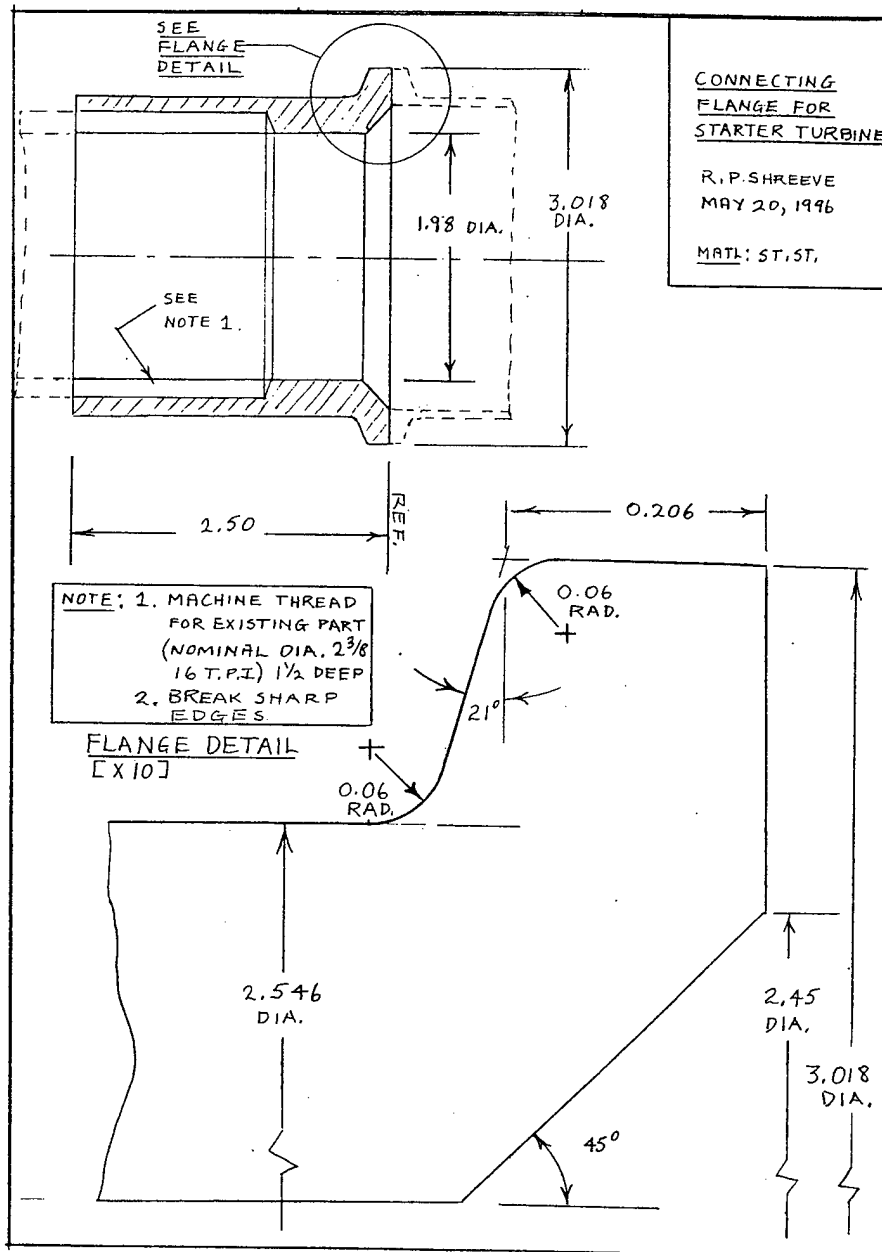


Figure B5. Turbine Connecting Flange Detailed Drawing

APPENDIX C.

CIRCUIT DESIGN

1. BCD Counter Circuit
2. Power Supply Circuit
3. Waveshaper Redesign Proposal

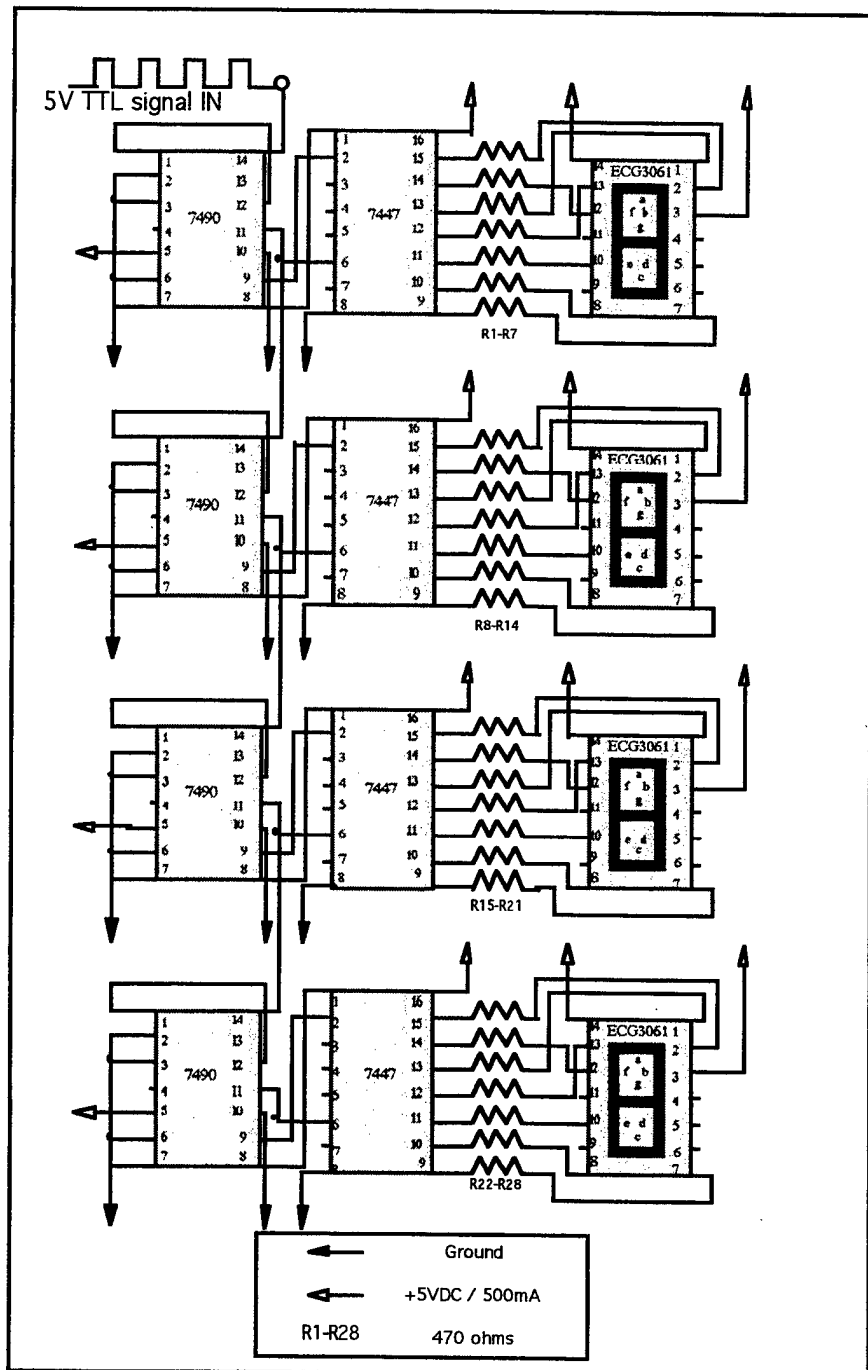
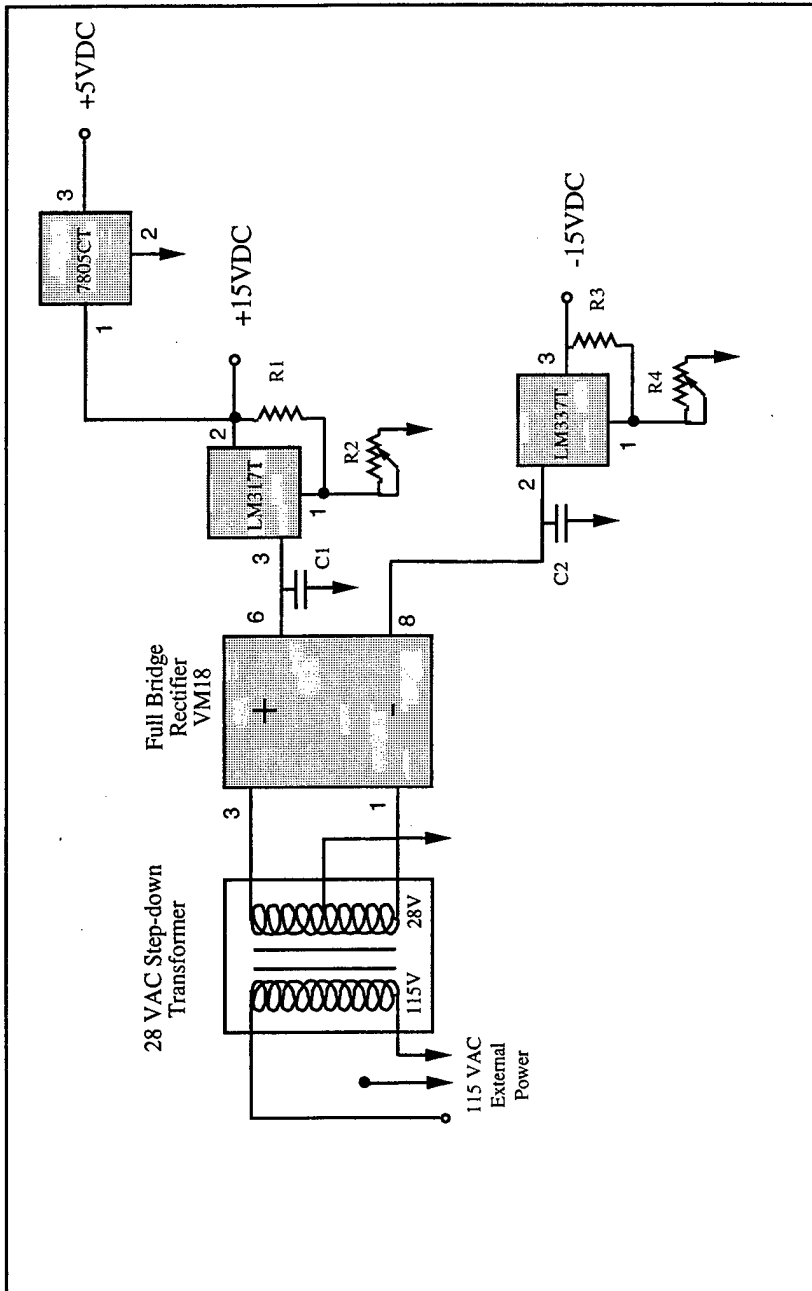


Figure C1. BCD Counter Circuit



VM18 IC	Full Bridge Rectifier IC	C1, C2 47 μ F (0-50V)
LM317T	Voltage Regulator	R1, R3 390 Ω
LM337T	Voltage Regulator	R2, R4 0-10k Ω
7805CT	Voltage Regulator	

Figure C2. Power Supply Circuit

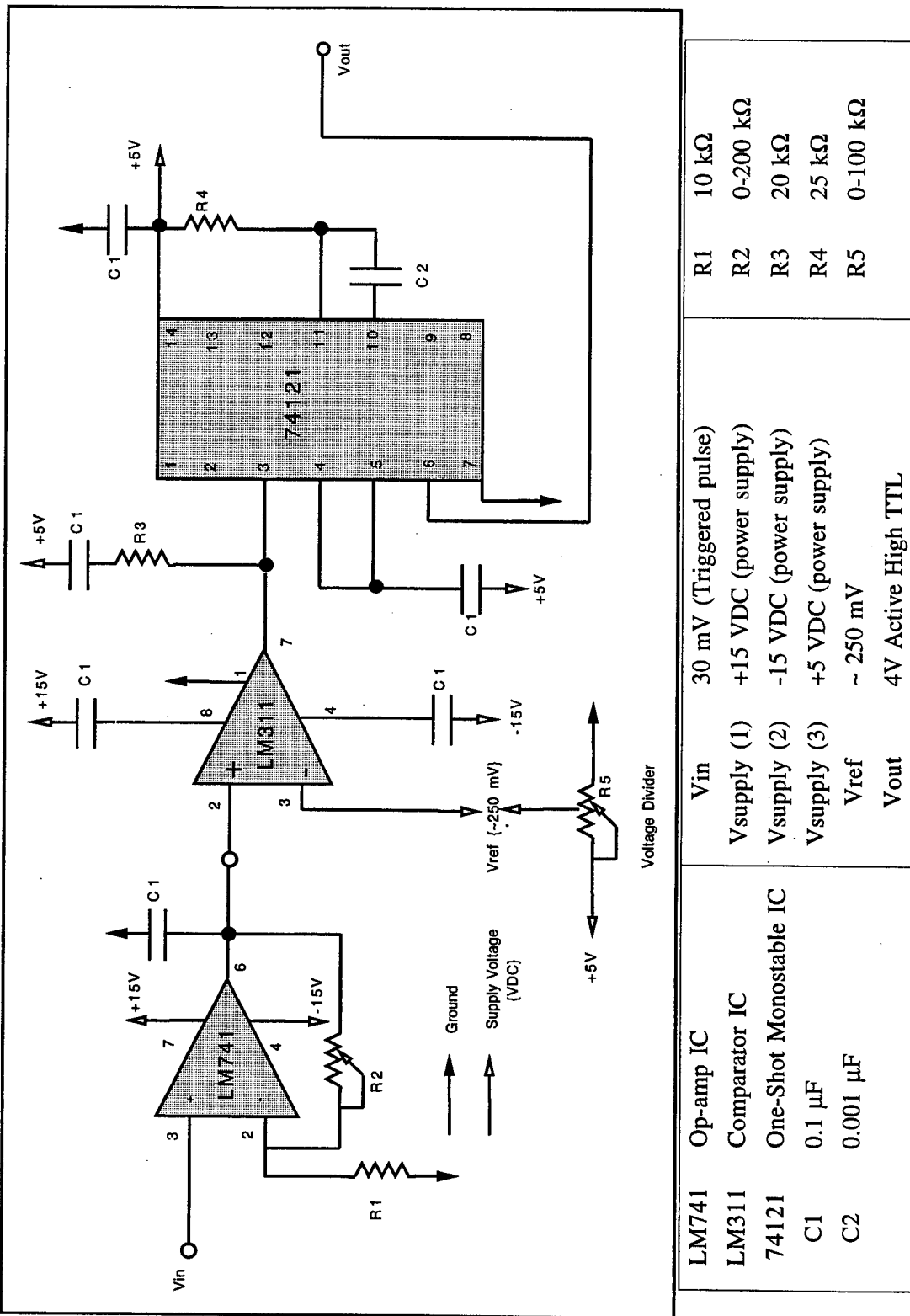


Figure C3. Proposed One-shot Monostable Waveshaper Circuit Schematic

APPENDIX D. ***4MIP TOOL SCRIPTED MACROS***

The scripting of the imaging process allowed for repetitive, 'hands off' measurements and gave the tester the ability to monitor the overall process. The scripts were developed using the TEACH / EXECUTE SCRIPT menu in the EPIX *4MIP TOOL* software. This menu option recorded keyboard stroke inputs in a executable text file. Subsequent execution of the text file allowed the software to emulate the recorded keystrokes. Because of the large memory requirement per image, the software was best able to acquire, store, and manipulate the data by first executing the SPLIT SCREEN option to alleviate the need to exit and switch between menus during the script execution (EPIX Users Manual, 1993). The scripts were saved under the path and suffix \4MIP\SCRIPTS\name.MPX.

The imaging process commenced with the execution of the script PSP_PIC.MPX which first executed a split screen and commenced a series of image captures to fill the available 11 segmented memory buffers. A sub-script denoted CHECKER.MPX was then initiated three times in a sequence. This script execution resulted in a video-like play back of the 11 buffers, providing a visual check for error within the data. With the data checked, the script then executed another sub-script, PSP_AVG, which averaged the 11 images in the SEQUENCE OPERATIONS menu. The resulting image was then saved as IMAGE1.TIF. The process was then repeated with the second image saved as IMAGE2.TIF. The final image was developed by loading and averaging the two images. The file was saved using the file naming protocol shown in Table 6. The scripts listed in this Appendix follow:

1. *PSP_PIC.MPX*
2. *CHECKER.MPX*
3. *PSP_AVG.MPX*

FSR FIG.MPX		
{!}KEY 0x5900 SF6	!CurrentImageBuffer 6	/checker.mpx
^Screen1Height 10	{!}KEY 0x4000 F6	>AdditionalMIPXScriptOptions&Operations
^Screen2Height 9	IExecuteTriggeredCapture:	^SingleStepExecution YES
^Screen3Height 9	{!}KEY 0x4000 F6	<SubMenu
!SetSplitScreen	{!}KEY 0x4000 F6	!ExecuteMIPXScriptFile.Name: scripts
<SubMenu	ICurrentImageBuffer 7	/checker.mpx
>VideoDigitize/Display	{!}KEY 0x4000 F6	>AdditionalMIPXScriptOptions&Operations
!CurrentImageBuffer 1	IExecuteTriggeredCapture:	^SingleStepExecution NO
{!}KEY 0x4000 F6	{!}KEY 0x4000 F6	<SubMenu
>SpecialOperations&Modes	ICurrentImageBuffer 8	!ExecuteMIPXScriptFile.Name: scripts
>TriggeredImageCapture	{!}KEY 0x4000 F6	/psp_avg.mpx
!ExecuteTriggeredCapture:	IExecuteTriggeredCapture:	<SubMenu
{!}KEY 0x4000 F6	{!}KEY 0x4000 F6	>ImageFileLoad/Save
{!}KEY 0x4000 F6	ICurrentImageBuffer 9	>FileLoad/Save.TIFFFormatw.AOI
!CurrentImageBuffer 2	{!}KEY 0x4000 F6	!SaveImageToFile.Name:
{!}KEY 0x4000 F6	IExecuteTriggeredCapture:	!SaveImageToFile.Name: images/image1.tif
!ExecuteTriggeredCapture:	{!}KEY 0x4000 F6	~ImageBufferSelected 1
{!}KEY 0x4000 F6	IExecuteTriggeredCapture:	!ImageAreaOfInterest:FullImage
{!}KEY 0x4000 F6	{!}KEY 0x4000 F6	<SubMenu
!CurrentImageBuffer 3	ICurrentImageBuffer 10	!ExecuteMIPXScriptFile.Name: scripts
{!}KEY 0x4000 F6	{!}KEY 0x4000 F6	/checker.mpx
!ExecuteTriggeredCapture:	IExecuteTriggeredCapture:	
{!}KEY 0x4000 F6	{!}KEY 0x4000 F6	
{!}KEY 0x4000 F6	ICurrentImageBuffer 11	
!CurrentImageBuffer 4	{!}KEY 0x4000 F6	
{!}KEY 0x4000 F6	IExecuteTriggeredCapture:	
!ExecuteTriggeredCapture:	{!}KEY 0x4000 F6	
{!}KEY 0x4000 F6	>MIPXScripts	
{!}KEY 0x4000 F6		
!CurrentImageBuffer 5		
{!}KEY 0x4000 F6		
!ExecuteTriggeredCapture:		
{!}KEY 0x4000 F6		
!CurrentImageBuffer		
{!}KEY 0x4000 F6		

PSP PIC.MPX CONT'D	<pre> CurrentImageBuffer 9 {!}KEY 0x4000 F6 !ExecuteTriggeredCapture: {!}KEY 0x4000 F6 {!}KEY 0x4000 F6 !CurrentImageBuffer 3 {!}KEY 0x4000 F6 !ExecuteTriggeredCapture: {!}KEY 0x4000 F6 {!}KEY 0x4000 F6 !CurrentImageBuffer 4 {!}KEY 0x4000 F6 {!}KEY 0x4000 F6 !ExecuteTriggeredCapture: {!}KEY 0x4000 F6 {!}KEY 0x4000 F6 !CurrentImageBuffer 5 {!}KEY 0x4000 F6 !ExecuteTriggeredCapture: {!}KEY 0x4000 F6 {!}KEY 0x4000 F6 !CurrentImageBuffer 6 {!}KEY 0x4000 F6 !ExecuteTriggeredCapture: {!}KEY 0x4000 F6 {!}KEY 0x4000 F6 !CurrentImageBuffer 7 {!}KEY 0x4000 F6 !ExecuteTriggeredCapture: {!}KEY 0x4000 F6 {!}KEY 0x4000 F6 !CurrentImageBuffer 8 {!}KEY 0x4000 F6 !ExecuteTriggeredCapture: {!}KEY 0x4000 F6 </pre>	<pre> >ImageFileLoad/Save >FileLoad/Save,TIFFFormatw.AOI !SaveImageOfFile.Name: !SaveImageOfFile.Name: images/image2.tif ~ImageBufferSelected 11 !ImageAreaofInterest:FullImage <QuitMenu <QuitMenu </pre>
	<pre> {!}KEY 0x4000 F6 !CurrentImageBuffer 10 {!}KEY 0x4000 F6 !ExecuteTriggeredCapture: {!}KEY 0x4000 F6 {!}KEY 0x4000 F6 !CurrentImageBuffer 11 {!}KEY 0x4000 F6 !ExecuteTriggeredCapture: {!}KEY 0x4000 F6 >MIPXScripts !ExecuteMIPXScriptFile.Name: /checker.mpx scripts </pre>	<pre> scripts </pre>
	<pre> !ExecuteMIPXScriptFile.Name: /checker.mpx scripts </pre>	<pre> scripts </pre>
	<pre> !ExecuteMIPXScriptFile.Name: /checker.mpx scripts </pre>	<pre> >AdditionalMIPXScriptOptions&Operations ^SingleStepExecution YES <QuitMenu </pre>
	<pre> !ExecuteMIPXScriptFile.Name: /checker.mpx scripts </pre>	<pre> >AdditionalMIPXScriptOptions&Operations ^SingleStepExecution NO <QuitMenu </pre>
	<pre> !ExecuteMIPXScriptFile.Name: /psp_avg.mpx scripts </pre>	<pre> scripts </pre>

CHECKER.MPX

```
<QuitMenu
  >VideoDigitize/Display
  !CurrentImageBuffer 1
  !CurrentImageBuffer 2
  !CurrentImageBuffer 3
  !CurrentImageBuffer 4
  !CurrentImageBuffer 5
  !CurrentImageBuffer 6
  !CurrentImageBuffer 7
  !CurrentImageBuffer 8
  !CurrentImageBuffer 9
  !CurrentImageBuffer 10
  !CurrentImageBuffer 11
  <QuitMenu
  >MPXScripts
```

PSP_AVG.MPX

```
<QuitMenu
  >VideoDigitize/Display
  !CurrentImageBuffer 1
  <QuitMenu
    >ImageProcessing
      >ImageSequenceOperations
        ~SequenceStartingBuffer 1
        ~SequenceEndingBuffer 11
        !AverageImageSequence
        !ImageAreaofInterest:FullImage
      <QuitMenu
        >MPXScripts
```

APPENDIX E.

DISK STRESS ANALYSIS AND ROTOR REDESIGN

The structural evaluation of the flat plate disk-rotor consisted of stress and modal analyses. The structural analysis determined the limiting rotational speed of the disk and verified characteristic modes of the disk would not be excited at the wheel speeds used in the experiment. The stress analysis was based on strain-displacement relationships for a uniform, thin rotating disk. Aerodynamic stresses and rotor-blade stresses were not incorporated in the computation. The modal analysis used finite-element methods in the structural analysis code MSC-NASTRAN. A summary of each analysis is provided. Due to the limiting speed of the current disk-rotor, the maximum tip Mach number attainable was 0.865. To obtain sonic tip conditions, a new disk-rotor design is required. A proposed design of this disk for use on the PSP test-rig apparatus is presented and summarized.

A. STRESS ANALYSIS

From the development of the strain-displacement relationships for a uniform, thin rotating disk with a central hole, the following relationships for radial and tangential stress was obtained (Baumeister, 1967):

$$\sigma_{\theta} = \frac{3+v}{4} \rho \omega^2 (R^2 + \frac{1-v}{3+v} r^2) \quad (E1)$$

$$\sigma_r = \frac{3+v}{8} \rho \omega^2 (R^2 - r^2) \quad (E2)$$

For type 6061-T6 aluminum plate (density = 0.1 lbs_m/in³, yield stress = 40,000 psi), the maximum wheel speed was limited by tangential stress at the inner hole location to 21,750 RPM. The tangential stress at the inner radius is plotted versus wheel speed in Figure E1 (top). Because blade and aerodynamic stresses were not computed, the operational limit was reduced to 20,000 RPM. Figure E2 (bottom) plots the radial and tangential stresses at the 20,000 RPM operational limit, as a function of the radial distance from the rim.

B. MODAL ANALYSIS

The modal analysis of the flat-plate disk-rotor was undertaken using MSC-NASTRAN for WINDOWS finite element methods. Plate elements were used in the formulation. The disk hub was constrained in the three translational directions and in the transverse and lateral rotational planes. Figure E2 depicts the NASTRAN mesh geometry and Table E1 lists the frequencies and the corresponding modes. The results show modes with complementary frequencies due to the symmetry of the model. The primary bending and flapping modes were shown to occur at low frequencies. A pitching mode, however, was found at 313 Hz and turbine operation in the vicinity of this frequency was monitored for excessive vibration. Figure E3 shows normalized deformation contours for the primary modes and exemplifies the solution symmetry in the second and third bending modes.

ω (Hz)	Natural Mode	ω (Hz)	Natural Mode	ω (Hz)	Natural Mode
17.850 17.972	1st Bending ¹	119.47	2nd Rotating	269.90 271.68	7th Bending
21.232	1st Flapping ²	128.15 129.70	Mixed mode ⁵ Bending / Flapping	302.97 303.99	5th Flapping
26.101 27.043	2nd Bending	147.90 147.91	5th Bending	312.24 313.15	1st Pitching ⁴
56.973	3rd Bending	161.94 167.84	3rd Flapping	330.60 340.01	Mixed mode Pitching / Bending
87.319	1st Rotating ³	205.10 207.31	6th Bending	341.93 342.79	Mixed mode Bending / Flapping
98.318 98.489	4th Bending	227.31 228.31	4th Flapping	343.39	
1Bending modes are asymmetric about the plane of rotation (XY plane). 2Flapping modes are symmetric about the plane of rotation (XY plane). 3Rotating mode is symmetric about the axis of rotation (Z axis). 4Pitching mode is translation in the plane of rotation (XY plane). 5Mixed modes have characteristics of more than one of the previously defined modes.					

Table E1. Disk-Rotor Modal Frequencies (Hz)

C. DISK-ROTOR REDESIGN

The design for a disk-rotor, capable of bearing the stress associated with sonic tip speeds, is based on constant stress distribution. The constant stress design requires varying the disk thickness, which subsequently will increase the difficulty in the disk manufacturing. Applying radial equilibrium and assuming constant stress, equation E3 is derived (Mattingly, 1987).

$$\frac{W_r}{W_R} = e^{\left(\frac{\rho(\omega R^2)}{2\sigma_y}(1 - (\frac{r}{R})^2)\right)} \quad (E3)$$

To obtain an estimate of disk thickness at the material yield and tensile stress limits, Figure E4 is plotted. The physical requirement for mounting the disk-rotor to the turbine is a flat interface, however, resulting in the estimated design geometry portrayed. In addition, imaging requirements at the disk rim necessitate a portion of the outer rim be flat. The design drawing is presented in Figure E5.

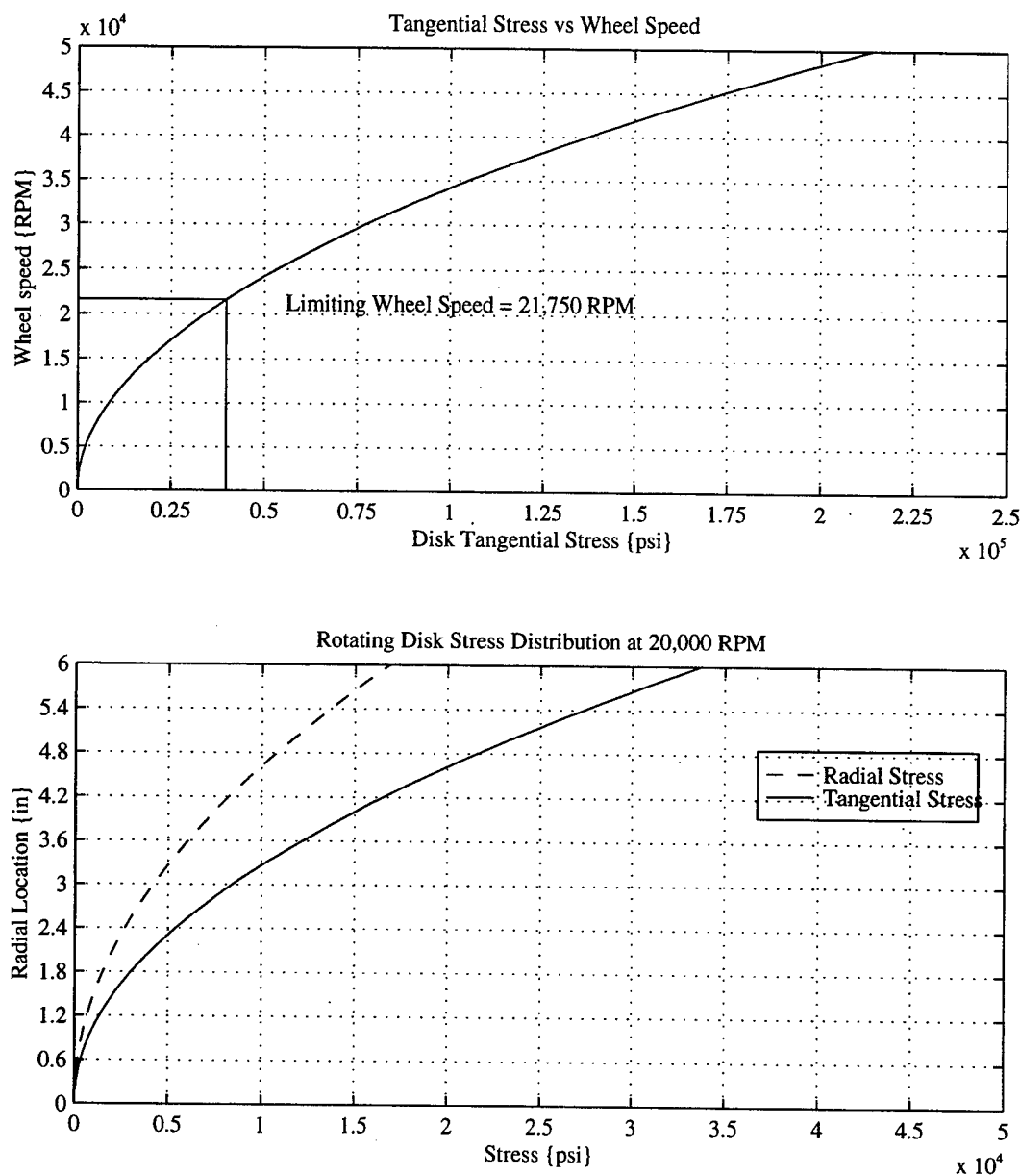
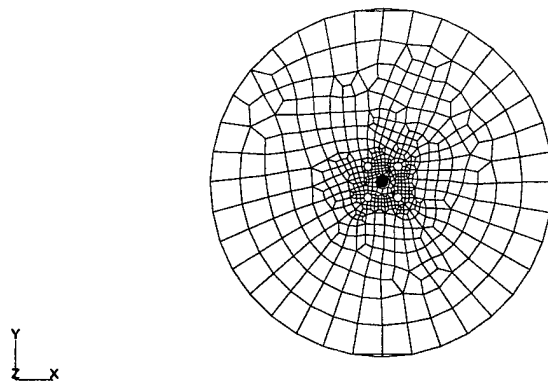


Figure E1. Disk-Rotor Stress Distributions

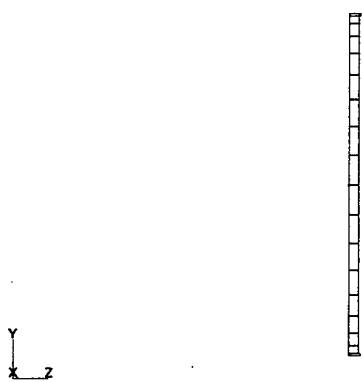
V: Disk Rotor ZX Front View

C: Constrained



V: Disk Rotor XY SideView

C: Constrained



V: Disk Rotor FE Geometry

C: Constrained

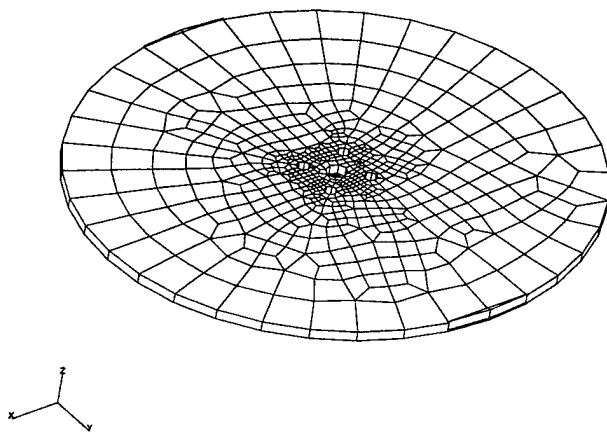


Figure E2. NASTRAN Disk-Rotor Finite Element Model

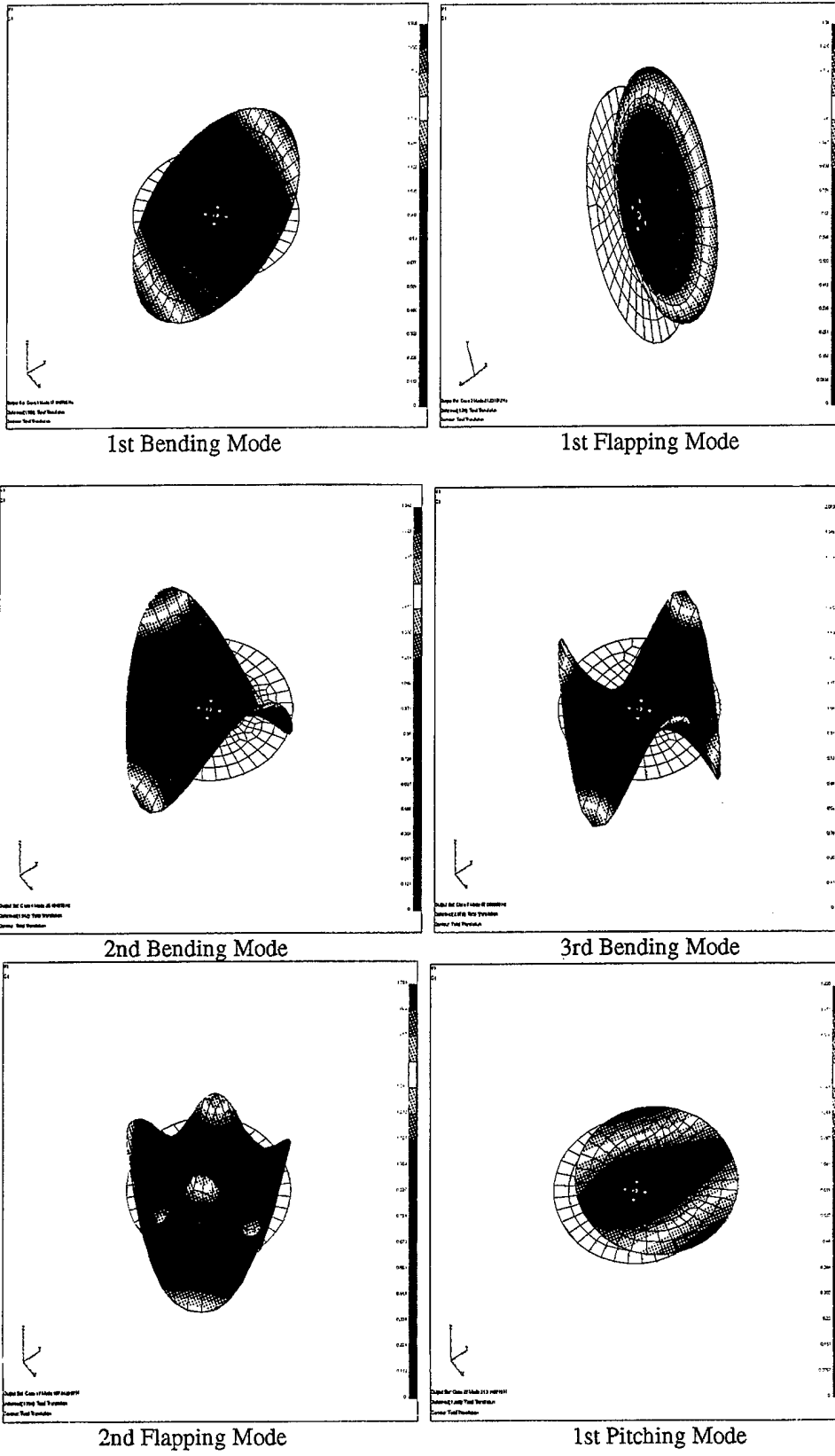


Figure E3. Disk-Rotor Modal Characteristics

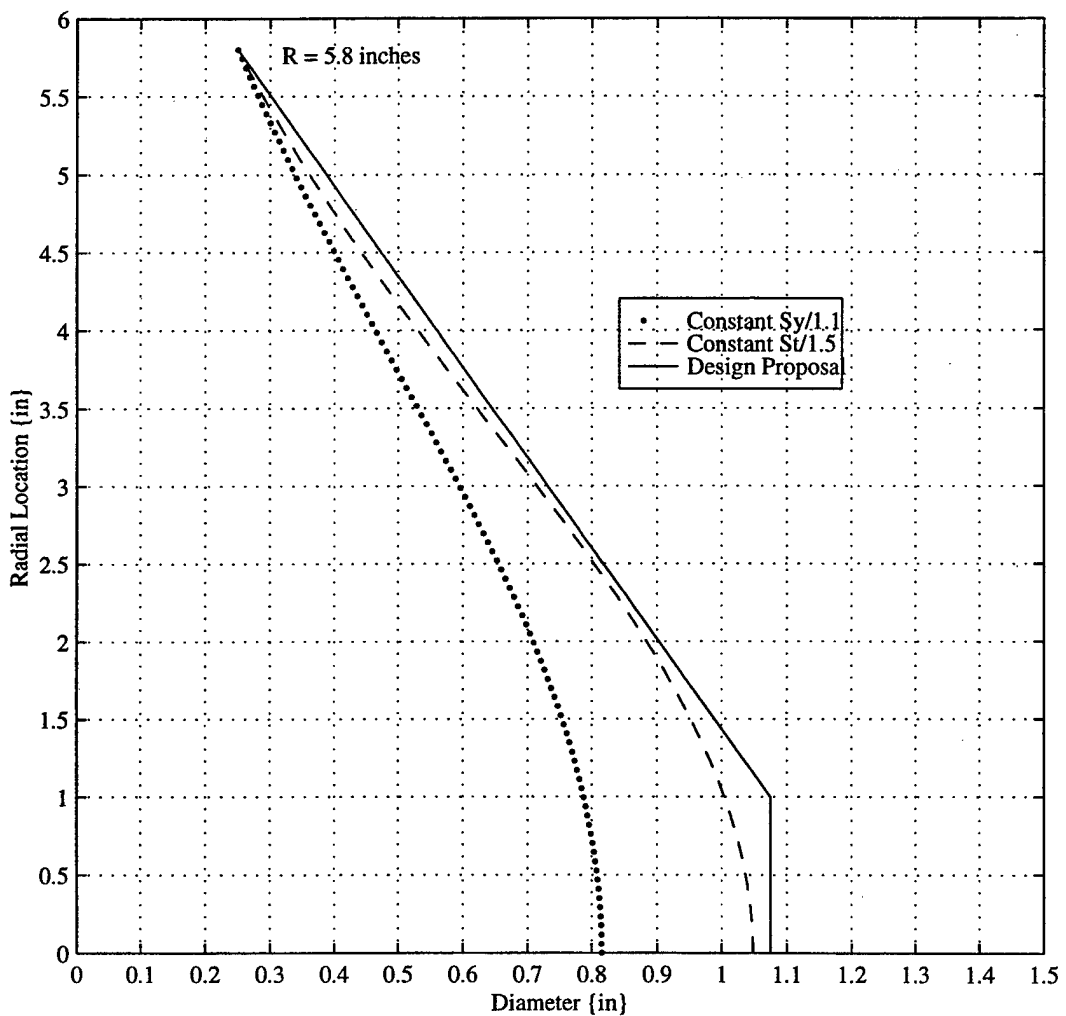


Figure E4. Constant Stress Disk-Rotor Thickness Distribution ($R = 5.8$ inches)

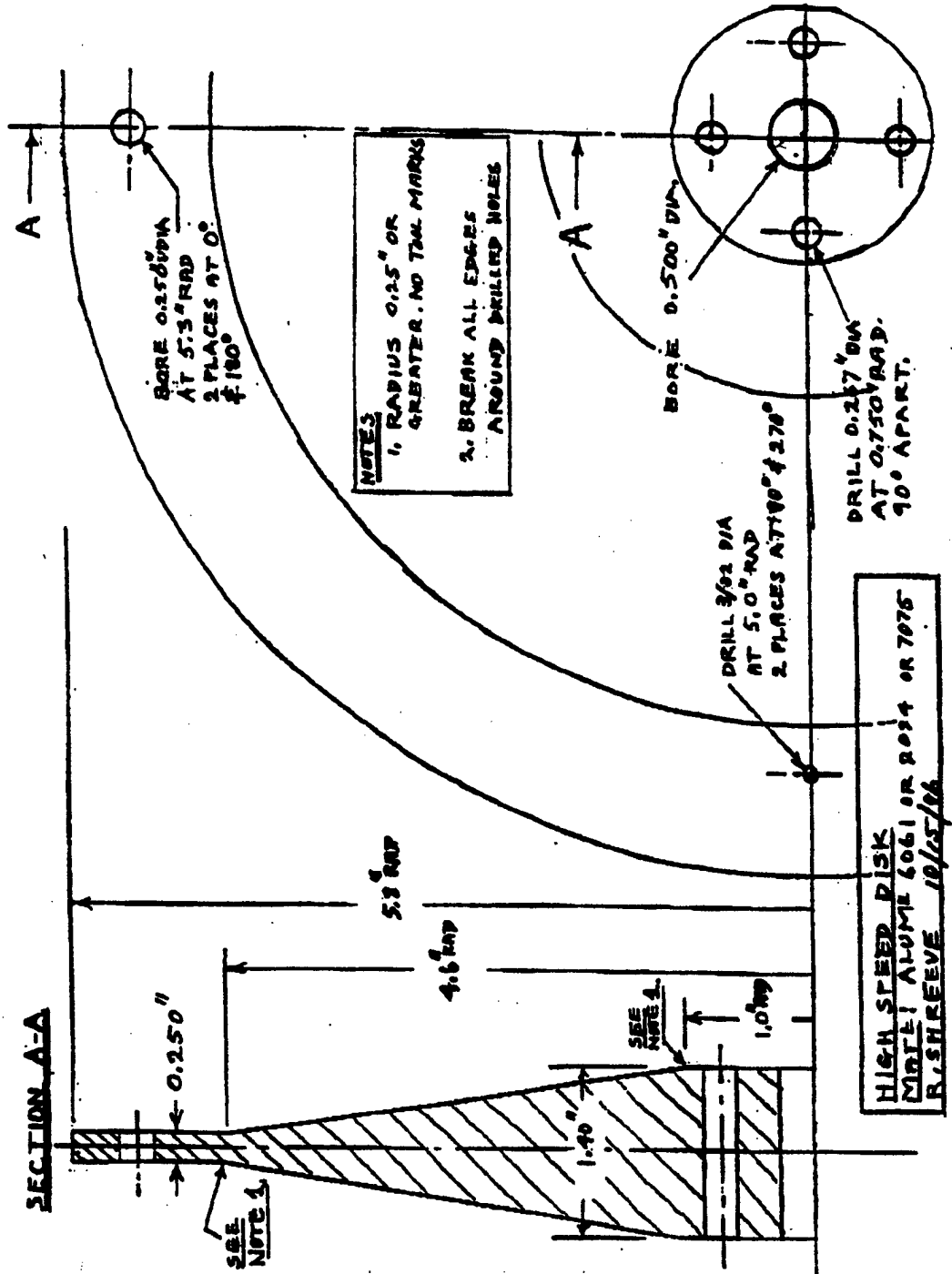


Figure E5. Disk-Rotor Redesign Drawing

LIST OF REFERENCES

Baumeister, Theodore (Ed.), *Standard Handbook for Mechanical Engineers, Seventh Edition*, McGraw-Hill, Inc., 1967, p. 5-73.

Buning, Pieter G., et al. "Overflow Users Manual; Version 1.6aw," NASA Ames Research Center, Moffett Field, CA, 12 July 1995.

Burns, Steven P. And Sullivan, John P., "The Use of Pressure Sensitive Paints on Rotating Machinery," International Congress on Instrumentation in Aerospace Simulation Facilities Paper, 1995.

Department of Electrical and Computer Engineering Printed Notes, "Electronic Circuits Laboratory Experiment, EC2220," Naval Postgraduate School, 1996.

EPIX Incorporated, "User's Manual, 4MEG Video Model 12, Revision 4.0 and 4.1," 1994.

EPIX Incorporated, "User's Manual, 4MIP - 4MIPTOOL Interactive Image Analysis Software, Version 2.8," 1993.

Hamilton Standard Technical Manual, "OverHaul Instructions, Turbine-Driven Fuel Pump; Model No. TPC-13, Assembly No. 705094 599151," 15 April 1968.

Hubner, J.P., Abbott, J. D., Carroll, B.F., "Pressure Measurements on Rotating Machinery Using Lifetime Imaging of Pressure Sensitive Paint," AIAA Paper No.96-2934, 32nd AIAA/ASME/SAE/ASEE Joint Propulsion Conference, Lake Buena Vista, FL July, 1996.

Kavandi, J.L., "Luminescence Imaging for Aerodynamic Pressure Measurements," Doctoral Thesis, Chemistry Department, University Of Washington, 1990.

Mattingly, J.D., Heiser, W.H., and Daley, D.H. *Aircraft Engine Design*, AIAA Education Series, 1987.

Oriel Corporation, "Instruction Manual, Lamp Controller, Model 6405," 1992.

Reid, William D., "Transonic Axial Compressor Design Case Study and Preparations for Testing," M.S. Thesis, Naval Postgraduate School, September, 1995.

Roberts, D. Allan, "Radiometry/Photometry Terms," *The Photonics Design and Applications Handbook*, 1993, pp. H68-H71.

Sanger, N.L., "Design of a Low Aspect Transonic Compressor Stage Using CFD Techniques," *ASME Journal of Turbomachinery*, Volume 118, July 1996. pp. 479-91.

Schlichting, H., *Boundary Layer Theory*, McGraw-Hill, 1960.

Seivwright, Douglas L., "Application of Pressure-Sensitive Paint in Shock Boundary Layer Interaction Experiments," M.S. Thesis, Naval Postgraduate School, March, 1996.

Torrington Company, "Torrington Company Service Catalog. , Form Number 100-889-50M First Edition, Second Printing", p E62.

Sony Corporation, "Sony Trinitron Color Video Monitor PVN-1954Q Operating Instructions," 1993.

UDT Sensors Inc., "Optoelectronic Components Catalog," 1996.

Varner, Donald R., *Pressure Sensitive Paint Measurement on a Rotor*, M.S. Thesis, Naval Postgraduate School, March, 1995.

Xybion Electronic Systems, "Electronically Gated Intensified CCD Video Camera, Model ISG-350," May, 1992.

Xybion Electronic Systems, "Video Camera Control Unit User's Manual, Model CCU-01," September, 1990.

INITIAL DISTRIBUTION LIST

1.	Defense Technical Information Center	2
	8725 John J. Kingman Rd., STE 0944	
	Ft. Belvoir, VA 22060-6218	
2.	Dudley Knox Library	2
	Naval Postgraduate School	
	411 Dyer Rd.	
	Monterey, CA 93943-5101	
3.	Department of Aeronautics and Astronautics	
	Naval Postgraduate School	
	699 Dyer Road -- Room 137	
	Monterey, CA 93943-5106	
	ATTN: Chairman, Code AA	1
	Professor R.P. Shreeve, Code AA/SF	5
	Assoc. Professor G.V. Hobson, Code AA/HG	1
	Curricular Officer, Code 31	1
4.	Naval Air Warfare Center - Aircraft Division	
	Propulsion and Power Engineering	
	22195 Elmer RD, Unit 4	
	Patuxent River, MD 20670-1534	
	ATTN: J. Zidzik, Code 4.4.7.1, BLDG 106	1
	S. McAdams, Code 4.4.7.1, BLDG 106	1
	C. Gorton, Code 4.4T, BLDG 106.....	1
5.	U.S. Air Force, WL/POTX	
	BLDG 18	
	1950 Fifth ST.	
	Wright Patterson AFB, OH 45433-7281	
	ATTN: Dr. Doug Rabe	1
6.	LT Donald R. Varner, USN.....	1
	US Naval Academy	
	Department of Aeronautics and Astronautics	
	Annapolis, MD 21412	
7.	CAPT Joseph F. Quinn Jr., USNR(R)	1
	66 Pine Tree Circle	
	North Kingstown, RI 02852	
8.	LT Kevin J. Quinn, USN	2
	2335 Brian's Way	
	Lusby, MD 20657	